Search for medium effects with jet-like hadron correlations at ALICE at the LHC

Patrick Aaron Scott

Thesis submitted for the degree of

Doctor of Philosophy

Nuclear Physics Group,
School of Physics and Astronomy,
University of Birmingham.

September 2013

CERN-THESIS-2013-206
//2013

ABSTRACT

We present an analysis of the properties of jets in proton–proton and lead–lead collisions at the ALICE experiment at the CERN Large Hadron Collider, using the technique of two-particle angular correlations. The data sample comprises proton collisions at energies of $\sqrt{s} = 7$ TeV and $\sqrt{s} = 2.76$ TeV, and lead collisions at a nucleon–nucleon collision energy of $\sqrt{s_{\mathrm{NN}}} = 2.76$ TeV, from data taking periods in 2010 and 2011.

The jet width and transverse momentum imbalance, quantified by the jet fragmentation transverse momentum j_{T} and the net partonic transverse momentum k_{T} respectively, were studied in minimum bias proton collisions. The width was found to be independent of hadron transverse momentum, with a value of $\sqrt{\langle j_{\mathrm{T}}^2 \rangle} \approx 0.8$ GeV. This is higher than measurements from earlier experiments at lower beam energies, consistent with theoretical expectations. $\sqrt{\langle k_{\mathrm{T}}^2 \rangle}$ was found to increase with collision energy and also with the transverse momentum of the hadrons in the jet.

The dependence of jet yield on the produced multiplicity was studied in proton and ion collisions, with the multiplicity providing an estimator for the ion collision centrality. The ratio of awayside to nearside yield was studied, with a view to identifying suppression of jet momentum through interaction with a deconfined quark-gluon plasma. This suppression was identified in lead collisions as expected from previous results, but no suppression was observed in high multiplicity proton collisions.

The jet width and transverse momentum imbalance were also studied as a function of multiplicity, with the width quantified by j_{T} and the imbalance quantified by the correlation function awayside peak width. In proton collisions, the jet width was measured to be $\sqrt{\langle j_{\mathrm{T}}^2 \rangle} \approx 0.8$ GeV independently of multiplicity; this was consistent

with the measurements in minimum bias collisions. No firm evidence of medium effects was observed in measurements of the awayside peak width in proton or lead collisions, but the jet width was observed to decrease in lead collisions of increasing centrality. This was interpreted as a suppression of the high momentum hadrons in the jets.

DECLARATION OF AUTHOR'S CONTRIBUTION

It is the nature of research that no work is performed in isolation, and this work would not have been possible were it not for the efforts of many others. In particular, I could never have performed my analysis without the combined work of the many people involved with every stage of the design, construction and operation of the LHC and the ALICE experiment. Nevertheless, with that caveat the work presented in this document is entirely my own and unless otherwise indicated, all figures and results were produced by myself.

The bulk of my analysis work consisted of developing a framework for the construction of two-particle azimuthal correlation functions, which built upon official ALICE analysis code, and for the extraction of relevant quantities from these correlation functions. This is described in chapter 4, with the results in chapters 5, 6 and 7.

To extract the RMS net partonic transverse momentum $\sqrt{\langle k_{\mathrm{T}}^2 \rangle}$ from the measured quantities, a Monte-Carlo model was developed. This is described in detail in appendix B. A Monte-Carlo model was also developed to determine the relationship between collision centrality and particle multiplicity in lead–lead collisions. This model is described in appendix C.

In addition to my own work, I shared in the responsibilities of the operation of the Central Trigger Processor (CTP) through undertaking shifts in the control room whilst based at CERN, and also through acting as an on-call expert.

ACKNOWLEDGEMENTS

Over the past four years I have drawn help from many people, both in and out of work. Here I would like to show my appreciation; if I have omitted anyone who deserves to be mentioned then it is only through my own forgetfulness.

Firstly I would like to thank my supervisors, Roman Lietava and Peter Jones. Without their patient help and expert guidance I would doubtless not have come close to completing the work presented here. I am also indebted to the rest of the staff in the Birmingham ALICE group: David Evans, Orlando Villalobos-Baillie, Lee Barnby, Cristina Lazzeroni, Anton Jusko, Marian Krivda, Gron Jones and Frank Votruba. Special mention must go to David for his tireless support of the group (and for all of the cigars and wine), and to Anton for tolerating my many phone calls in the small hours of the morning as I frantically tried to fix trigger emergencies.

I have enjoyed sharing offices in Birmingham and at CERN with the other students of the Birmingham ALICE group, in particular Arvinder Palaha and Plamen Petrov whose help and advice I found invaluable. I would also like to thank the other students of the group: Zoe Matthews, Ravjeet Kour, Sparsh Navin, Luke Hanratty, Graham Lee and Didier Alexandre.

At CERN I benefited greatly from collaboration with Filip Krizek, Jan Rak and Sami Räsänen, who shared with me their knowledge of correlation analysis and Monte-Carlo modelling. I was also aided by Misha Ryskin and Valery Khoze, whose expertise enhanced the theoretical interpretation of my results.

Outside of work, I cannot neglect to thank my friends at CERN, too numerous to name, for all of the late nights, long days, ski trips, journeys across Europe and general shenanigans that made my eighteen month stay in Geneva so fantastic. I have also greatly enjoyed my time in the particle physics group and, more broadly, in

the School of Physics and Astronomy, and this is due in no small part to my friends in Birmingham. Special mention is due to Rory Smith (who always maintained that the pickle was implied), Tom McLaughlan and the denizens of West 316 (whose office tennis court and other inventions provided a welcome distraction), Sarah Baker (for giving me somewhere to live when I needed it), Pete Rothery, Brigid Jones, Jim Smyth and everyone else. I'll miss you guys.

I would like to thank Paul Newman and Peter Watkins for giving me the chance to join the particle physics research group, and the Science and Technology Facilities Council for funding my PhD.

I would like to express my gratitude to my family, especially my parents Adam and Hetty, for all of their help over the years, providing me with constant moral (and occasional financial) support.

Finally I would like to thank Amy, for always being there.

So that no more with bitter sweat
I need to talk of what I don't know yet,
So that I may perceive whatever holds
The world together in its inmost folds.

Goethe - *Faust*

Three quarks for Muster Mark!

J. Joyce - *Finnegans Wake*

CONTENTS

LIST OF FIGURES

LIST OF TABLES

CHAPTER 1

INTRODUCTION

The present understanding of interactions in nature includes four fundamental forces: gravity, electromagnetism and the strong and weak nuclear interactions. Gravity will be omitted from this discussion as it is significantly weaker than the other three, and its theoretical description proceeds along very different lines (although the possible unification of gravity with the other forces is an open question in physics). The other three interactions are described by the exchange of virtual bosons: photons in the case of electromagnetism, $W^{\pm}$ and Z^0 bosons for the weak interaction, and gluons for the strong interaction.

The quantum field theory of electromagnetism (quantum electrodynamics) and the unified electroweak theory describe electromagnetic and weak interactions to great precision, indeed quantum electrodynamics has been described as the "jewel of physics" for the extreme accuracy of its predictions [1]. This is partly because the small coupling constant means that not many terms in a perturbative expansion

are needed to provide a good degree of accuracy, and partly because the existence of elementary charged and electroweakly interacting free particles (leptons) allows precise experimental investigation. A classic example of this would be the precise measurement of many electroweak variables at the Large Electron–Positron Collider (LEP) [2]. Neither of these are the case for the strong interaction as, due to the running of the strong coupling, perturbative expansions are not possible except for interactions with a large transferred momentum, and also the property of confinement means that fundamental strongly interacting particles do not exist freely in nature but exist instead in bound states.

1.1 Quantum chromodynamics

The strong interaction is the strongest of the four fundamental interactions and is responsible for binding nucleons (protons and neutrons) together into atomic nuclei. However, nucleons are not fundamental particles but are believed to be composed of quarks, and it is also the strong interaction which binds these constituents together to form the nucleons. Indeed, the constituent particles are exposed to the "full" strong interaction, while the binding of atomic nuclei is due only to the residual strong force between the nucleons.

The current accepted theoretical description of the strong interaction is the theory of quantum chromodynamics (QCD). While similar to quantum electrodynamics (QED) and electroweak theory in that it describes elemental particles carrying a charge (the so-called colour charge in the case of QCD) interacting via the exchange of virtual bosons, it has many important differences. Particularly important is that the exchange bosons, gluons, carry colour charge [2]. This means that gluons can self-interact, which fundamentally affects the properties of the interaction.

1.1.1 The quark–parton model

The theory of the strong interaction has its roots in the parton and quark models of the 1960s. The parton model originated as particle accelerators began to be sufficiently energetic for deep inelastic electron–proton scattering to probe the internal structure of nucleons [3]. It was subsequently shown by Bjorken that the observed cross sections could be explained as evidence that nucleons were not elementary but were in fact comprised of point-like "partons" [4].

At around the same time, the quark model was proposed independently by Gell-Mann and Zweig [5, 6]. This was motivated by the large number of observed hadronic (divided into bosonic mesons and fermionic baryons) states that had been discovered over the preceding decade, which were considered to be too numerous to all be fundamental.

The quark model explained these states as composite particles comprised of fractionally charged, spin-$\frac{1}{2}$ "quarks", along with their corresponding antiquarks; mesons were described as quark–antiquark ($q\bar{q}$) pairs, baryons as three quarks (qqq) and antibaryons as three antiquarks ($\bar{q}\bar{q}\bar{q}$). Three "flavours" of quarks were needed to account for the observed combinations of charge, isospin (originally introduced in response to the symmetries between the proton and neutron, and later generalised to other hadrons) and strangeness (invoked to account for the long decay time of the kaon relative to its mass); these were named the up (u), down (d) and strange (s) quarks. The prediction and subsequent discovery of the Ω^- baryon, consisting of three strange quarks, was strong evidence for the validity of the quark model [7]. It was later discovered that in addition to the u, d and s quarks, there existed charm (c), bottom (b) and top (t) quarks, with masses too high to be produced at 1960s experiments. The quarks and their quantum numbers are summarised in table 1.1.

A problem for the quark model was the need to explain the discovery of the Δ^{++} baryon, which according to the model comprised three u quarks with parallel spins

Table 1.1: Quark flavours and their quantum numbers [8].

Flavour	Charge	Other
u	$+^2/_3$	Isospin $= +^1/_2$
d	$-^1/_3$	Isospin $= -^1/_2$
s	$-^1/_3$	Strangeness $= -1$
c	$+^2/_3$	Charm $= +1$
b	$-^1/_3$	Bottom $= -1$
t	$+^2/_3$	Top $= +1$

and should thus have violated the Pauli exclusion principle. This problem was averted with the introduction of an additional quantum number, which was not observed in hadrons and thus must sum to zero for physical states. This quantum number, with the symmetry described by the SU(3) group, was termed colour, with each quark having a colour of "red", "green" or "blue" and likewise with "anti-colours" for the antiquarks. Physical hadron states are SU(3) singlets (colourless), either by having equal numbers of all three colours of quark (for example a baryon must have a red, a green and a blue quark), or by having each colour sum to zero (for example a meson could have red–antired, green–antigreen or blue–antiblue quarks).

The quark and parton models were realised to be describing the same objects, and together form the quark–parton model. Later deep inelastic electron–nucleon scattering experiments determined that hadrons can in fact contain large numbers of quarks, gluons and antiquarks. However, the quark–parton model of flavour remains valid with the observation that the net quark content of a given hadron obeys a sum rule. A proton, for example, is in the quark model composed of (uud). Following the sum rules, for a proton $\Sigma(u) - \Sigma(\bar{u}) = 2$, $\Sigma(d) - \Sigma(\bar{d}) = 1$, and for all other quark flavours $\Sigma(q) - \Sigma(\bar{q}) = 0$. These net quarks are termed valence quarks, and the rest sea quarks. In QCD, the quarks are viewed as elementary fields, with hadrons existing as bound states of these.

1.1.2 Confinement

Experimental investigation of the strong interaction is complicated by the fact that elementary strongly interacting particles do not exist freely in nature but are bound inside hadrons, a property known as confinement. As such, it is impossible to observe an isolated scattering of coloured particles in the same way as, for example, electron scattering provides a clean way to study the electroweak interaction. A description of a widely studied QCD process that could be observed at a collider experiment (hadronic jet production as a consequence of hard parton scattering) can be found in section 2.1.

In QCD, the strong interaction is described in terms of the exchange of massless bosons known as gluons. As stated in the introduction to this section, in contrast to the uncharged photons in QED, gluons carry colour charge. This has consequences when two quarks are pulled apart, and leads to the phenomenon of confinement.

To visualise this process it is instructive to consider the QCD colour field lines as a function of separation, as shown in figure 1.1. At very short distances of much less than the typical hadron size of 1 fm, the QCD potential behaves analogously to the QED potential, with an r^{-1} dependence (figure 1.1a). At longer distances, approaching the hadron size, the gluon self-interaction pulls the gluons exchanged between the quarks into a "flux tube" as shown in figure 1.1b. Here the field energy per unit length is approximately constant, analogously to a stretched spring. Taking into account both of these components, the strong potential V_{S} has the form

$$V_{\mathrm{S}} = -\frac{4}{3}\frac{\alpha_{\mathrm{S}}}{r} + kr \tag{1.1}$$

where α_{S} is the strong coupling, k is the tension of the flux tube and r is the separation of the quarks.

At even larger separations of greater than 1 fm, it becomes more energetically

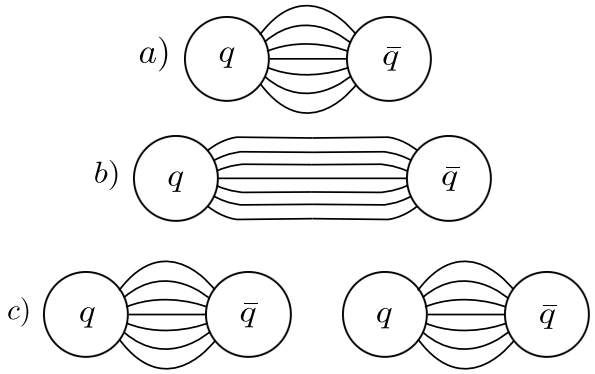

Figure 1.1: The confinement of quarks visualised in terms of the QCD field lines.
a) The colour field at very short range behaves much like the QED field.
b) At longer range, the characteristic "flux tube" behaviour.
c) At even longer range, it becomes more energetically favourable for a new $q\bar{q}$ pair to be produced.

favourable for a new $q\bar{q}$ pair to be produced from the field energy and the flux tube "breaks", leading to two separate hadrons, which are individually confined.

Despite this picture of confinement, to date there has been no analytic proof that QCD should be confining. However, due to the lack of any observation of bound coloured states, it is generally accepted.

As well as defining hadron size to around 1 fm, the majority of hadron mass also arises from confinement: nucleons have mass of the order of 1 GeV, while the bare quark mass is expected to be of the order of 1 MeV (although there is no way to directly measure this at present).

1.1.3 Asymptotic freedom

The strong coupling α_S, used to define the strength of the strong interaction, is not in fact constant but varies with separation r. Due to the Heisenberg uncertainty principle, this is equivalent to a dependence on transferred four-momentum q. This arises due to quantum vacuum fluctuations and related effects occur in both QED and QCD.

In QED, virtual electron–positron pairs can appear from the vacuum and act as dipoles, being polarised by the presence of a real charge (such as a real electron). These act to shield the field of the real charge which results in its measured charge increasing asymptotically with the momentum of a probe, or equivalently with decreasing separation. The electron charge is typically taken as its value measured at infinity, with the QED coupling α "running", that is to say increasing with decreasing separation (or alternatively with increasing q).

A similar effect is present for QCD with virtual $q\bar{q}$ pairs shielding a bare colour charge but, due to the gluon self-interaction, gluon loops arise as well as $q\bar{q}$ loops. This leads to the net gluon contribution being in fact an anti-shielding which dominates over the $q\bar{q}$ shielding, with the net effect being that α_{S} decreases with smaller separation (or equivalently, α_{S} decreases with increasing q).

As the coupling increases with separation, it cannot be scaled with respect to the coupling at infinity, as is done with QED, but must instead be defined relative to the coupling at a reference scale μ. From quantum field theory, this leads to the expression for $\alpha_{\mathrm{S}}(Q^2)$, where $Q^2 = -q^2$:

$$\alpha_{\mathrm{S}}(Q^2) = \frac{\alpha_{\mathrm{S}}(\mu^2)}{1 + \beta_0 \alpha_{\mathrm{S}}(\mu^2) \ln\left(\frac{Q^2}{\mu^2}\right)} \tag{1.2}$$

where $\beta_0 = \frac{1}{12\pi}(2n_{\mathrm{q}} - 11n_{\mathrm{c}})$, $n_{\mathrm{q,c}}$ being the number of quark and colour degrees of freedom. For QCD, with six quark flavours and three colours, $\beta_0 = -\frac{7}{4\pi}$. This is usually expressed in terms of the QCD scale constant $\Lambda^2_{\mathrm{QCD}} = \mu^2 \exp\left[-1/\beta_0 \alpha_{\mathrm{S}}(\mu^2)\right]$ which can be thought of as the scale at which the coupling becomes large. Defining also the positive quantity $b = -\beta_0$, equation 1.2 simplifies to [9]

$$\alpha_{\mathrm{S}}(Q^2) = \frac{1}{b \ln(Q^2/\Lambda^2_{\mathrm{QCD}})}. \tag{1.3}$$

From this equation the running of α_{S} is apparent. For $Q^2 \gg \Lambda_{\mathrm{QCD}}$, corresponding

to small separation, $\alpha_S \ll 1$ and thus the interaction can be treated perturbatively, much as in QED. This is the basis for perturbative QCD (pQCD), which has had much success in calculating, for example, cross sections for various hard (high Q^2) QCD processes [9]. However, at low Q^2 of the order of Λ^2_{QCD} and lower, α_S becomes large and a perturbative expansion is impossible. Instead, non-perturbative techniques must be used, such as lattice QCD; this approach formulates QCD on a discrete spacetime lattice of finite size, with quarks defined on the sites and gluons on the links [10]. Monte-Carlo techniques can then be applied to solve such a system numerically.

Measurements of α_S at a range of Q^2 values are shown in figure 1.2 and from these it has been determined that $\Lambda_{QCD} \sim 0.2$ GeV, which is equivalent to a distance of roughly 1 fm. This is what constrains hadron size to this scale.

If one takes the running of α_S to its logical conclusion, it becomes apparent that at asymptotically large Q^2, $\alpha_S(Q^2) \to 0$; hence the partons behave as if free, as first predicted by Gross, Wilczek and Politzer [11, 12]. This phenomenon is known as asymptotic freedom.

1.2 Quark–gluon plasma

The phenomenon of asymptotic freedom, as described in section 1.1.3, applies to partons at close separation within a hadron. However, it also leads to the conclusion that at extremely high energy density, bulk hadronic matter would become deconfined with partons able to propagate freely through the medium. In such a system of independent partons, hadrons would cease to exist [13]. This state of matter is commonly referred to as quark–gluon plasma (QGP), and according to big bang cosmology the universe was likely in such a state before $t \sim 10$ µs [14].

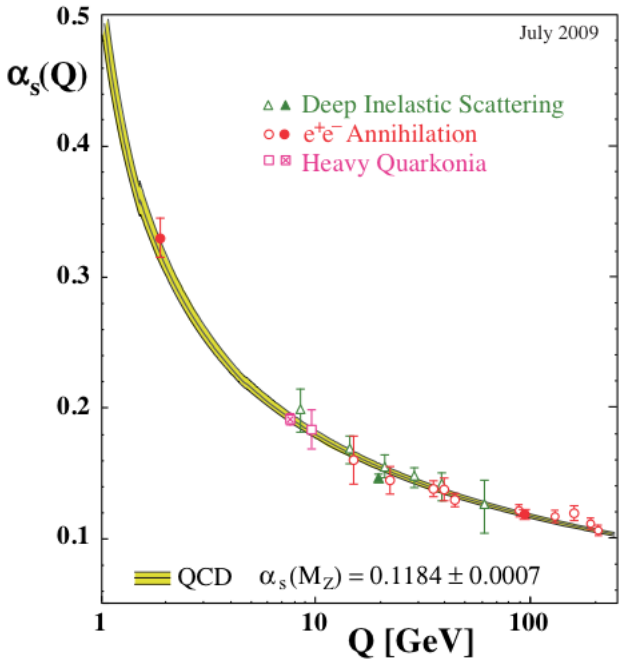

Figure 1.2: Dependence of the strong coupling α_S on transferred momentum Q, from PDG 2010 summary of world data [8].

1.2.1 Debye screening

Deconfinement can occur in a dense medium, at lower energy densities than would be required to reach the asymptotic limit, by a screening process analogous to the Debye screening of electric charges in an electromagnetic plasma. Much as the presence of mobile electric charges screens the field of a point charge in an electromagnetic plasma, mobile colour charges cause screening in a nuclear medium heated or compressed to sufficient density that the nucleon boundaries begin to overlap. Due to this colour charge screening, individual partons interact only with other partons within the screening length, which is inversely proportional to the cube root of the energy density. As this length becomes comparable to the mean separation, the partons behave as if free.

Taking only the Coulomb-like (short range) part of equation 1.1 and including Debye

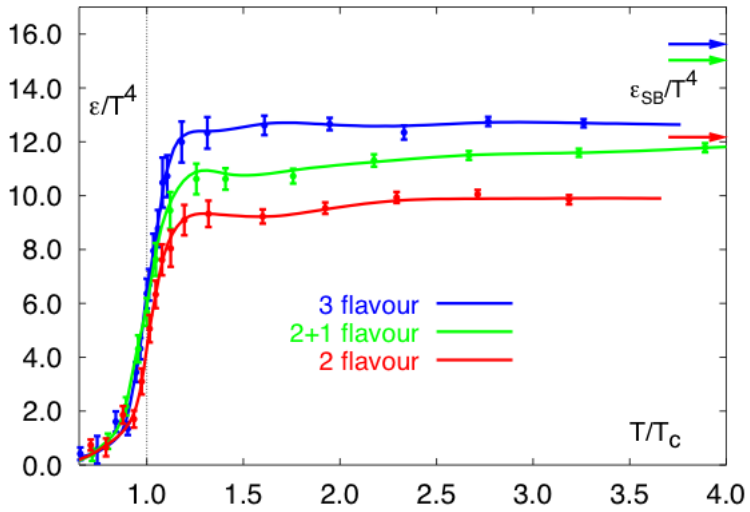

Figure 1.3: Ratio of energy density to T^4 in strongly interacting matter as predicted by lattice QCD, where T is temperature. 2 and 3 flavour calculations include two and three light quarks, respectively, and 2+1 flavour calculations include two light quarks and a heavy strange quark [16].

screening gives

$$V_{\mathrm{S}} \sim -\frac{\alpha_{\mathrm{S}}}{r} \cdot \exp\left(-\frac{r}{r_{\mathrm{D}}(T)}\right) \tag{1.4}$$

where $r_{\mathrm{D}}(T)$ is the Debye screening radius, which characterises the separation within which colour charges interact with each other [15]. It is dependent on the temperature of the system, being infinite at low temperature (implying no screening) and becoming shorter with increasing temperature over a critical temperature T_{C}. When $r_{\mathrm{D}}(T)$ becomes smaller than the hadronic radius, bound hadrons cease to exist. Due to this screening effect, nuclear matter can undergo a transition to a deconfined QGP state at a lower energy density than would be required for an asymptotically free QGP.

As α_{S} can still not be assumed to be small in this case, perturbative calculations cannot be used. Instead, non-perturbative methods must be applied to model the properties of a non-asymptotically-free QGP. Particularly useful is lattice QCD, which has been used extensively to calculate thermodynamic properties of the QGP such as the critical temperature of the phase transition.

Lattice QCD calculations of the critical temperature T_{C} depend on the number of quark flavours considered, among other parameters, but generally yield conclusions that $T_{\mathrm{C}} \approx 170\,\mathrm{MeV}$ with a corresponding critical energy density $\epsilon_{\mathrm{C}} \approx 1\,\mathrm{GeV/fm^{-3}}$ [16]. QGP energy densities from such calculations, for various numbers of quark flavours, are shown in figure 1.3. The phase transition to a QGP state is clearly visible at $T = T_{\mathrm{C}}$.

Typically, the produced energy density is quantified by the Bjorken energy density

$$\epsilon_{\mathrm{Bj}} = \frac{dE_{\mathrm{T}}}{dy}\frac{1}{S_{\mathrm{T}}\tau} \tag{1.5}$$

where dE_{T}/dy is the transverse energy per unit rapidity (which can be related to the produced multiplicity of charged particles), S_{T} is the transverse overlap area of the colliding nuclei and τ is the plasma formation time [17]. Rapidity is defined in appendix A. In $\sqrt{s_{\mathrm{NN}}} = 0.2\,\mathrm{TeV}$ gold–gold collisions at the Relativistic Heavy Ion Collider (RHIC), a measurement was made of $\tau\epsilon_{\mathrm{Bj}} = 5.2 \pm 0.4\,\mathrm{GeV/fm^2}$ which, assuming a formation time $\tau < 1\,\mathrm{fm}/c$, gives an energy density of at least several $\mathrm{GeV/fm^3}$, well in excess of the critical energy density as predicted by lattice QCD [18].

Increased beam energy leads to a higher energy density and indeed measurements at the ALICE experiment at the LHC indicate values of $\tau\epsilon_{\mathrm{Bj}} \approx 15\,\mathrm{GeV}$ in central lead–lead collisions [19]. As such, QGP is believed to be accessible to modern collider experiments.

1.2.2 The phase diagram of quantum chromodynamics

A schematic representation of the QCD phase diagram, as a plot of temperature T against baryon chemical potential μ_{B} is shown in figure 1.4. μ_{B} is a representation of the net baryon density, and characterises the imbalance between quarks

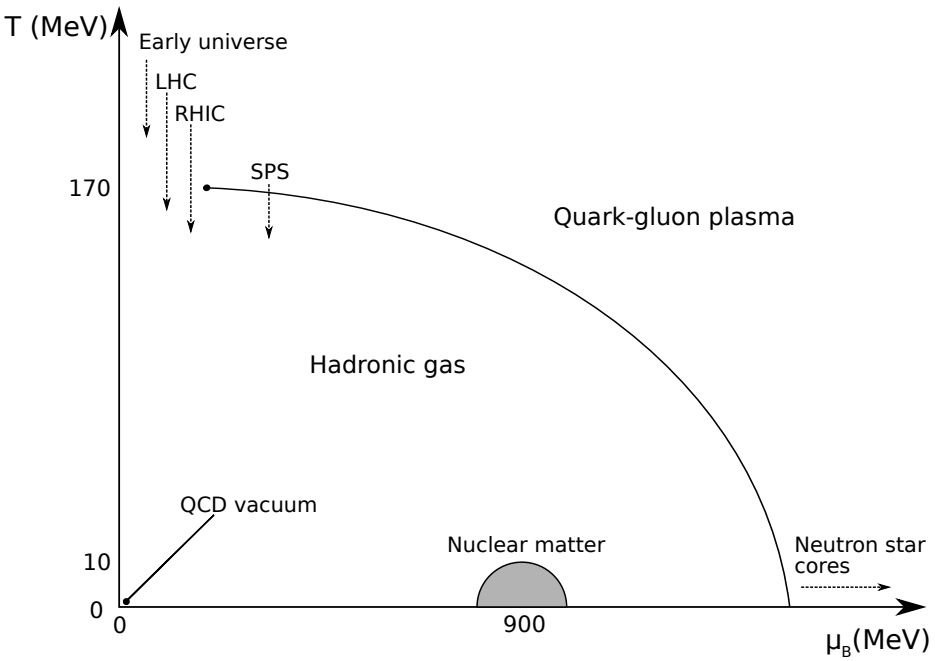

Figure 1.4: Schematic representation of QCD phase diagram in temperature and baryon chemical potential plane.

and antiquarks (although it does not give an absolute measurement of density). For $\mu_{\mathrm{B}} \approx 0$ lattice QCD can be used, and the rest of the diagram is deduced from QCD phenomenology and equilibrium thermodynamics. The diagram shows the distinction between confined hadronic matter and deconfined QGP, and it is expected that the phase transition between these states is a crossover type at low μ_{B} and first order at higher μ_{B}, with a critical point existing. However, this is not yet fully established [20].

Cold nuclear matter is shown at low-T, $\mu_{\mathrm{B}} \approx 900$ MeV, and QCD vacuum exists in the limit of $T, \mu_{\mathrm{B}} \to 0$. Conditions expected at various past and present heavy ion collider experiments are marked, which tend to increased T and lower μ_{B} with increasing energy. The early universe is presumed to have existed in the extreme high T, low μ_{B} position on the diagram with enormous temperature and approximately equal quark and antiquark densities.

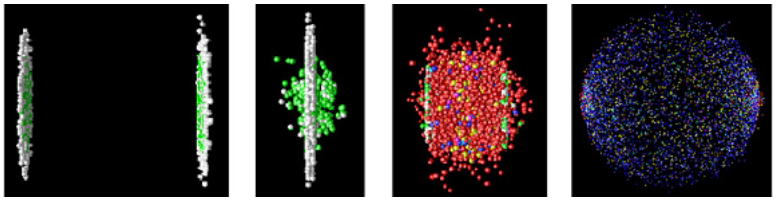

Figure 1.5: Simulation of a heavy ion collision [21].

There also exists a phase transition to deconfined matter at low T and high μ_{B}, which could occur in matter of very high pressure. This high pressure, (relatively) low temperature matter is theorised to possibly exist in the core of compact stellar objects such as neutron stars and hypothetical quark stars. However, such a system is inaccessible to current experiments.

1.3 Experimental production of QGP

1.3.1 Relativistic heavy ion collisions

As stated in section 1.2.2, ultrarelativistic heavy ion collisions can be used to produce a high temperature, low baryon chemical potential QGP, similar to (but less extremely so than) that of the early universe. At these experiments, the nuclei of heavy elements are accelerated to high energy and collided inside detectors to record the produced particles.

Figure 1.5 shows a simulation of a heavy ion collision. The nuclei impact each other as Lorentz contracted "pancakes" which experience nucleon–nucleon collisions but do not stop in the centre of mass frame. As they pass through each other, they produce a hot dense region between them which rapidly expands and cools. The system then "freezes out" into hadrons, which pass into the detector and can be detected. The energy density ϵ is not directly measurable, but it is correlated with the number and average energy of particles produced at mid-rapidity (around 90°

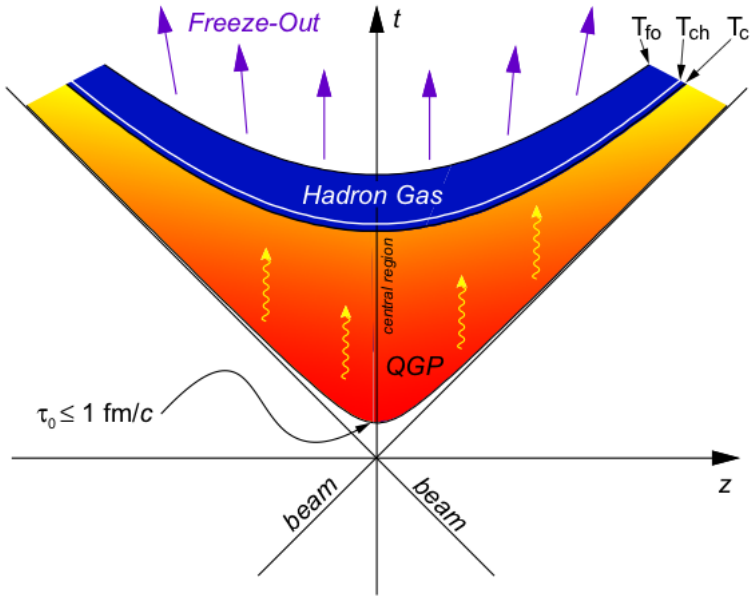

Figure 1.6: Depiction of the time evolution of a heavy ion collision, from the QGP phase, through the hadron gas phase to freeze-out [22].

to the beam direction) as indicated by equation 1.5.

A more detailed depiction of the post-collision time evolution of system is shown in figure 1.6. The initial pre-equilibrium ($t < \tau_0$) stage is thought to be dominated by hard (high Q^2) parton scattering. Multiple parton scatterings then take place, driving the system to an equilibrated QGP phase. The expansion is then driven by hydrodynamic pressure.

As the system expands it cools, with hadrons re-forming as the temperature drops below T_C. At LHC energies of 2.76 TeV per nucleon, this occurs at a time approximately 10 fm/c after the initial collision [23]. Shortly after this, the temperature falls below the chemical freeze-out temperature T_{ch}, after which inelastic scattering does not occur and the hadron species ratios are fixed. Finally, the temperature drops below the kinetic freeze-out temperature T_{f_0} and no more elastic scattering can occur. Barring any subsequent weak decays, the hadrons then pass unchanged to the detectors.

1.3.2 High multiplicity proton collisions

So far this section has described QGP production in heavy ion collisions, which is well established. The systems produced in proton collisions are typically too dilute and small in volume for thermalisation to occur and for QGP to be produced. However, it has been suggested that it may be possible to produce sufficient energy densities for QGP production in a subset of proton collisions in which a suitably large number of particles are produced (as the energy density is correlated with the multiplicity) [24, 25].

Studies of this have been performed at previous experiments, but have thus far yielded inconclusive results [26]. Much greater multiplicities are produced at Large Hadron Collider (LHC) energies, which may imply the production of QGP in the highest multiplicity collisions. The mean charged particle multiplicity has been measured in 7 TeV proton collisions to be $dN_{\mathrm{ch}}/dy = 6.01 \pm 0.01^{+0.20}_{-0.12}$ [27] but the highest produced multiplicities, reaching values of around $dN_{\mathrm{ch}}/dy \approx 60$, are comparable to the multiplicities observed in 200 GeV/nucleon copper collisions at RHIC at which measurable QGP effects were observed [28].

There has also been an observation of an extended ridge structure in dihadron azimuth–pseudorapidity ($\Delta\phi$–$\Delta\eta$) correlations in 7 TeV proton collisions at the LHC [29]. While not yet fully understood, a similar feature was observed in gold collisions at RHIC and so there is interest in whether this could be indicative of QGP production [30]. Whether this observation implies the production of QGP in proton collisions is still debated [31, 32].

If QGP were produced in a proton collision, the initial size would be significantly smaller than that produced in a heavy ion collision, as the proton transverse size (roughly 1 fm) is an order of magnitude smaller than that of a heavy ion. This, combined with the shorter lifetime that results from the smaller size, would lead observable QGP signatures (described in section 1.4) to be less apparent, although

still potentially measurable [25].

1.3.3 Experimental history

Various experimental facilities have been built to attempt to create QGP through heavy ion collisions. While there were earlier attempts at the Alternating Gradient Synchrotron (AGS), the first indications of QGP production were found at fixed target experiments at the CERN SPS [33], which studied lead–lead collisions at a centre of mass energy per nucleon of 19.4 GeV. The peak energy density achieved was estimated to be around 3 GeV/fm^3.

The next experimental facility was the Relativistic Heavy Ion Collider (RHIC) at Brookhaven National Laboratory, a beam–beam collider which produced gold–gold, copper–copper, proton–proton and deuteron–gold collisions at various centre of mass energies per nucleon up to 200 GeV, producing an estimated energy density well in excess of the critical density [18]. A wider range of QGP signatures were observed, which provided greater confidence that QGP had indeed been produced and allowed a more detailed study of its properties [34].

Currently operating is the CERN LHC which, in addition to its proton–proton program, collides lead nuclei up to a current maximum centre of mass energy per nucleon of 2.76 TeV, producing a longer-lived and hotter plasma than previously. A Large Ion Collider Experiment (ALICE) is optimised to study heavy ion collisions at this collider.

1.4 Signatures of quark–gluon plasma production

Various experimental observables have been proposed as signatures to identify the production of QGP as opposed to a hot hadronic gas. Typically, these involve mea-

suring the same observable in minimum bias proton–proton collisions (the ALICE minimum bias trigger is described in section 3.2.6) on the assumption that generally the systems produced are too small to form a QGP. Comparison is then made with heavy ion collisions to identify differences that cannot merely be explained as a superposition of nucleon–nucleon collisons.

Significant observables include enhanced strange particle yield, charmonium suppression, suppression of high momentum particles and hydrodynamic flow. The first two were first observed at the Super Proton Synchrotron (SPS), and the second two were important discoveries at RHIC [34].

1.4.1 Enhanced strange particle yield

One of the key pieces of evidence for the production of QGP at the SPS was the increased production of strange particles (hadrons containing at least one strange quark or antiquark) in nuclear collisions compared with hadronic collisions [33]. This was expected in QGP as the strange quark mass is of similar magnitude to the QGP transition temperature of 170 MeV and so many strange quarks are produced through scattering subprocesses. The dominant subprocess at SPS energies (and above) is gluon-gluon fusion $gg \rightarrow s\bar{s}$ [35].

Strangeness production occurs as a result of the partonic rescattering that drives the system to equilibrium. Analysis of strangeness production rates can therefore provide insight into the equilibration process, an example being at the SPS where it was discovered that the system typically reaches chemical equilibrium after times of the order of 5 fm/c. A system with hadronic degrees of freedom rather than partonic would take around ten times as long to equilibrate via hadron rescattering, and as such would disperse too quickly for this to occur. [35].

After the system cools below T_{C}, the strange quarks hadronise to form strange

hadrons in greater numbers than would be expected in the absence of QGP.

1.4.2 Charmonium suppression

A consequence of the high charm quark mass is that the production of $c\bar{c}$ pairs tends to occur mainly in the early stages of a heavy ion collision. In a medium of sufficient temperature, the Debye screening radius $r_{\mathrm{D}}(T)$ becomes smaller than the relatively large size of bound $c\bar{c}$ states, such as the J/ψ. This suppresses the observed production of these states, whilst production of $\mathrm{D}^{\pm}$ and D^{0} states is enhanced due to the free charm quarks [36].

J/ψ suppression has been measured to be of a similar degree at SPS [37] and RHIC [38] energies. While some degree of suppression would be expected in the absence of a QGP due to cold nuclear matter effects such as hadronic rescattering, the magnitude of these effects was studied in deuteron–gold collisions at RHIC and was determined to be insufficient to account for the observed suppression in ion–ion collisions [39].

Measurements at ALICE at the LHC have indicated the suppression at these energies to be less than that observed at earlier experiments [40]. This is believed to be a consequence of the higher energy densities produced at the LHC, which enhances the production of $c\bar{c}$ pairs. These deconfined quarks are then subject to recombination during hadronisation, which partially compensates for the screening suppression effect [41, 42].

1.4.3 Hydrodynamic flow

Due to the size of heavy nuclei, heavy ion collisions are not typically head-on but instead occur with a degree of overlap. This overlap is quantified by centrality,

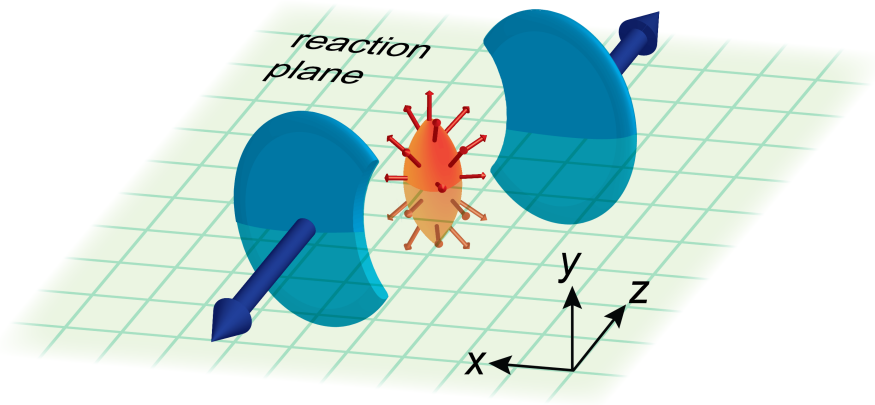

Figure 1.7: Schematic diagram of colliding heavy ions, showing a non-central collision with the interaction plane labelled [44].

ranging from 0%–100% where 0% is the most central (head-on) and 100% is the most peripheral. A three-dimensional view of this, with the reaction plane (the plane defined by the centres of the colliding nuclei and the beam direction) labelled, is shown in figure 1.7. This spatial anisotropy leads to a larger energy density gradient in the reaction plane than perpendicular to it, and hence a larger pressure gradient in this plane [43].

Hydrodynamically, the difference in pressure gradient results in a momentum anisotropy in the final state particle distribution, with particles emitted in the reaction plane having higher p_{T} than those emitted perpendicular to it. This can be measured from the observed particle p_{T} distribution as a function of azimuth. This can be characterised as a Fourier series, the most important component being the second harmonic v_2 which measures the anisotropy between the reaction plane and the perpendicular. This is termed elliptic flow [43].

Measurements of v_2 are typically compared with predictions from relativistic hydrodynamics, assuming a QGP equation of state with quark degrees of freedom. These predictions were shown to describe the data well for lower momentum particles at RHIC [46] and at the LHC [47, 48], providing strong evidence for the production of

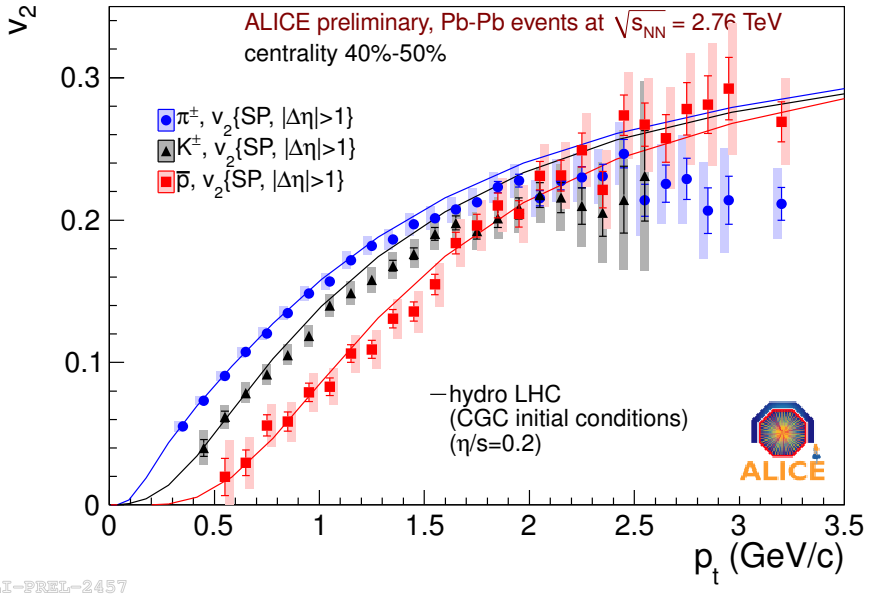

Figure 1.8: Elliptic flow v_2 in the 40%–50% centrality window, measured as a function of p_{T} at ALICE. Hydrodynamic predictions are shown to match the data well at lower p_{T} [45].

QGP; indeed the success of these models has led to the description of the QGP as a "perfect liquid" with very small viscosity.

Figure 1.8 shows such a comparison for identified particles at ALICE, clearly exhibiting the dependence of v_2 on particle type and the accurate description of this by a current "state-of-the-art" relativistic hydrodynamic model, with colour-glass condensate (CGC) initial conditions. The models are not generally applicable at high p_{T}, where particle production is dominated by the scattering of hard partons and their interaction with the medium.

1.4.4 Suppression of high transverse momentum particles

Another key QGP signature is the suppression of particles of high transverse momentum p_{T}. The main production mechanism for high p_{T} hadron production at hadron colliders is jet production, where hard-scattered partons hadronise into collimated cones of hadrons known as jets. Typically this results in pairs of jets (dijets) that

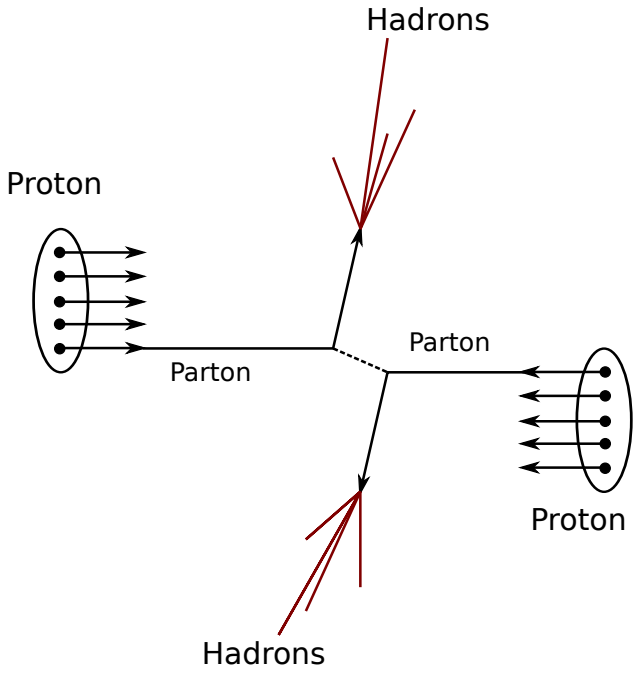

Figure 1.9: Schematic depiction of hard parton scattering leading to dijet production.

are approximately opposite in azimuth (although not in polar angle as the centre of mass frame of the parton–parton collision is generally boosted with respect to the lab frame, as described in appendix A). A simple picture of this is shown in figure 1.9. This observation forms a large part of this thesis and so jet production will be discussed in greater detail later.

Hard scattering in heavy ion collisions occurs early in the timeline of the collision, but the p_{T} of the scattered partons is expected to be significantly attenuated by radiative interactions with the medium; an overview of this attenuation is provided in section 2.2. Due to the reduced p_{T} of the fragmenting parton, the produced hadrons also have reduced p_{T} and so this effect is visible as a reduction in the yield of high p_{T} particles when normalised by the number of nucleon collisions and compared with proton collisions at the same centre of mass energy.

Typically the suppression is quantified with the nuclear modification factor R_{AA}. This is defined as the ratio of the charged particle yield in heavy ion (A–A) collisions

to that in p–p collisions, the yield from proton collisions being scaled by the mean number of binary nucleon–nucleon collisions in the ion collisions $\langle N_{\mathrm{coll}} \rangle$ [49]:

$$R_{\mathrm{AA}}(p_{\mathrm{T}}) = \frac{(1/N_{\mathrm{evt}}^{\mathrm{AA}}) d^2 N_{\mathrm{ch}}^{\mathrm{AA}} / d\eta dp_{\mathrm{T}}}{\langle N_{\mathrm{coll}} \rangle \, (1/N_{\mathrm{evt}}^{\mathrm{pp}}) d^2 N_{\mathrm{ch}}^{\mathrm{pp}} / d\eta dp_{\mathrm{T}}} \tag{1.6}$$

where η is the pseudorapidity as defined in appendix A and $N_{\mathrm{evt}}^{\mathrm{AA}}, N_{\mathrm{evt}}^{\mathrm{pp}}$ are the number of ion and proton events, respectively. $\langle N_{\mathrm{coll}} \rangle$ is calculated from a model incorporating the nuclear overlap and nucleon–nucleon cross sections. A model of this type, used in this analysis to determine the relationship between observed particle multiplicity and collision centrality, is outlined in appendix C.

Thus, a lack of suppression at a given p_{T} would be implied by $R_{\mathrm{AA}}(p_{\mathrm{T}}) = 1$, which would suggest that ion collisions could be viewed as simple superpositions of proton collisions. Observations of $R_{\mathrm{AA}} < 1$ would indicate suppression. Figure 1.10 shows measurements of R_{AA} for a range of p_{T} at the ALICE [49] experiment at the LHC and the STAR [50] and PHENIX [51] experiments at RHIC. This shows R_{AA} values of significantly less than 1, implying a high degree of suppression. It is apparent that more significant suppression was observed at ALICE than at the RHIC experiments, which is interpreted as a consequence of the hotter, longer lived plasma produced at the LHC compared to that produced at RHIC.

As with the charmonium suppression described in section 1.4.2, the possibility of the high p_{T} suppression being caused by cold nuclear matter effects such as gluon shadowing or hadronic scattering was investigated at RHIC through the analysis of deuteron–gold collisions. The lack of suppression in these events provided strong evidence that the observed suppression in heavy ion collisions was indeed indicative of QGP production [52]. A proton–lead collision program was underway at the LHC at the time of writing with the aim of validating the suppression measurements in a similar way.

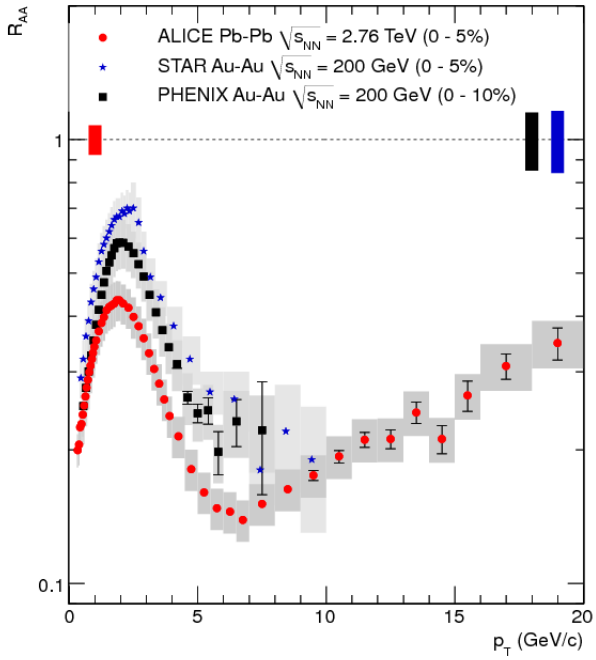

Figure 1.10: Measurements of the nuclear modification factor R_{AA} in central heavy ion collisions at ALICE (LHC) and STAR and PHENIX (RHIC) [49].

1.4.5 Jet quenching

Section 1.4.4 describes the general suppression of high p_{T} particles in heavy ion collisions. However, the degree of attenuation depends on the position and direction of the parton within the geometry of the system: a parton produced by a hard scatter near the edge of a volume of QGP and directed out of the medium would have a shorter path length and suffer less energy loss than one traversing a greater length of plasma.

As depicted in figure 1.11, jet quenching arises when a hard parton is produced in a QGP volume, leading to a reduction in jet p_{T} due to the interaction of the parton with the medium. When a hard parton pair is produced near the edge of the volume, one parton may be directed out of the medium and one azimuthally opposite, as shown in the figure. As the first parton is not greatly suppressed, a high p_{T} jet is still observed in this direction. However, the greater energy loss from the other parton

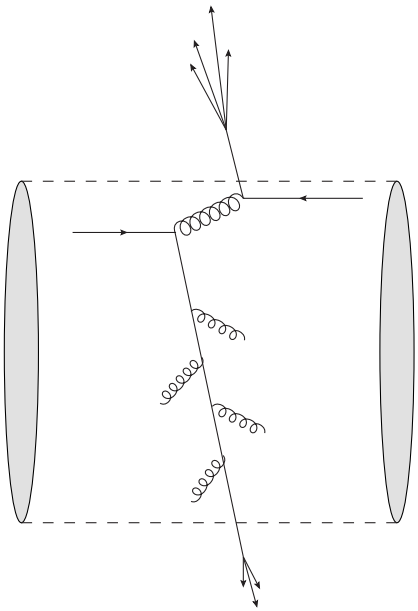

Figure 1.11: Simplified representation of radiative parton energy loss leading to jet quenching, with the observed jets having a momentum asymmetry.

leads to a jet with significantly lower p_{T} such that a jet momentum asymmetry is observed.

In general it is difficult to fully reconstruct jets in heavy ion collisions as the jet energies are typically not sufficiently high to be distinguished from the background; because of this, jet studies have been performed using two-particle angular correlations. In such an analysis, the distribution of angular difference $\Delta\phi$ between particles in defined "trigger" and "associated" p_{T} ranges is produced. Given sufficiently high p_{T} bins, in p–p collisions this produces a characteristic shape of two peaks, centred at $\Delta\phi = 0$ and $\Delta\phi = \pi$, atop a flat non-jet background (which is generally subtracted). This shape appears as a consequence of azimuthally opposite dijet production. However, a p_{T} asymmetry in the jets, due to jet quenching, can lead to the suppression of the awayside ($\Delta\phi = \pi$) peak; this technique was used to provide firm evidence for jet quenching at RHIC [52]. A more comprehensive description of a two-particle correlation analysis is presented in section 4.4.

The degree of this attenuation can be described by the ratio of dihadron yields I_{AA}.

This is defined as

$$I_{\mathrm{AA}} = \frac{Y_{\mathrm{AA}}}{Y_{\mathrm{pp}}} \tag{1.7}$$

where Y_{AA} and Y_{pp} are the yields of hadrons associated with the high p_{T} "trigger" in ion and proton collisions. Typically this quantity is constructed separately for the nearside ($\Delta\phi \approx 0$) and awayside ($\Delta\phi \approx \pi$) peaks, with the difference between these expressing the relative degree of suppression of the awayside jets. Measurements of jet quenching and of the single particle suppression R_{AA} are sensitive to different properties of the medium, for example through the parent parton of an awayside jet necessarily traversing a greater path length through the medium. As such, their combined study allows effective constraint of jet quenching models [53, 54].

Figure 1.12 shows an early measurement in Pb–Pb and p–p collisions at ALICE at the LHC [55]. The awayside peak in peripheral (60%–90% centrality) Pb–Pb is shown to match that for p–p. However, the peak in central (0%–5% centrality) Pb–Pb is suppressed with respect to p–p. This suppression indicates the effect of jet quenching. The $\Delta\phi = 0$ peak is not suppressed in central Pb–Pb as the requirement of "trigger" particles in a given high transverse momentum range preferentially selects events where the jet production occurs near the surface of the QGP volume and thus one jet escapes mostly unattenuated. In the plot shown, this peak can in fact be seen to be enhanced in central Pb–Pb with respect to p–p; the mechanism for this enhancement is not yet well understood.

It has also been suggested that the degree of acoplanarity of a dijet pair with respect to the beam trajectory could be increased as a consequence of interaction of the jets with the medium [56, 57, 58, 59]. The degree of acoplanarity can be determined from the net transverse momentum of a jet pair, which can be extracted from two-particle angular correlations.

At modern hadron collider experiments it is more usual to analyse jets by identifying and reconstructing them on an event-by-event basis. At LHC energies, jets in heavy

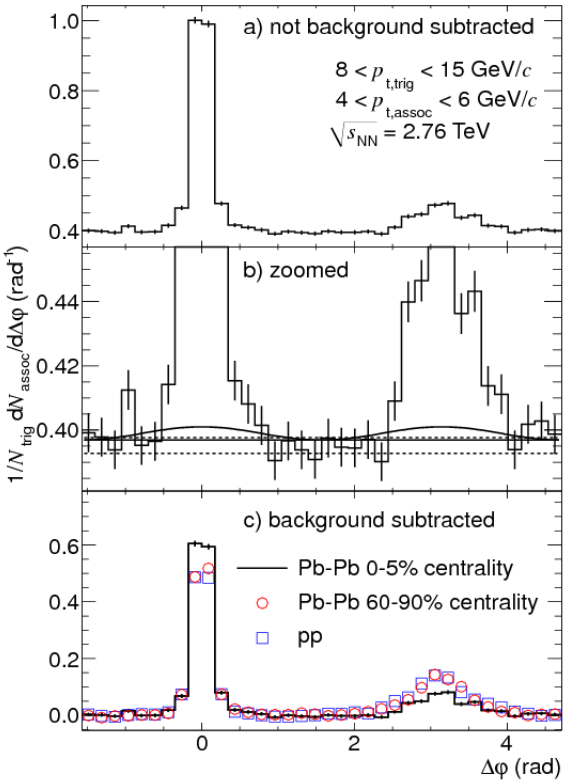

Figure 1.12: Corrected per-trigger pair yield at ALICE, comparing peripheral (60%–90% centrality) Pb–Pb, central (0%–5% centrality) Pb–Pb and p–p. While the awayside yield in peripheral Pb–Pb matches p–p, a suppression with respect to this is observed in central Pb–Pb. This suppression indicates jet quenching [55].

ion collisions are in fact energetic enough that it may be possible to accurately reconstruct them. However, due to the large number of non-jet background particles overlapping with the jet this is still challenging, and correlations remain a valuable technique which allows comprehensive comparison with results from previous experiments.

When taken in combination, measurements of the signatures described in this section provide convincing evidence that a deconfined quark-gluon plasma state is produced in heavy ion collisions at the energies of modern experiments.

1.5 Overview of thesis

This document presents a detailed analysis of jet properties, using the technique of two-particle correlations, in proton–proton collisions at centre of mass collision energies of $\sqrt{s} = 7$ TeV and $\sqrt{s} = 2.76$ TeV and lead–lead collisions at a nucleon–nucleon centre of mass collision energy of $\sqrt{s_{\mathrm{NN}}} = 2.76$ TeV.

Chapter 2 reviews the theoretical background of jet production in proton and ion collisions, including more detail regarding parton attenuation in a deconfined medium than is given in this introduction. Chapter 3 discusses the ALICE experiment at the LHC, at which the analysed data was taken, with particular emphasis given to the detector subsystems relevant to this analysis. The details of the dihadron correlation analysis are then described in chapter 4, including the construction of the correlation functions and the extraction of interesting physical quantities from these. The results of this analysis are then given in chapters 5, 6 and 7. The conclusions drawn from the results are reviewed in chapter 8, and some additional technical details regarding the analysis are presented in appendices: appendix A outlines some kinematic quantities used widely throughout this document, and appendices B and C contain descriptions of the Monte-Carlo models used in the analysis.

CHAPTER 2

THEORETICAL BACKGROUND

2.1 Jets in proton–proton collisions

High p_{T} hadron production in high energy particle collisions, at both e^+e^- and hadron colliders, is characterised by jet production. Jets originate from the production of a pair of high momentum coloured particles which, due to confinement, fragment into collimated jets of hadrons. In e^+e^- collisions, the initial (pre-fragmentation) event involves the production of a $q\bar{q}$ pair via an intermediate photon or Z boson through the process $e^+e^- \to \gamma/Z^0 \to q\bar{q}$.

In hadron collisions, the coloured particle pair is produced through the hard inelastic scattering of the constituent partons of the colliding hadrons, with all possible parton scattering processes contributing to the overall cross section. These constituents can be valence quarks, sea quarks or gluons. By way of example, a diagram showing a

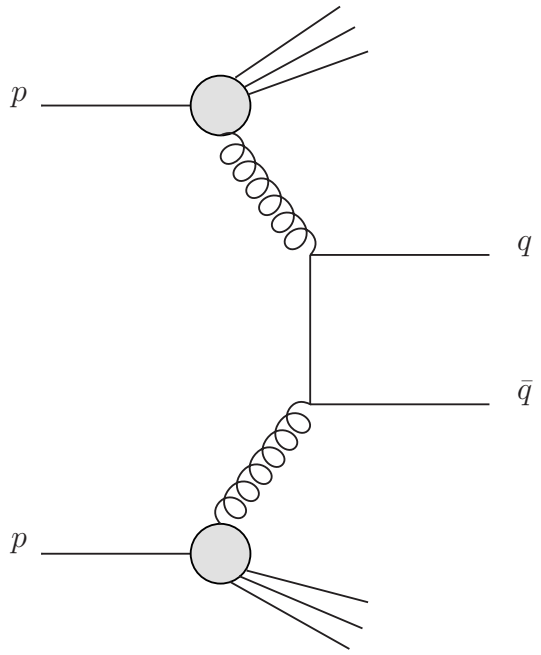

Figure 2.1: Feynman diagram of typical p–p hard scattering event, which would lead to two jets in a detector.

gluon–gluon scattering is shown in figure 2.1.

Hard (high momentum transfer) processes, where the strong coupling α_S is small (as described in section 1.1.3), can be well described by pQCD in much the same way that electroweak theory can be used to describe processes such as e^+e^- scattering. The parton scattering subprocesses fall into this category. However, the momentum distributions of the initial partons within the hadron are incalculable with pQCD as they arise from many soft processes. Despite this, the scattering cross section is independent of the initial parton momentum distribution and the process can be factorised into separate components. Because of this, given a suitable parameterisation of this distribution, the dijet production cross section can be calculated [60, 61].

The momentum distribution of the initial partons is described by parton distribution functions $\mathrm{PDF}(i, x, Q^2)$, where i denotes the type of parton and x the hadron momentum fraction carried by that parton. PDFs are experimentally determined – figure 2.2 shows the current best measurement of the proton PDFs at $Q^2 = 10\ \mathrm{GeV}^2$,

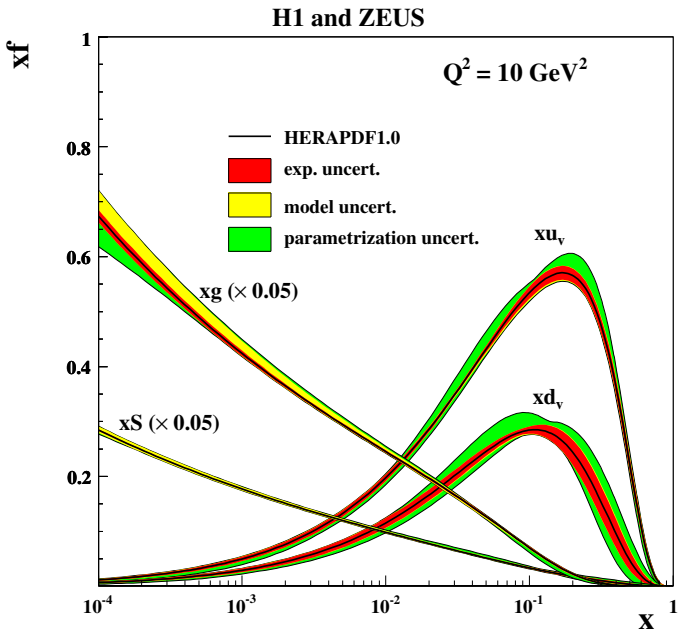

Figure 2.2: Current best fit of the proton parton distribution functions at $Q^2 = 10$ GeV^2, from combined H1 and ZEUS data [62].

from deep inelastic electron–proton scattering at the H1 and ZEUS experiments at HERA [62]. This shows the relative proportion of the different parton types. The fractions of proton momentum carried by valence up quarks, valence down quarks, sea quarks and gluons are given by xu_v, xd_v, xS and xg, respectively. It can clearly be seen that valence quarks contribute significantly at high x, and gluons (and, to a lesser extent, sea quarks) dominate at low x.

The convolution of the PDFs with the hard scattering cross-sections gives the hard parton production cross-section and therefore, as these partons fragment into jets of hadrons, the dijet production cross section. The next stage in the jet production process is the fragmentation of the outgoing partons into hadrons. Fragmentation occurs due to confinement and can be visualised in terms of the stretching of gluon "flux tubes" between partons, as described in section 1.1.2, which repeatedly produce extra parton pairs that together form a jet of hadrons.

The hadrons that form the jet share the momentum of the parent parton and thus

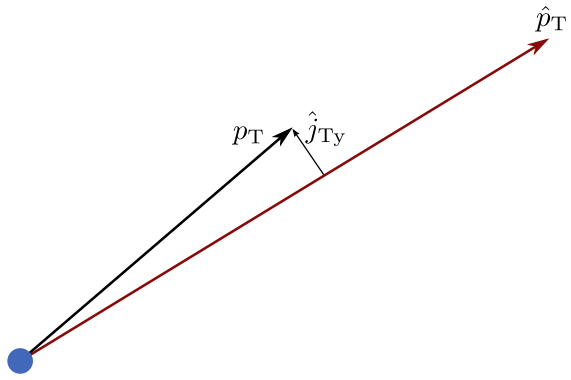

Figure 2.3: Schematic view of the kinematics of the fragmentation process for one jet. The parton and hadron transverse momenta $\hat{p}_{\mathrm{T}}$ and p_{T} are labelled, as is the jet fragmentation transverse momentum component j_{Ty}. Seen in the plane perpendicular to the beam axis.

form a collimated cone shape about the parton momentum axis, with the relative p_{T} of a hadron to its parent parton termed j_{T} (with y component in the azimuthal plane) as shown in figure 2.3. As with the PDFs, the fragmentation process is governed by soft QCD and cannot be calculated perturbatively. The results of parton fragmentation are instead described by empirical fragmentation functions $D(h, z, Q^2)$, which give the probability distribution for the production of hadrons h with momentum fraction z of the parent parton. Assuming the fragmentation process to be independent of both the hard parton production and of the proton collision underlying event, the fragmentation functions can be measured in the comparatively clean environment of e^+e^- collisions and the results applied to hadron collider physics [63].

This principle of the independence of the fragmentation function and hard cross section (and also of the PDFs) is known as factorisation and is an important QCD concept. The main consequence of factorisation is that the empirical fragmentation functions and PDFs can be determined separately and convolved with the hard scattering cross section, calculated using pQCD, to give the overall hadron production

cross section due to jets. This can be written schematically as

$$\sigma = \sum_{abcd} \int dx_a dx_b dz \ \mathrm{PDF}(i_a, x_a, Q^2) \ \mathrm{PDF}(i_b, x_b, Q^2) \otimes \sigma_{ab\to cd} \otimes D(h, z_c, Q^2) D(h, z_d, Q^2)$$

with the sum over all parton scattering subprocesses $a + b \to c + d$.

2.1.1 The k_T effect

If parton collisions were collinear with the p–p collision axis, the two emerging partons in a hard scattering event would have equal transverse momentum and opposite azimuth. Any initial partonic p_T, denoted k_T, would cause a deviation from this, with the scattered partons having net transverse momentum $\langle p_\mathrm{T}^2 \rangle_\mathrm{pair} = 2 \cdot \langle k_\mathrm{T}^2 \rangle$. It might be naïvely expected that the partons would have $k_\mathrm{T} \sim 300$ MeV, due to the size of the proton [64]. However, this was observed [65] to not be the case, and a study by the CERN-Columbia-Oxford-Rockefeller (CCOR) collaboration found k_T to be dependent on the centre of mass energy $\sqrt{s}$ and to have a value as high as $\langle |k_{\mathrm{T}y}| \rangle \sim 0.8$ GeV (giving $\sqrt{\langle k_\mathrm{T}^2 \rangle} \sim 1.1$ GeV from the geometric relationship $\sqrt{\langle k_\mathrm{T}^2 \rangle} = \sqrt{\pi} \langle |k_{\mathrm{T}y}| \rangle$, where $k_{\mathrm{T}y}$ is the component of k_T perpendicular to the transverse momentum of the other hard parton (typically this is defined relative to the highest p_T parton) [66]) for the highest energy collisions at the Intersecting Storage Rings (ISR), with $\sqrt{s} = 62$ GeV [67].

Measurements of k_T were subsequently performed at other experiments, the results of many of which are collected in figure 2.4 [66]. This demonstrates clearly that k_T is both significantly larger than the naïve expectation and that it increases, approximately logarithmically, with $\sqrt{s}$.

It was subsequently realised that the only satisfactory explanation for this behaviour was that k_T had a radiative origin (in addition to the intrinsic part already expected).

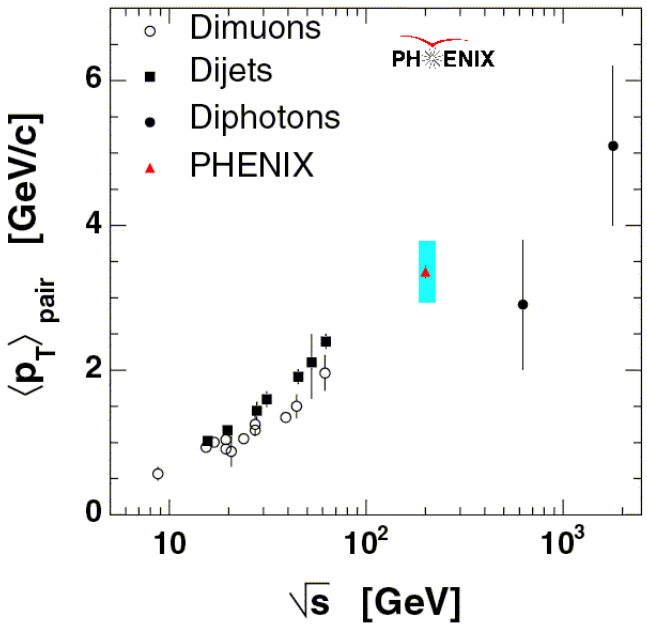

Figure 2.4: Net pair p_{T} measurements in proton collisions over a range of $\sqrt{s}$, illustrating a clear dependence [66].

It is now understood that k_{T} is composed of three components

$$\langle k_{\mathrm{T}}^2 \rangle = \langle k_{\mathrm{T}}^2 \rangle_{\mathrm{intrinsic}} + \langle k_{\mathrm{T}}^2 \rangle_{\mathrm{NLO}} + \langle k_{\mathrm{T}}^2 \rangle_{\mathrm{soft}} \tag{2.1}$$

where "intrinsic" refers to the aforementioned component of roughly 300 MeV due to the proton size, "NLO" refers to next to leading order corrections (the radiation of an initial or final state hard gluon) and "soft" refers to the QCD radiation of soft gluons, which is explained by resummation [68]. It was found by the E706 collaboration at Fermilab that the observed k_{T} values cannot be explained by the intrinsic and NLO components alone, and that the soft component is essential to explain the observations. Indeed, it is believed that at collider energies the soft component is dominant [69].

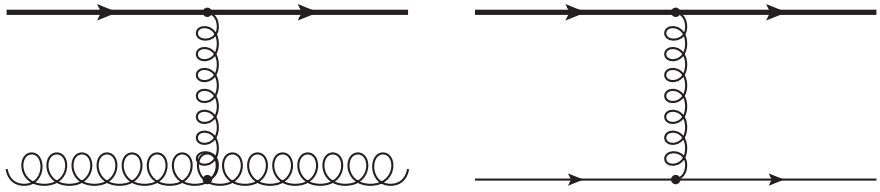

(a) Scattering from thermal gluons and quarks.

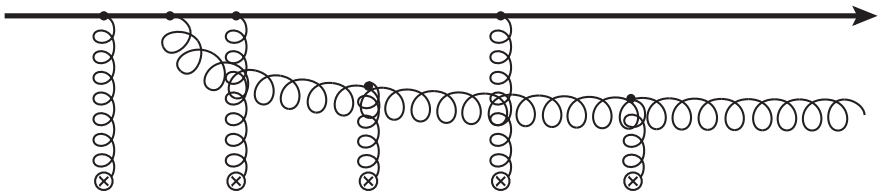

(b) Radiation.

Figure 2.5: Energy loss mechanisms of hard partons in QGP.

2.2 Jets in heavy ion collisions

It is assumed that hard parton scattering in heavy ion collisions should behave the same as in proton collisions and so, assuming the usage of appropriate PDFs (modified to take into account the effects of the nuclear medium), it is possible to calculate a dijet cross section in much the same way as for proton collisions. However, the evolution of the system after the initial hard scattering takes place in a medium very different from the vacuum of proton collisions. Significant suppression of high p_{T} particles (and jets) is expected relative to the yield observed in p–p collisions, indeed this suppression is regarded as a signature of the production of QGP (as introduced in section 1.4).

Colour charges (partons) traversing a colour-deconfined medium are expected to lose energy through interactions with that medium, with those interactions being either collisional or radiative. Collisional energy loss was the first type to be considered (by Bjorken [70]), with interactions of this type involving the scattering of fast partons from thermal quarks and gluons in the medium as depicted in figure 2.5a.

The other type of energy loss is radiative energy loss. Fast partons lose energy in

this manner by interacting with scattering centres and emitting gluon radiation, in a manner analogous to the emission of bremsstrahlung photons in electromagnetic plasmas. A representation of such an interaction is shown in figure 2.5b [71]. All models of radiative parton energy loss must include the Landau-Pomeranchuk-Migdal effect, whereby gluon radiation is suppressed due to interaction between the parton and the radiated gluon [72, 59].

As well as energy loss, as stated in section 1.4.5 it has been suggested that medium interactions could increase the acoplanarity of a jet pair with respect to the beam trajectory [56, 57, 58, 59]. Any acoplanarity is measurable as a non-zero k_{Ty}, and so measuring the p_{T} imbalance in heavy ion collisions could provide a measure of the degree of suppression.

2.2.1 Parton attenuation models

The first main approach to modelling radiative parton energy loss, known as BDMPS (Baier-Dokshitzer-Mueller-Peigne-Schiff), models attenuation by the emission of multiple soft gluons [72]. The second, known as GLV (Gyulassy-Levai-Vitev) models instead the emission of one or a small number of hard gluons [73]. Typically in either of these approaches, for a finite volume of QGP, the parton energy loss is not strongly dependent on the initial parton energy (except for it setting an upper bound on the total energy loss).

The models differ regarding the thickness of plasma that they describe. BDMPS calculations assume that the plasma is relatively thick and static, with the hard partons being sufficiently energetic that the path length traversed L (defined by the size of the plasma) is less than a critical length $L < L_{\mathrm{cr}} = \sqrt{\lambda_{\mathrm{g}} E/\mu^2}$, where λ_{g} is the radiated gluon mean free path and $\mu = 1/R_{\mathrm{Debye}}$ is the Debye screening mass of the medium. In models of this type the energy loss ΔE is proportional to L^2.

In contrast, GLV calculations are applicable to "thin" plasmas which are not significantly larger than the mean free path, where the BDMPS approximations do not apply. In this situation it is appropriate to assume that only a small number of gluon emissions take place [73]. From this model it can be shown that $\Delta E \propto L$.

The other main radiative energy loss formalisms are higher twist (HT) [74] and Arnold-Moore-Yaffe (AMY) [75], both of which attempt to create a fuller quantum field theoretic approach. AMY in particular is based entirely on pQCD, with the consequence that it is limited to describing only plasmas of very high temperature $T \gg T_{\mathrm{C}}$ [59].

The models of parton energy loss outlined above generally relate the energy loss to primary model parameters which characterise the medium. For example, in the BDMPS approach the energy loss is related to the transport coefficient $\hat{q} = \langle q_{\mathrm{T}}^2 \rangle / L$, where q_{T}^2 is the transverse energy squared transferred to the traversing parton. This is in turn related to the gluon density in the medium. The primary parameters in the other models, for example the opacity (related to the screening length and mean free path) in the case of the GLV approach, are typically translated into effective transport coefficients [59].

Figure 2.6 shows measurements of parton energy loss, quantified by R_{AA}, from the ALICE experiment alongside results from various models [49, 76]. It can be seen that it is difficult to discriminate between the different models by studying R_{AA} alone, as the data are well described by both purely collisional and purely radiative models. This is attributed to the dependence of R_{AA} on the initial conditions and evolution of the system, which cannot be solely characterised by the (effective) transport coefficient [77].

These models describe the general suppression of high p_{T} particles in heavy ion collisions. However, the dependence on path length leads to the conclusion that the degree of attenuation depends on the position and direction of the parton within

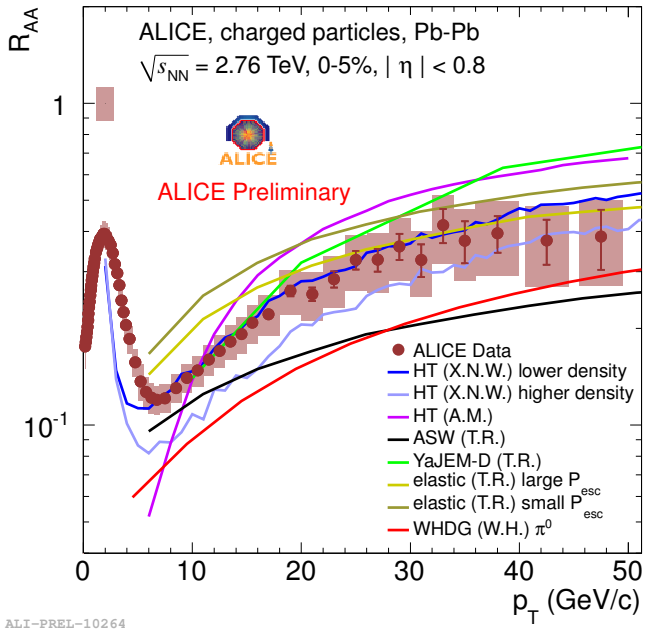

Figure 2.6: Measurements of the nuclear modification factor R_{AA} in central heavy ion collisions at ALICE, compared with various models [76].
HT, ASW and YaJEM are purely radiative models; the elastic models are purely collisional; WHDG includes radiative and collisional energy loss.

the geometry of the system: a parton produced by a hard scatter near the edge of a volume of QGP and directed out of the medium would have a shorter path length and suffer less energy loss than one traversing a greater length of plasma. This can lead to a measurable jet momentum asymmetry, as described in section 1.4.5.

This dependence on path length also has consequences for the potential observation of QGP in proton collisions, which is described in section 1.3.2. If QGP production were to occur in such collisions, the volume would be very small compared with that produced in heavy ion collisions and as such, parton path lengths would be small and the degree of quenching would not be as great. This would make it harder to observe.

CHAPTER 3

THE ALICE EXPERIMENT AT THE LHC

This chapter describes the LHC, a particle accelerator at CERN on the French-Swiss border, in section 3.1. The ALICE experiment at the LHC is then described in section 3.2, with particular emphasis on the subsystems which are relevant to the two-particle correlation analysis described in chapter 4. These subsystems are the Inner Tracking System (ITS) (section 3.2.3) and Time Projection Chamber (TPC) (section 3.2.4) for tracking, and additionally the V0 (section 3.2.5) for triggering. The triggering and reconstruction mechanisms are also described, in sections 3.2.6 and 3.2.7, respectively.

3.1 The Large Hadron Collider

The Large Hadron Collider (LHC) is a two-ring hadron synchrotron, 26.7 km in circumference and 45–70 m underground, located in the tunnel originally constructed for LEP. Each ring (composed of curved and straight sections) can accelerate either protons or lead nuclei in opposite directions about the ring and collide them at four crossing points. At design energy it will be able to collide protons at $\sqrt{s} = 14$ TeV and lead nuclei at $\sqrt{s_{\mathrm{NN}}} = 5.5$ TeV, although at the time of writing the highest energies achieved were $\sqrt{s} = 8$ TeV and $\sqrt{s_{\mathrm{NN}}} = 2.76$ TeV for protons and lead, respectively [78]. Collisions of lower-mass nuclei have also been proposed, but this had not been implemented at the time of writing [79].

The beams are steered around the ring by dipole magnets with a peak field of 8.33 T and are focussed by quadrupole magnets. The acceleration occurs within a single straight section of the ring, containing an array of 400 MHz radio frequency (RF) cavities [78]. The two-ring structure is necessary as, unlike previous hadron colliders which typically studied proton–antiproton collisions, the LHC circulates two beams of positively charged particles. This requires the bending magnetic field for the clockwise beam to be in the opposite direction to that for the anticlockwise beam.

Four main experiments are positioned around the LHC ring, one at each of the four crossing points. These are ALICE, optimised to study ion collisions, the general-purpose experiments ATLAS and CMS, and LHCb, optimised for the study of b physics. The layout of these experiments and the accelerating RF cavities around the LHC ring is shown in figure 3.1.

Protons or lead nuclei are passed through a chain of accelerators prior to being injected into the LHC [80]. Protons are supplied by a proton source, which strips hydrogen atoms of their electrons and injects them into a linear accelerator (LINAC2) in which they are accelerated to 50 MeV prior to injection into the Proton Synchrotron Booster (PSB). The PSB accelerates the protons to 1.4 GeV before inject-

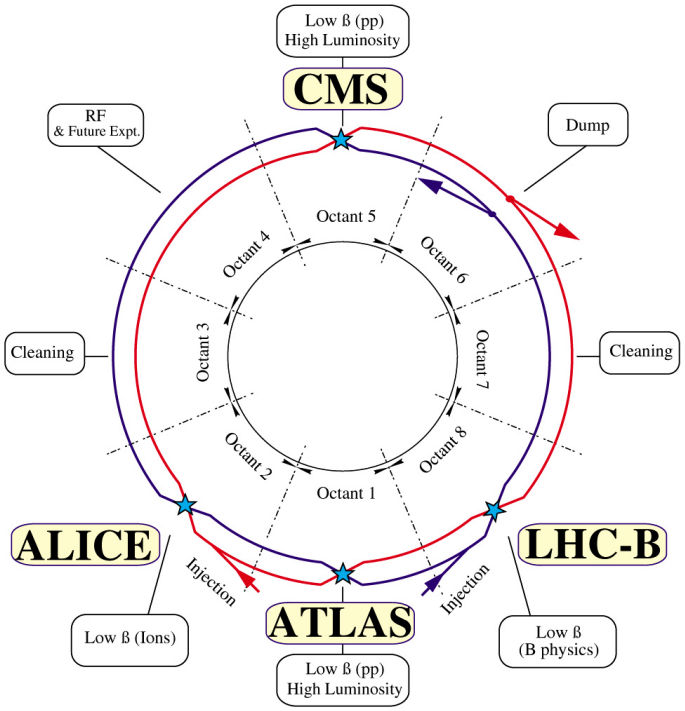

Figure 3.1: Schematic depiction of the LHC ring, showing ALICE at point 2 [78].

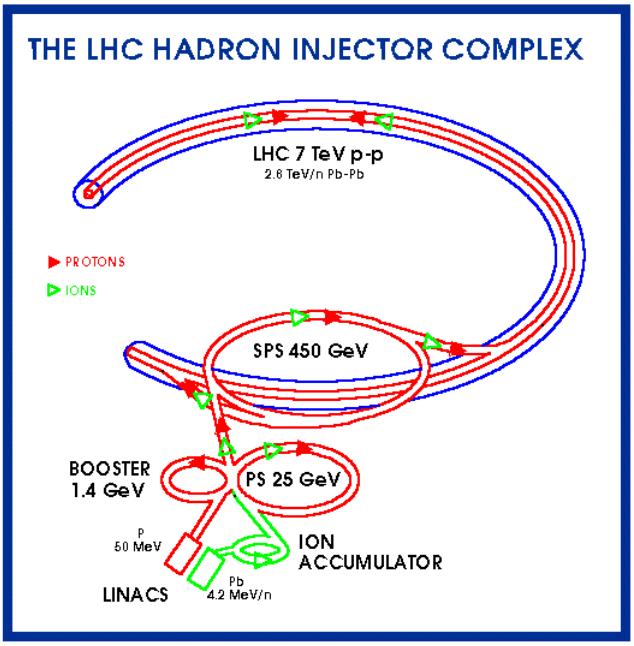

Figure 3.2: The chain of accelerators leading to the LHC, for both protons and lead ions [80]

ing them into the Proton Synchrotron (PS), in which they are accelerated to 25 GeV before being fed into the SPS. In the SPS the protons are accelerated to 450 GeV, after which they are injected into the LHC. This accelerator chain is shown in figure 3.2.

The hadrons undergoing acceleration are collected in bunches, with a separation between bunches of 25 ns at maximum capacity. One beam can circulate up to 2808 of these bunches, which have a typical transverse size when far from the detectors of the order of 1 mm and a length of a few centimetres. The bunches are squeezed by focussing magnets to a transverse size of approximately 16 µm at the interaction points to maximise the collision rate in the experiments.

To produce lead beams, ^{208}Pb atoms are stripped of their electrons by being passed through a series of foils. The nuclei are then accelerated in a linear accelerator (LINAC3), followed by the Low Energy Ion Ring (LEIR). The ions are then injected into the PS, after which they follow the same accelerator chain as described for protons (albeit at a correspondingly reduced energy per nucleon).

The design p–p collision luminosity is $L = 10^{34}$ cm^{-2} s^{-1} which, combined with the total inelastic p–p collision cross section of $\sigma_{\text{inel}} = 69.4$ mb at $\sqrt{s} = 7$ TeV [81], gives an event rate of 700 MHz. The highest produced luminosity across all of the LHC experiments at the time of writing is 7.7×10^{33} cm^{-2} s^{-1}, with the value in ALICE typically being around 10^{30} cm^{-2} s^{-1} (leading to an event rate of around 10^5 Hz).

When running with lead beams, the average produced luminosity to date was measured to be 5×10^{23} cm^{-2} s^{-1}, giving a hadronic collision rate of approximately 4 Hz. The overall interaction rate was around 50 Hz, but the majority of this was due to electromagnetic processes which are easily rejected due to their low produced multiplicity [82].

3.2 The ALICE detector

3.2.1 Detector overview

A Large Ion Collider Experiment (ALICE), measuring $16 \times 16 \times 26$ m^3 and situated at point 2 on the LHC ring, is optimised to focus on the Pb–Pb collisions at the LHC as opposed to the p–p collisions that are the focus of the other experiments. In particular, this required the design to take into account the very large track multiplicity expected in ion collisions, roughly three orders of magnitude larger than that of typical p–p collisions and a factor of two to five higher than the largest multiplicities observed at RHIC. ALICE was tested with simulations of up to $dN_{\text{ch}}/d\eta = 8000$ [83], significantly higher than the value of $dN_{\text{ch}}/d\eta = 1601 \pm 60$ measured at the LHC in central Pb–Pb collisions at mid-rapidity [84].

The layout of the detector is illustrated in figure 3.3. The central barrel, centred on the interaction point, is contained within a large solenoidal magnet which produces a uniform field of 0.5 T. This causes particle paths within the detector to curve,

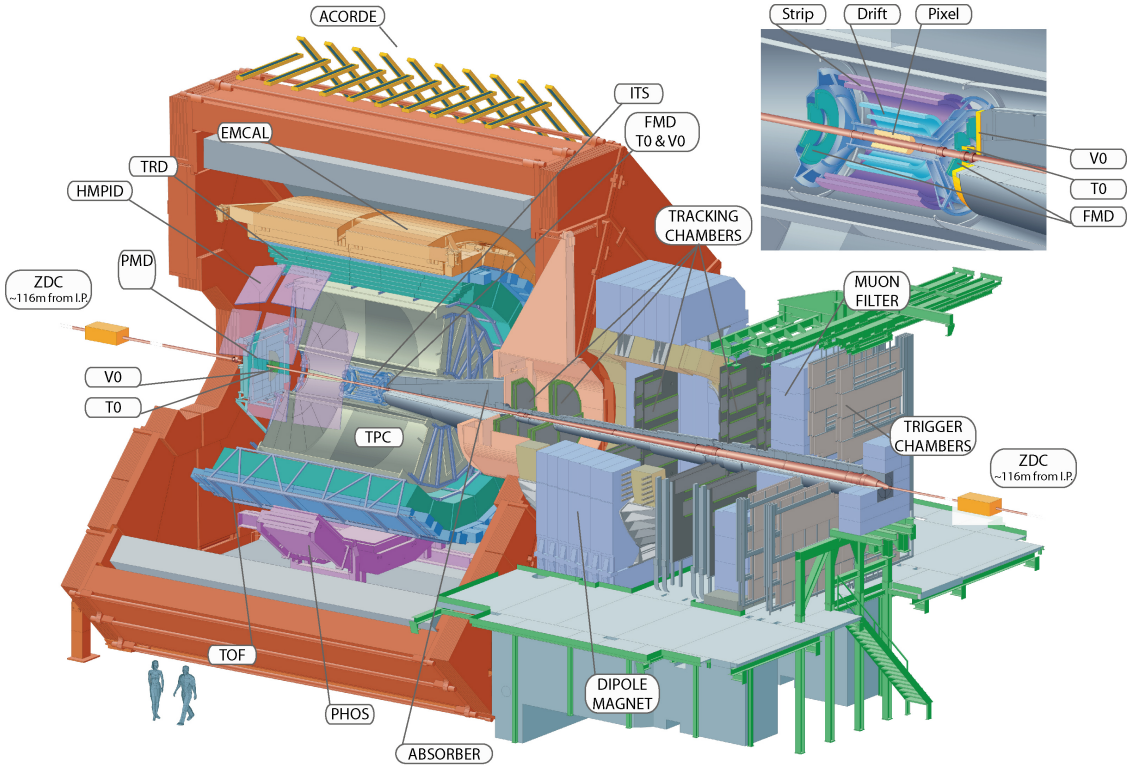

Figure 3.3: Layout of the ALICE detector [83].

allowing their momentum to be measured as described in section 3.2.7. The central barrel comprises many concentrically layered detector systems for charged particle tracking, calorimetry and particle identification (PID), most of which cover the pseudorapidity range $-0.9 < \eta < 0.9$ and the full range of azimuthal angle $0 < \phi < 2\pi$. Transverse momentum is measurable over a large range from around 100 MeV up to over 100 GeV, and PID is also possible over much of this range. The analysis presented in this document required only charged unidentified hadrons, and so of the central barrel detectors only the tracking detectors were used. These, the ITS and TPC, are described later in this section.

In addition to the central barrel detectors, there exist detectors at larger pseudorapidity to detect particles with paths closer to the beamline. Mostly these detectors, such as the multiple components of the forward muon arm, were not used in this analysis. However the V0, a particle counter with a fast response, is used for minimum bias triggering and is described later in this section.

3.2.2 Coordinate system

A standard set of coordinates is used when describing directions and angles in the ALICE experiment. The origin of both coordinate systems defined here is set to the intersection of the beamline and the central membrane of the TPC, in the mid-point of the central barrel.

Cartesian x, y, z

The x-axis points to the centre of the LHC; the y-axis points vertically upwards; the z-axis is parallel to the beam direction and points towards the muon arm end of the detector.

Cylindrical polar r, θ, ϕ

r is the radial distance perpendicular to the beam pipe. θ and ϕ are polar and azimuthal angles with respect to the beam pipe (z-axis), although pseudorapidity η (as defined in appendix A) is typically used instead of θ.

Sides A and C

The A side of the experiment is the side closest to the main CERN site, and the C side is the side furthest away. The muon arm is located on the C side.

3.2.3 Inner tracking system

The Inner Tracking System (ITS) consists of six concentric cylindrical layers of silicon detectors, located immediately around the interaction point and covering the pseudorapidity range $|\eta| \leq 0.9$. As depicted in figure 3.4, from inner to outer these six layers comprise two layers of Silicon Pixel Detector (SPD), two layers of Silicon Drift Detector (SDD) and two layers of Silicon Strip Detector (SSD). The main design consideration is the high multiplicity expected in ion collisions, which necessitates a very high granularity in the tracking detectors close to the beam line

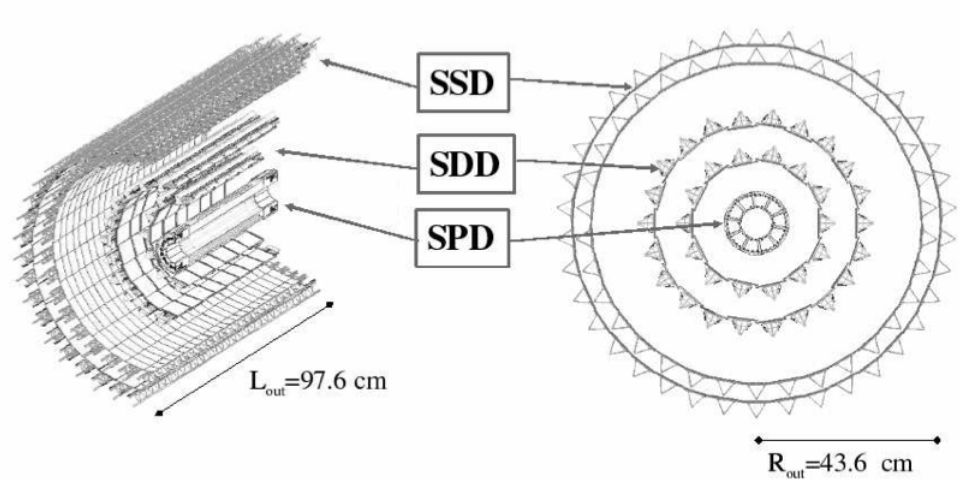

Figure 3.4: Cross section of the ALICE inner tracking system [83].

– in the innermost layer, with its radius at the minimum allowed by the beam pipe, track density can be as high as 90 cm^{-2}. This granularity can only be achieved through the use of silicon detectors.

The primary functions of the ITS are vertex determination (including separation of secondary vertices), tracking of low-momentum particles and improvement of the momentum and angle measurements of the TPC [85]. It is particularly important for the measurement of particles of momentum lower than 200 MeV, which do not reach the TPC and thus only appear in the ITS.

Silicon pixel detector

The SPD comprises the innermost two layers of the ITS, positioned at radii $r = 3.9$ cm and $r = 7.6$ cm. The SPD is finely segmented in two dimensions (perpendicular to the ϕ direction), localising a particle passing through by detecting a signal in one of its 9×10^6 cells. This gives it the highest precision of the ITS components, with a spatial resolution of 12 µm in $r\phi$ and 100 µm in z. Its proximity to the interaction point means that the SPD must be extremely radiation hard – the estimated total dose over 10 years of running is 220 krad [86].

Short tracks known as "tracklets" can be formed from two SPD hits, with no other tracking information required. The number of these tracklets can provide a measurement of charged particle multiplicity sensitive to very low momentum particles. In addition to tracking, the SPD also contributes to the minimum bias trigger, as described in section 3.2.6.

Silicon drift detector

The middle two layers, at $r = 15.0$ cm and $r = 23.9$ cm, of the ITS are SDDs. These are finely segmented in one direction but coarsely in another, with track position in this dimension reconstructed by measuring the drift time of the produced charge to the electrode. This allows accurate hit location, with a resolution of 38 µm in $r\phi$ and 28 µm in z, at the expense of being limited in the event rate that they can accommodate – the ALICE SDD is configured for a maximum drift time of 6 µs [85]. As such, this type of detector is well suited to the high multiplicity, low frequency events produced in heavy ion collisions.

Silicon strip detector

The outer two layers of the ITS, at $r = 38.0$ cm and $r = 43.0$ cm, consist of double-sided SSDs. These are finely segmented in one direction but coarsely in the perpendicular direction, localising a particle to a single one of these strips. The two sides are at a relative angle of 35 mrad to allow two-dimensional reconstruction of a hit position with a resolution of 20 µm in $r\phi$ and 830 µm in z. This type of detector is only suitable at these larger distances from the interaction point, where the track density is typically less than 1 cm^{-2}, as in a higher density environment difficulties in the attribution of points to a given track could lead to ambiguity in the reconstruction [85]. The SSD layers are particularly important for track matching between the ITS and TPC.

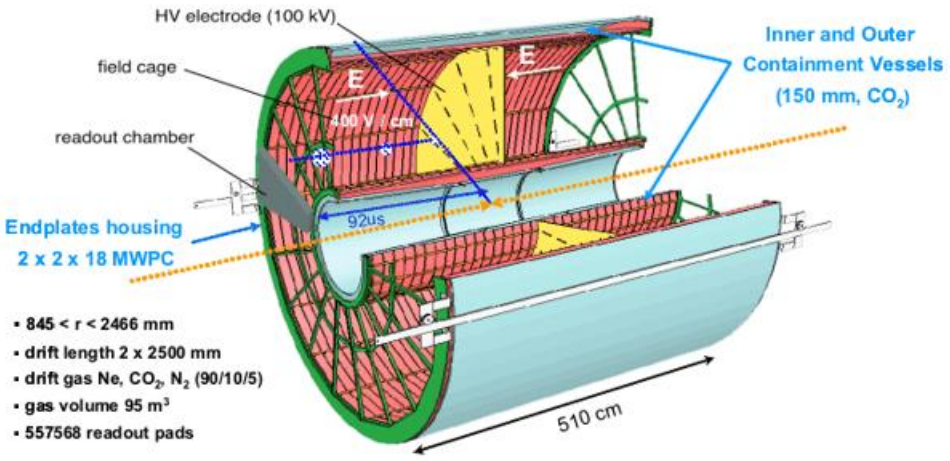

Figure 3.5: Layout of the TPC [87].

3.2.4 Time projection chamber

The Time Projection Chamber (TPC), located outside the ITS, is the main tracking system of the central barrel of the detector and (as with the other central barrel detectors) is optimised to provide a charged particle momentum measurement with good two-particle separation, PID and vertex determination [83]. For tracks with full radial track length it covers $|\eta| \leq 0.9$, and coverage up to $|\eta| \approx 1.5$ is possible with reduced track length (to a minimum of one third of the total radial track length) and correspondingly lower momentum resolution. The full range of azimuth is covered, with momentum resolution better than 1% for tracks with p_{T} between 0.2 and 1 GeV, around 5% for tracks of $p_{\mathrm{T}} \approx 10$GeV, and rising to 30% for tracks of up to 100 GeV. As with the ITS a significant factor in the design was the high track multiplicities expected with a theoretical maximum of 2×10^4 tracks over the full volume, an unprecedented multiplicity for a TPC [83].

TPCs are a form of gaseous tracking detector and are essentially very large-volume drift chambers with multi-wire proportional chambers (MWPCs) at one or both ends (both in the case of ALICE [88]). Due to their very low material thickness, they cause minimal scattering of the passing particles. This, combined with their excellent two-

track separation, is desirable in the high multiplicity environment produced in ion collisions. As with drift chambers, charged particles passing through ionise atoms of the gas, liberating electrons. These electrons then drift in a uniform electric field towards the MWPC, producing an electron shower when they approach the MWPC anode wires and are accelerated by the stronger electric field near the wires. This shower is then detected from the charge induced on cathode pads [89].

The long drift time of a TPC (up to approximately 92 µs at ALICE [83]) limits the maximum collision rate that can be accommodated. Full three-dimensional information can be read out: x and y from the two dimensionally segmented cathode pads and z from the drift time.

The ALICE TPC is cylindrical with inner radius roughly 85 cm, outer radius roughly 250 cm and longitudial length of 500 cm; a cutaway diagram of its structure is shown in figure 3.5. It contains 90 m^3 of $Ne/CO_2/N_2$ in a 90:10:5 ratio at atmospheric pressure; this mixture is optimised for low diffusion perpendicular to the drift direction and low radiation length (minimising multiple scattering). It is separated by a central cathode, and electrons drift up to 2.5 m from either side of this to MWPCs at either end plate.

The end plates are shown in figure 3.6; the MWPCs comprise 18 trapezoidal sectors. The entire TPC is contained within a field cage to permit the extremely uniform electric field (of 400 V/cm) that is required in such detectors. It provides a position resolution of 800–1100 µm ($r\phi$) by 1100–1250 µm (z), the exact value depending on the particle position within the detector [83].

3.2.5 V0

The V0 comprises two arrays of plastic scintillator counters at small angles to the beam pipe – the V0A on the A side covering the pseudorapidity range $2.8 < \eta <$

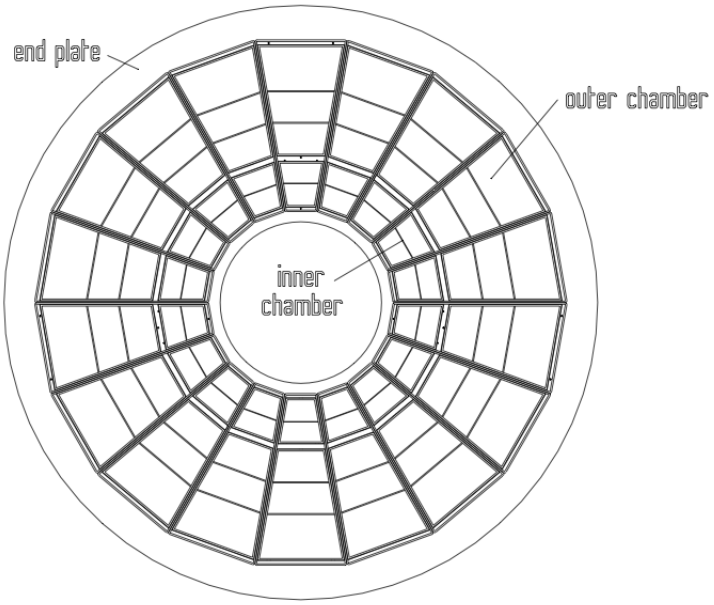

Figure 3.6: Segmentation of the ALICE TPC end plates [88].

5.1, and the V0C on the C side covering the pseudorapidity range $-3.7 < \eta < -1.7$. The V0A and V0C are positioned 340 cm and 90 cm from the interaction point, respectively, this difference being due to the limitations on available space on the C side imposed by the large muon absorber. This asymmetry leads to the aforementioned difference in pseudorapidity coverage of the two arrays.

Each V0 array is coarsely granular, being composed of four concentric rings of eight scintillator counters apiece. Its main relevance to the analysis presented here is its contribution to the minimum bias trigger, as described in section 3.2.6. It can also be used for a centrality trigger in heavy ion collisions, and for elimination of beam–gas interactions – the relative timing of signals in the two arrays can be used to distinguish a collision that occurred at the interaction point from one occurring elsewhere along the beamline.

3.2.6 Triggering

Typically at modern high energy physics experiments, including those at the LHC, the collision rate is far in excess of the capacity to store the resulting data. This necessitates some form of triggering to preferentially select interesting events for storage and analysis.

Central Trigger Processor

The triggering in the ALICE experiment is controlled by the Central Trigger Processor (CTP) hardware, located adjacent to the detector to minimise the latency. The CTP can receive up to 24 inputs from triggering detectors (additional detectors can be read out only, playing no role in triggering) and pass trigger signals to detectors via Local Trigger Units (LTUs). There exist three levels of trigger: L0, L1 and L2 [83].

Initially, if the inputs satisfy defined L0 conditions (typically indicating that at least one fast detector, such as the V0, has detected a possible event) and if no vetoes occur (see below for examples of possible vetoes), an L0 signal is generated which initiates the processing of the event by the read out detectors. This fast decision typically reaches the detectors within 1.2 µs of an interaction. If further, more restrictive, conditions are met, an L1 signal is generated and following this, processing of the event either continues or is terminated. Finally, after additional conditions are tested, an L2a (accept) or L2r (reject) signal is generated; if the read out detectors receive an L2a signal the event data is read out to the Data Acquisition (DAQ). This occurs roughly 88 µs after the interaction, approximately equal to the drift time of the TPC.

The CTP can be connected to 24 L0 inputs, 24 L1 inputs and 12 L2 inputs. Up to 50 trigger classes can be defined, each comprising a logical combination of these inputs.

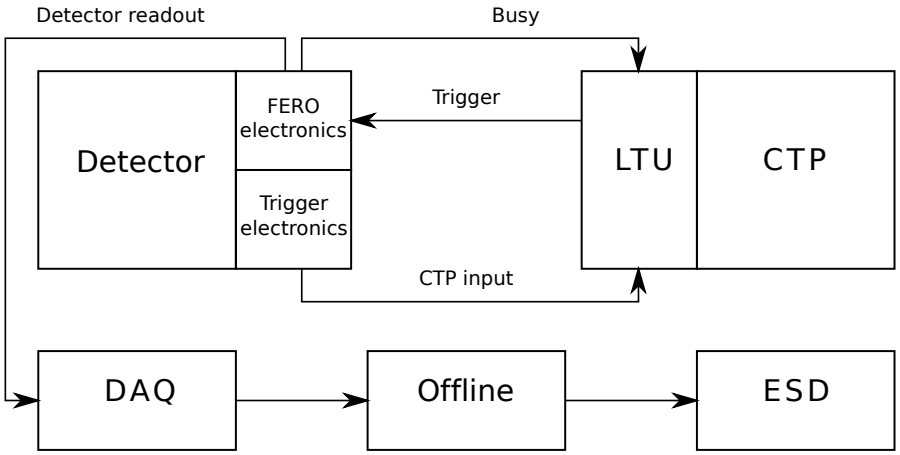

Figure 3.7: Schematic diagram of the triggering and read out process (adapted from [91]). One trigger detector and corresponding LTU is shown.
CTP: Central Trigger Processor; DAQ: Data Acquisition; ESD: Event Summary Data; FERO: Front-end Read out Electronics; LTU: Local Trigger Unit.

A class then triggers the read out of one of up to 6 defined clusters of detectors [90].

A trigger class can be vetoed if one of various conditions are met. Some examples are:

Detector busy A detector in the corresponding cluster is busy (indicated by a busy signal to the LTU), and thus cannot be read out.

CTP busy The CTP cannot process L0 signals with a spacing closer than 1.6 µs.

DAQ busy If the bandwidth of the connection to the DAQ is exceeded, the DAQ can veto further triggers.

Downscaling To protect rare triggers from being overwhelmed by common ones saturating the read out, trigger classes can have their rates downscaled by the CTP.

A schematic diagram of the flow of data through the triggering and read out process is shown in figure 3.7.

Triggers used in this analysis

The most basic trigger is a so-called minimum bias (MB) trigger which is optimised to select inelastic events with as little physics bias as possible, to produce a selection of the most typical events (with no preference for any rare characteristics). The ALICE p–p minimum bias trigger requires at least one hit in the V0A, or the V0C, or the SPD. Each SPD chip produces a Fast-OR signal for this purpose, indicating that a hit has occurred on at least one of the pixels on that chip [92]. This signal is fast enough to be used as an input to the L0 trigger; the full information is then read out later if the trigger is not vetoed.

For the Pb–Pb collisions studied in this analysis the minimum bias trigger was slightly different, requiring hits in at least two out of the V0A, V0C, or SPD.

Due to the steeply falling nature of the multiplicity spectrum, as demonstrated in figure 3.8, the majority of events selected by a minimum bias trigger have a relatively low multiplicity. For an analysis of high multiplicity p–p events, it is therefore advantageous to have a trigger that selects only high multiplicity events. The ALICE high multiplicity (HM) trigger was defined to require at least 60 fired chips in the outer layer of the SPD, and was active during the LHC10e period of $\sqrt{s} = 7$ TeV p–p data taking in August 2010.

As shown in figure 3.8, the high multiplicity trigger greatly increases the statistics at high multiplicity. In this plot multiplicity is defined as the number of reconstructed tracks with $p_{\mathrm{T}} > 0.2$ GeV, according to the multiplicity definition used in the analysis and described in more detail in section 4.3.

Figure 3.8 also shows the HM/MB ratio, which is constant (within statistical uncertainty) above 58 tracks. As such, 58 tracks was taken as the threshold above which the high multiplicity trigger was usable.

Each trigger described above was configured to trigger the read out of all of the

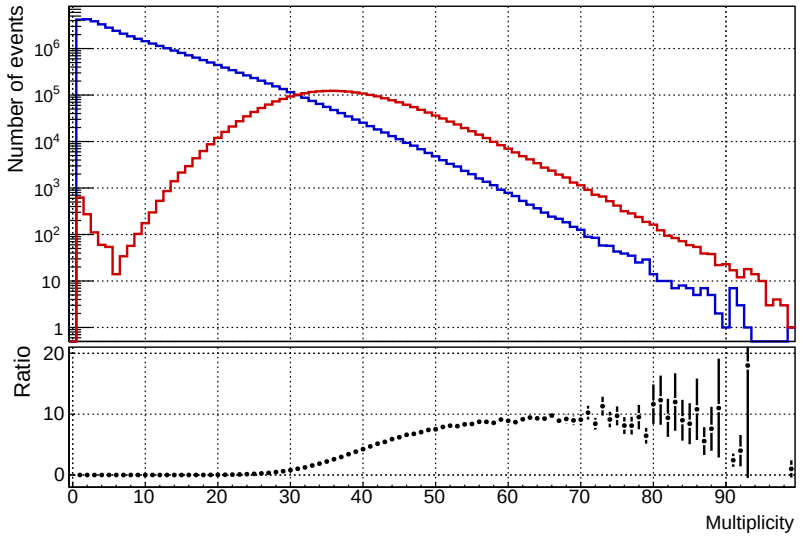

Figure 3.8: Multiplicity spectra of MB (blue) and HM (red) triggered $\sqrt{s} = 7$ TeV p–p data. Below is the HM/MB ratio.

main tracking detectors. Additional triggers, such as a muon trigger, were also in use during the data taking period analysed here. However, as they were not used in this analysis, they are not described in this document.

High multiplicity trigger bias

During the period of data taking in which the high multiplicity trigger was active there were problems with the ITS cooling system, leading to a non-negligible number of non-functioning pixels in the SPD. As described in section 4.1.1, track cuts were optimised to minimise any resultant biasing of the results. However, there was some concern that this would cause a bias in the high multiplicity trigger. Specifically, as the dead pixels were clustered together causing large non-functioning sections, there was a possibility that the trigger would respond differently to events with a clustered track profile (such as jet events) as opposed to those with a more uniformly distributed track profile. This would alter the relative proportions of these event types in the selected event sample.

To determine the extent of this issue, correlation plots were produced within the same high multiplicity bin from both minimum bias and high multiplicity triggered data. These were observed to be compatible within experimental uncertainty, leading to the conclusion that no significant bias existed in the final results.

3.2.7 Data acquisition and offline reconstruction

After an L2a trigger signal is received, the read out data from the detectors is managed by the Data Acquisition (DAQ) system. The Front-End Readout Electronics (FERO) of each detector are connected via optical fibre to Local Data Concentrators (LDCs), each of which receive and process chunks of an event. These chunks are then merged into a full event by one of a farm of Global Data Concentrators (GDCs), after which the raw data are stored for offline reconstruction [83].

The offline reconstruction of events is performed using the AliRoot software, an extension of the ROOT analysis software with ALICE-specific libraries and methods. This is processed on the Grid, a large distributed computing network [83].

The raw output from the tracking detectors consists of signals from detector elements, which are digitised. Sets of digits which are adjacent in space are assumed to originate from the same particle traversing the detector, and are combined into clusters. Space points are then reconstructed in three dimensions, generally positioned according to the centre of gravity of the cluster [93].

Before reconstructing full tracks, the primary vertex is reconstructed. Pairs of space points in the two layers of the SPD which are close in azimuthal and polar angles are joined to form tracklets, from which the primary vertex position is determined.

A first pass track reconstruction is then performed, starting with track seeds from the outermost clusters in the TPC and working inwards whilst assuming that all tracks originated at the primary vertex. This is repeated without the constraint

to the primary vertex, with both sets of tracks stored; the track finding is then continued through it ITS.

After the first pass, a second pass takes place, with the track finding beginning at the inner layer of the ITS and working outwards. The track can then be further refined by a final refitting, again beginning at the outside of the TPC and following the tracks inwards. Reconstruction is also possible using only the TPC or the ITS, producing so-called TPC or ITS standalone tracks. The transverse momentum of detected particles can then be deduced from the curvature of their tracks in the 0.5 T field of the ALICE solenoidal magnet, with the tracks of higher p_{T} particles having a greater radius of curvature.

After reconstruction, the data are stored in the Event Summary Data (ESD) format for future analysis. Typically this analysis is carried out on the Grid using routines written in C++ which utilise AliRoot.

CHAPTER 4

TWO-PARTICLE CORRELATION ANALYSIS

Jet analysis using dihadron angular correlations, mentioned briefly in section 1.4.5, takes a fundamentally different approach to the perhaps more familiar method of event-by-event jet reconstruction. Instead of requiring that individual jets be reconstructed, a statistical approach is taken whereby the distribution of angular separation of tracks is studied for a large sample of events. This technique is particularly useful with heavy ion collisions, where the large multiplicities make it difficult for jet-finder algorithms to distinguish tracks belonging to a jet from background. Such a statistical method is sensitive to a wide variety of jet physics [64, 94].

This chapter describes the usage of two-particle angular correlations for a study of jet shapes and transverse momentum imbalance (quantified by the jet fragmentation transverse momentum j_{T}, and the net partonic transverse momentum k_{T}) in mini-

Table 4.1: Summary of real data used in analysis.

System	$\sqrt{s}$ (TeV)	LHC period	MB events (millions)
p–p	2.76	LHC11a	45
	7	LHC10e	52
Pb–Pb	2.76/nucleon	LHC10h	18

Table 4.2: Summary of Monte-Carlo data used in analysis.

System	$\sqrt{s}$ (TeV)	Generator	MC production	Events (millions)
p–p	2.76	Pythia 6	LHC11e3a_plus	45
	7	Pythia 6	LHC10e20	13
Pb–Pb	2.76/nucleon	HIJING	LHC11a10a_bis	2.8

mum bias proton collisions, the results of which are presented in chapter 5. The use of correlations for a study of the multiplicity dependence of the jet yield in proton and ion collisions is described; the results of this are given in chapter 6. An analysis of the multiplicity dependence of the jet shape was also performed, the results being presented in chapter 7.

The proton multiplicity analyses were performed with a view to attempting to identify possible medium effects in high multiplicity proton collisions, as described in section 1.3.2; the ion analyses were performed for comparison.

4.1 Data sample

This analysis used data from p–p collisions at $\sqrt{s} = 7$ TeV and $\sqrt{s} = 2.76$ TeV, and Pb–Pb collisions at $\sqrt{s_{\mathrm{NN}}} = 2.76$ TeV. The data used, with the LHC periods and number of MB triggered events at each energy, are summarised in table 4.1. The analysis also used simulated Monte-Carlo data, which are detailed in table 4.2.

In the minimum bias proton collision analysis, the use of two beam energies allows the dependence of jet shapes on beam energy to be ascertained. In the multiplicity

analysis, the 2.76 TeV p–p data were used to allow the closest possible comparison with Pb–Pb data, as for this data $\sqrt{s_{\mathrm{pp}}} = \sqrt{s_{\mathrm{NN}}}$. The 7 TeV p–p data were used to allow the furthest possible multiplicity reach, as the high multiplicity trigger was only used during this period. Stronger QGP effects would also be expected to be more apparent in higher energy data. The LHC period given in the table contains a number indicating the year and a letter indicating the run period within that year, a period of data taking lasting roughly a month.

The simulated Monte-Carlo data were central ALICE productions, generated to match the detector response of the corresponding real data periods as closely as possible (the production name not necessarily matching the corresponding run period).

For p–p data, the Pythia 6 event generator was used with the Perugia-0 tune [95, 96]. Pythia is a Monte-Carlo event generator, developed with emphasis on events involving strong interactions. The total p–p collision cross section is divided into elastic, diffractive and inelastic components, with the diffractive physics being described by a pomeron model. Inelastic interactions are simulated with a pQCD model, the divergence of the cross section at low p_{T} being avoided by the introduction of a phenomenological cutoff $p_{\mathrm{Tmin}} \sim 2$ GeV. Pythia also includes a description of multi-parton interactions, whereby several parton–parton interactions can take place within one event. Fragmentation of colour strings is simulated using the Lund string model.

For Pb–Pb data, the HIJING 1.36 generator was used [97], which models QCD processes in a similar manner to Pythia. The simulation is extended to heavy ion collisions with Glauber geometry used to describe multiple nucleon–nucleon interactions In addition, nuclear phenomena such as nuclear shadowing (where the nuclear PDFs are modified with respect to those of free partons) are included. Final state effects, such as the suppression of high p_{T} hadrons in a volume of QGP, can also be introduced.

In both cases, the detector response was simulated using GEANT3.

4.1.1 Track selection

For each event, a set of track selection cuts were applied to eliminate poor-quality tracks. These were optimised to preferentially select primary particles not originating from weak decays or from interactions with detector components, and to maximise momentum resolution. In the period in which $\sqrt{s} = 7$ TeV p–p data were taken, there were a number of non-functioning sections in the ITS due to problems with the cooling system, which caused a non-negligible number of dead pixels in the SPD. To minimise the bias that this would cause to the results, no ITS hits were required. For consistency, the same set of track cuts was used for all events; these are detailed here.

- $|\eta| < 0.8$.
- At least 50 clusters in the TPC.
- χ^2/cluster < 4 in the TPC.
- DCA$_z < 3.2$ cm, DCA$_{xy} < 2.4$ cm where DCA$_{z,xy}$ is the impact parameter of the track in the beam direction and perpendicular to it.
- No kink daughters. Kinks can be produced by, for example, decay of a charged particle leading to a charged and a neutral product, or by interaction with a tracked particle with a detector element. They can also be produced by failures in tracking.

4.2 Pileup

A consequence of the high luminosities reached at the LHC during proton running is a high probability of multiple interactions occurring within one bunch crossing, termed pileup (due to the low luminosities during Pb–Pb collisions at the LHC, pileup for these events is negligible). This is typically quantified within a given run by the average number of interactions per bunch crossing μ; the probability $P(\mu, n)$ for n interactions in one bunch crossing then being determined by a Poisson distribution:

$$P(\mu, n) = \frac{e^{-\mu}\mu^n}{n!}. \tag{4.1}$$

μ is determined on a run-by-run basis from the number of fired CINT1B and CBEAMB triggers. A CBEAMB trigger indicates that both beams were present in the detector (as monitored by beam pickup detectors) and thus that proton interactions could occur, and CINT1B is the minimum bias trigger described in section 3.2.6 which implies that an interaction occurred while both beams were present. The ratio of the number of CINT1B triggers to the number of CBEAMB triggers thus gives the fraction of bunch crossings in which at least one interaction occurred, and hence the probability of at least one interaction occurring in a given bunch crossing. μ can then be determined by solving

$$\frac{\text{CINT1B}}{\text{CBEAMB}} = 1 - P(\mu, 0) \tag{4.2}$$

where CINT1B and CBEAMB indicate the number of those triggers fired and

$$P(\mu, 0) = e^{-\mu}$$

is the probability of no interactions occurring in one bunch crossing.

4.2.1 Estimation of pileup fraction

The fraction of pileup in measured data increases with event multiplicity and so during the period in which the ALICE high multiplicity trigger was in use the LHC was operated with a low-μ configuration at point 2, with the beams intentionally slightly misaligned.

Only the runs with the lowest μ were selected for the high multiplicity p–p analysis. The prevalence of pileup within these runs was estimated with a Monte-Carlo model. This model generated simplified events following the multiplicity spectrum determined from a "pileup-free" run of very low μ, each of which could contain from one to three interactions with proportions according to the μ calculated as described above. As a worst-case scenario, the highest μ of all selected runs was used.

The interaction vertices were distributed with a Gaussian distribution of width taken from the same "pileup-free" run, and the track DCA to the interaction vertex distributed according to a Gaussian determined similarly. Within each event, the highest multiplicity interaction was taken as the primary interaction and the others as pileup.

Different cuts were then applied on the zDCA of each track with respect to the primary vertex (where z indicates the direction parallel with the beam axis), and the degree of included pileup calculated. With the same cut as used in the analysis, $z\text{DCA} < 2$ cm, at the highest multiplicities the pileup fraction estimate was calculated to be 0.085.

To determine the effect of pileup on the final results, the analysis was performed with the zDCA cut reduced to 0.5 cm, reducing the pileup fraction at the highest multiplicities according to the model to 0.059. This had no measurable effect on the results, and so pileup was not deemed to be a significant issue. The zDCA cut was also varied when determining the systematic uncertainties due to the choice of track

cuts.

4.3 Multiplicity definition

For the multiplicity analysis, various multiplicity estimators were considered. Figure 4.1 shows the correlation of four potential multiplicity estimators with the true multiplicity in the region $|\eta| < 0.8$, in a sample of $\sqrt{s} = 2.76$ TeV p–p events simulated in Pythia. The estimators displayed in the figure are the number of reconstructed tracks with $p_{\mathrm{T}} > 0.2$ GeV, the number of reconstructed tracks with $p_{\mathrm{T}} > 0.3$ GeV, the V0 multiplicity and the number of SPD tracklets (a tracklet being a short track reconstructed using only information from the SPD).

It can be seen that the estimators involving the number of reconstructed tracks have a tighter correlation with the true multiplicity. This is largely due to the sensitivity of the detectors to different physics due to their differing acceptance. For example, diffractive events that cause a signal in the V0 due to its forward position can still produce few reconstructable tracks at central rapidity. In real data this effect is worsened by, for example, beam–gas interactions.

It is also preferable to use a relatively low p_{T} cut for the estimator, to minimise the risk of biasing the final results. As such, the multiplicity estimator selected for this analysis was the number of reconstructed tracks with $p_{\mathrm{T}} > 0.2$ GeV.

4.3.1 Defining centrality in heavy ion collisions

When heavy ion nuclei collide ultra-relativistically they appear in the centre of mass frame as Lorentz contracted "pancakes" of thickness $2R/\gamma_{\mathrm{cm}}$ (although there is a limiting thickness of around 1 fm due to Fermi momentum) where R is the nuclear radius (around 10 fm for typical experimental nuclei such as lead or gold)

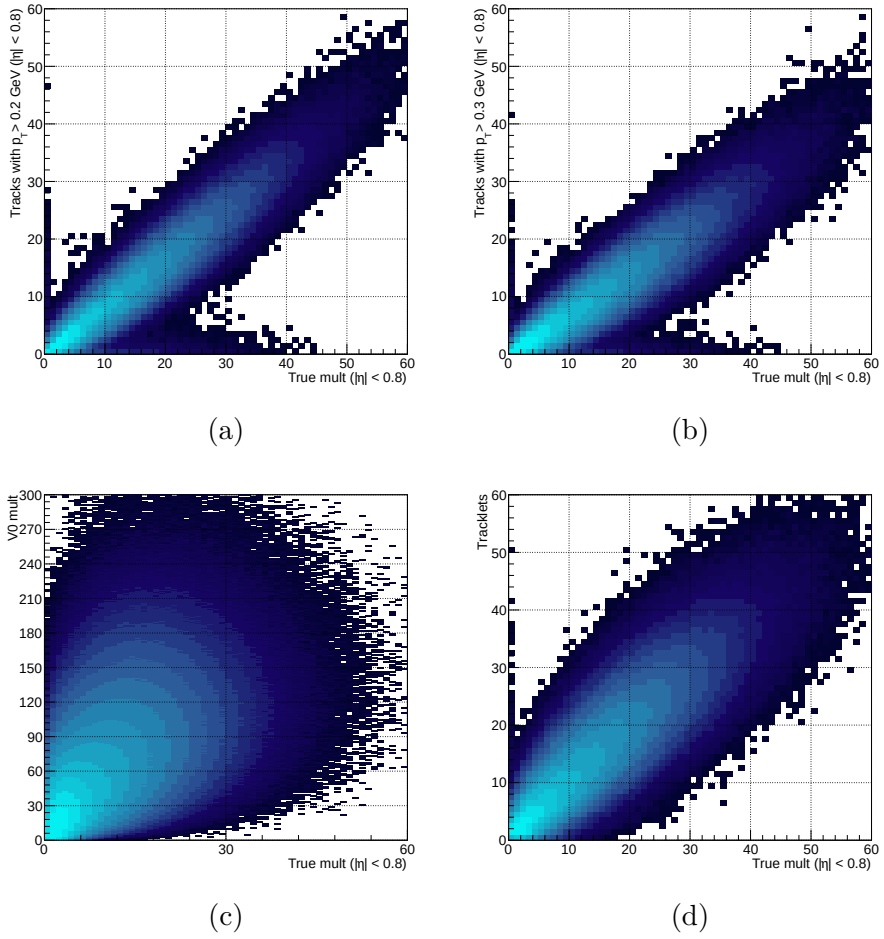

Figure 4.1: Correlation of multiplicity estimators with true multiplicity in the region $|\eta| < 0.8$. Based on a sample of $\sqrt{s} = 2.76$ TeV p–p events simulated in Pythia. A logarithmic scale is used on the z axis. The estimators depicted are (a) number of reconstructed tracks with $p_{\mathrm{T}} > 0.2$ GeV, (b) $p_{\mathrm{T}} > 0.3$ GeV, (c) V0 multiplicity, (d) Number of SPD tracklets.

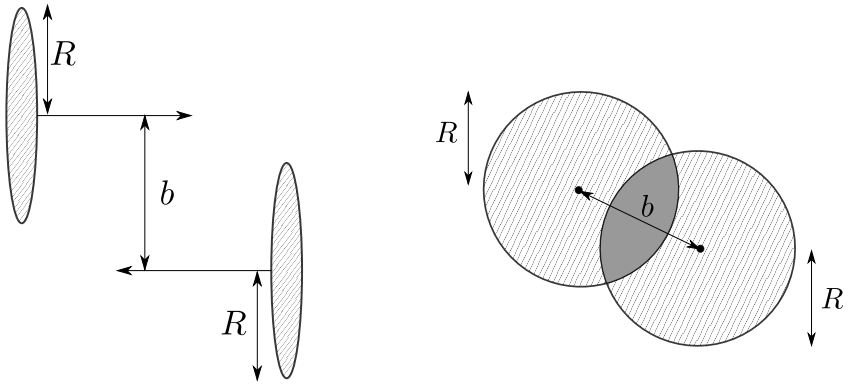

(a) (b)

Figure 4.2: Geometry of the collision of two heavy ions of radius R, with impact parameter b.

and $\gamma_{\mathrm{cm}} = E_{\mathrm{cm}}/2m_{\mathrm{N}}$ is the relativistic Lorentz factor, with m_{N} being the nucleon mass [10].

As the colliding nuclei are, in the transverse direction at least, relatively large, it is likely that the collision is not in fact head on but instead occurs with a degree of overlap. The transverse separation of the nucleus centres is termed the impact parameter, b. This is depicted in figure 4.2a, with the overlapping region in the transverse plane shown in figure 4.2b.

The degree of overlap is typically quantified not by the impact parameter but by the collision centrality. This is defined from 0–100% of cross section, where 0% is a perfectly head on collision with $b = 0$, and 100% is an extreme peripheral collision with $b = 2R$. Typically in the ultra-peripheral region electromagnetic effects dominate, and so centralities more peripheral than 90% are often excluded from analyses. Larger, denser volumes of QGP would be expected in more central collisions.

4.3.2 Determination of centrality

The centrality is not directly measurable, but it is strongly correlated with the observed particle multiplicity. As such, multiplicity is commonly used as a centrality estimator, with the hadronic cross section as a function of multiplicity being divided into percentiles [82].

While the standard ALICE centrality estimator uses the V0 multiplicity, in this analysis it was decided that the same multiplicity estimator would be used for both p–p and Pb–Pb data, to enable more direct comparison between the two systems. This estimator is described at the beginning of section 4.3.

The multiplicity distribution according to this estimator is fit using a Monte-Carlo model, with a Glauber model to describe the collision geometry and a negative binomial distribution to describe the particle production. This follows the basic technique used by the standard ALICE centrality estimator [82]; the model is described in appendix C. The multiplicity distribution was fit only in the region above 25 tracks to minimise the contamination from electromagnetic interactions, which comprise a non-negligible contribution to the total cross section in the most peripheral collisions.

The distribution obtained from the model and divided into centrality bins is shown, together with the multiplicity distribution from the data, in figure 4.3. It can be seen that the model matches the data well. Figure 4.4 shows the correlation between centrality according to this estimator and centrality according to the standard ALICE centrality estimator, using V0 multiplicity.

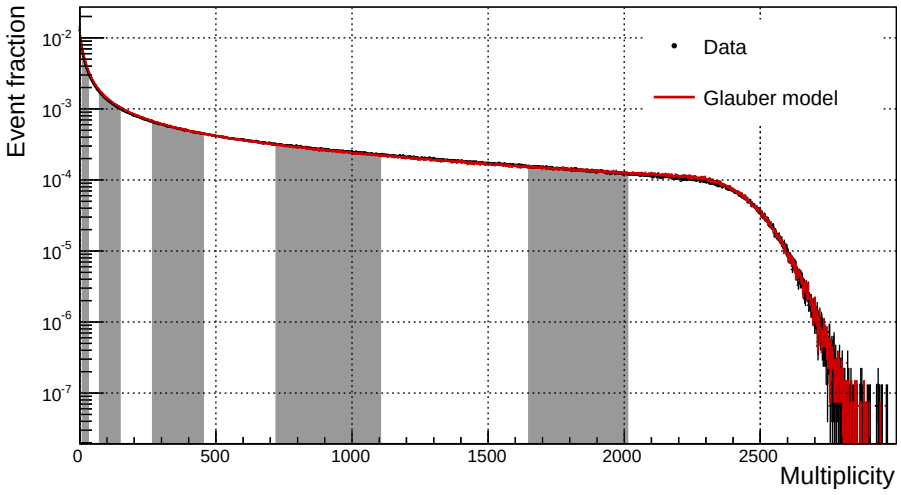

Figure 4.3: Multiplicity spectrum from data and from the Glauber model, with the Glauber distribution divided into centrality bins (alternately shaded). The most central two are 0–5% and 5–10%, and the remaining are in 10% increments.

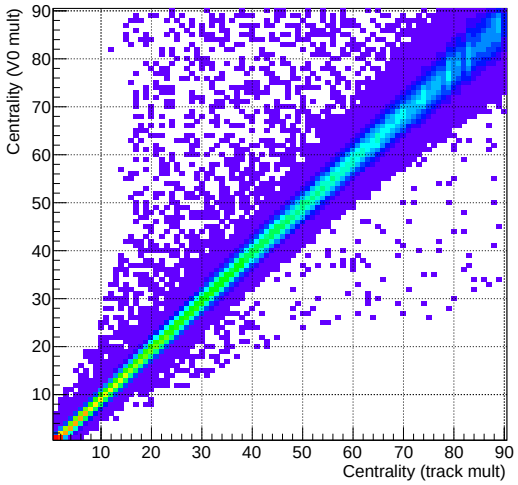

Figure 4.4: Correlation of centrality according to reconstructed track multiplicity with centrality according to V0 multiplicity.

4.4 Correlation function construction

In each event, high p_{T} particles (defined as having p_{T} within a given range) are identified and termed "trigger" particles. For each of these, pairs are formed with "associated" particles, defined as having p_{T} less than that of the trigger but still relatively high (defined as being within a different, but still relatively high, range). Dihadron azimuthal correlation functions measure the distribution of angular difference $\Delta\phi = \phi_{\mathrm{t}} - \phi_{\mathrm{a}}$ between these pairs; in general in this analysis, subscripts "t" and "a" refer to the trigger and associated particles, respectively. The allowed p_{T} ranges of the trigger and associated particles, p_{Tt} and p_{Ta}, are selected to be high enough that soft effects (such as flow) do not form a significant contribution but low enough that an acceptably large number of pairs are analysed.

The normalised correlation function can be constructed as the ratio of real to mixed distributions

$$C(\Delta\phi) = \frac{N_{\mathrm{mix}}}{N_{\mathrm{trigg}}} \cdot \frac{dN_{\mathrm{uncorr}}/d\Delta\phi}{dN_{\mathrm{mix}}/d\Delta\phi} \tag{4.3}$$

where N_{trigg} is the number of triggers in the real distribution, N_{mix} is the number in the mixed distribution and $dN_{\mathrm{uncorr}}/d\Delta\phi$ and $dN_{\mathrm{mix}}/d\Delta\phi$ are the real and mixed distributions. The real distribution is the $\Delta\phi$ distribution within each event, whereas the mixed distribution is constructed using the trigger particles of one event and the associated particles of another event. As pairs in the mixed distribution are uncorrelated by construction, the use of the mixed distribution in this manner corrects for the pair detection efficiency of the detector.

If the mixed distribution is suitably flat, this normalisation is equivalent to normalising by a constant, and so in this case the following distribution could be used:

$$\frac{1}{N_{\mathrm{trigg}}} \frac{dN_{\mathrm{uncorr}}}{d\Delta\phi}. \tag{4.4}$$

The mixed distribution is equivalent to the convolution of the ϕ_{t} distribution with the

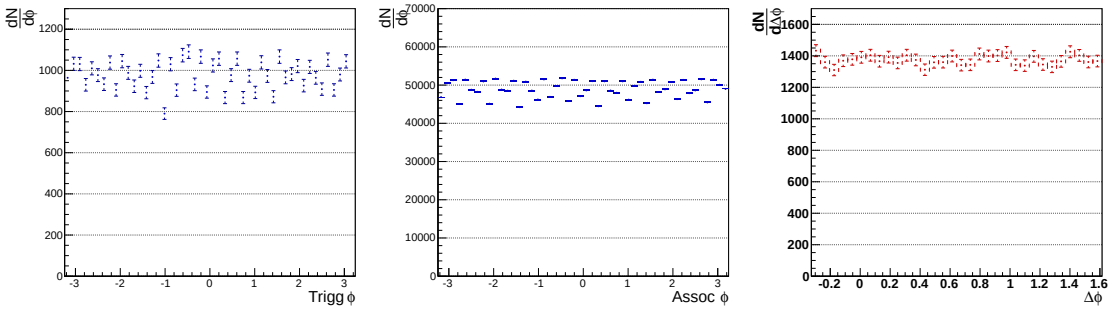

(a) (b) (c)

Figure 4.5: Convolution of ϕ distributions. (a) ϕ_{t}, for $8 < p_{\mathrm{Tt}} < 15$ GeV. (b) ϕ_{a}, for $3 < p_{\mathrm{Ta}} < 8$ GeV. (c) Monte-Carlo convolution of (a) with (b).

ϕ_{a} distribution. Figure 4.5 shows ϕ_{t} and ϕ_{a} distributions for $\sqrt{s} = 7$ TeV p–p data next to the convolution of one with the other (performed using a simple Monte-Carlo process). It can be seen that the ϕ distributions are noticeably non-uniform, mostly as a result of the segmented structure of the TPC. Despite this, the convolution process leads to a very flat pair acceptance. As such, in this analysis the raw $\Delta\phi$ distributions were normalised by a constant N_{trigg} and no mixed distributions were used. The "uncorr" suffix is omitted in the remainder of this document, ie.

$$\frac{1}{N_{\mathrm{trigg}}}\frac{dN}{d\Delta\phi} \equiv \frac{1}{N_{\mathrm{trigg}}}\frac{dN_{\mathrm{uncorr}}}{d\Delta\phi}. \tag{4.5}$$

Normalised $\Delta\phi$ correlation plots generally have a characteristic shape of two peaks, at $\Delta\phi \approx 0$ and $\Delta\phi \approx \pi$, corresponding to pairs of azimuthally opposite jets. These sit on top of a constant pedestal from the uncorrelated background. Examples of uncorrected and normalised $\Delta\phi$ distributions illustrating this shape, from both p–p and Pb–Pb collisions, are shown in figures 4.6 and 4.7. In general in this document $\Delta\phi$ distributions are presented in units of π such that, for example, $\Delta\phi = 1$ implies that the two particles are perfectly back-to-back.

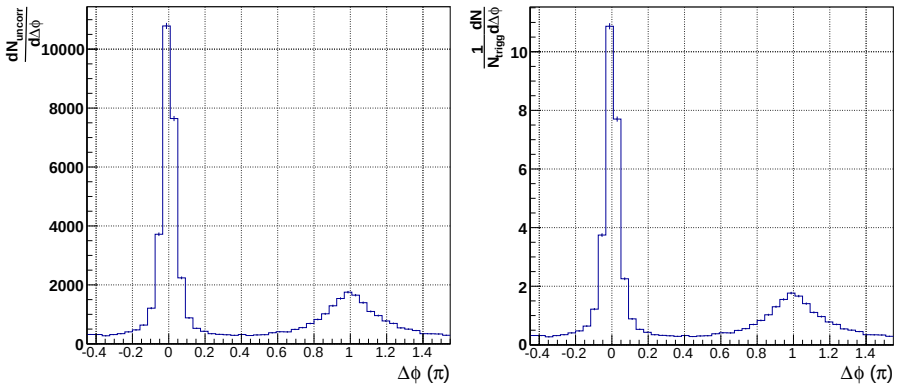

(a) (b)

Figure 4.6: Example raw (a) and per-trigger (b) correlation functions, from $\sqrt{s} = 7$ TeV p–p data with $8 < p_{\mathrm{Tt}} < 15$ GeV and $3 < p_{\mathrm{Ta}} < 8$ GeV.

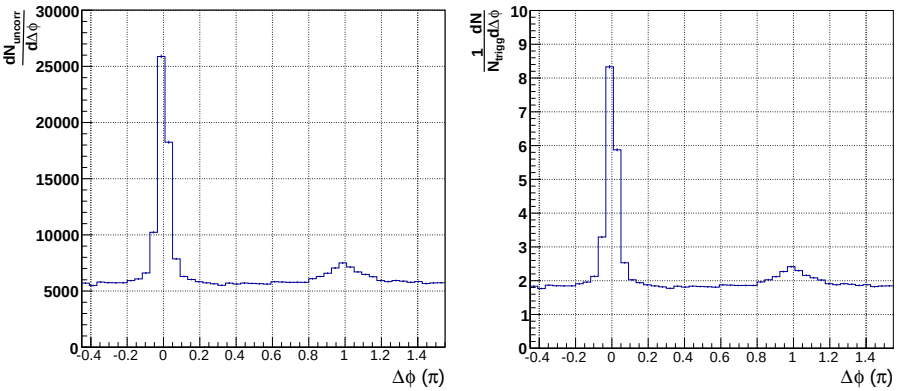

(a) (b)

Figure 4.7: Example raw (a) and per-trigger (b) correlation functions, from 0–5% central $\sqrt{s_{\mathrm{NN}}} = 2.76$ TeV Pb–Pb data with $8 < p_{\mathrm{Tt}} < 15$ GeV and $3 < p_{\mathrm{Ta}} < 8$ GeV.

4.5 Corrections

When analysing correlation data it is important to consider the effects of efficiency and contamination. These can be divided into single particle and pair corrections, with the single particle correction being applied to all trigger and associated particles separately, and the pair correction being applied to all pairs. The required corrections are determined from a comparison of reconstructed and generator-level simulated Monte-Carlo data, the data being described in section 4.1 and summarised

in table 4.2.

4.5.1 Single particle corrections

In general it is important to correct for tracking inefficiencies and fake tracks, where tracking inefficiency is caused by tracks not being reconstructed and a fake track is one which was wrongly reconstructed where in fact no particle from the initial interaction traversed the detector. Tracking efficiency is defined as

$$\varepsilon = \frac{N_{\mathrm{rec}}^{\mathrm{prim}}}{N_{\mathrm{gen}}^{\mathrm{prim}}} \tag{4.6}$$

where $N_{\mathrm{rec}}^{\mathrm{prim}}$ and $N_{\mathrm{gen}}^{\mathrm{prim}}$ are the number of reconstructed and generated primaries, respectively, a primary being defined as a particle produced in the initial collision and not resulting from a later weak decay or from an interaction with the detector material. Contamination is defined as

$$f = \frac{N_{\mathrm{fake}}}{N_{\mathrm{rec}}} \tag{4.7}$$

where N_{fake} is the number of reconstructed tracks that do not correspond to a primary particle and $N_{\mathrm{rec}} = N_{\mathrm{rec}}^{\mathrm{prim}} + N_{\mathrm{fake}}$ is the total number of reconstructed tracks. The overall correction for efficiency and contamination c is then defined as

$$c^{-1} = \frac{N_{\mathrm{fake}} + N_{\mathrm{rec}}^{\mathrm{prim}}}{N_{\mathrm{gen}}^{\mathrm{prim}}} = \frac{N_{\mathrm{rec}}}{N_{\mathrm{gen}}^{\mathrm{prim}}}. \tag{4.8}$$

This is shown in figure 4.8 for each Monte-Carlo production, as a function of p_{T}, for three multiplicity bins in p–p and three centrality bins in Pb–Pb. It can be seen that, while there is some dependence on multiplicity/centrality, within a given multiplicity bin the correction appears to be flat within statistical uncertainty above $p_{\mathrm{T}} \approx 3$ GeV.

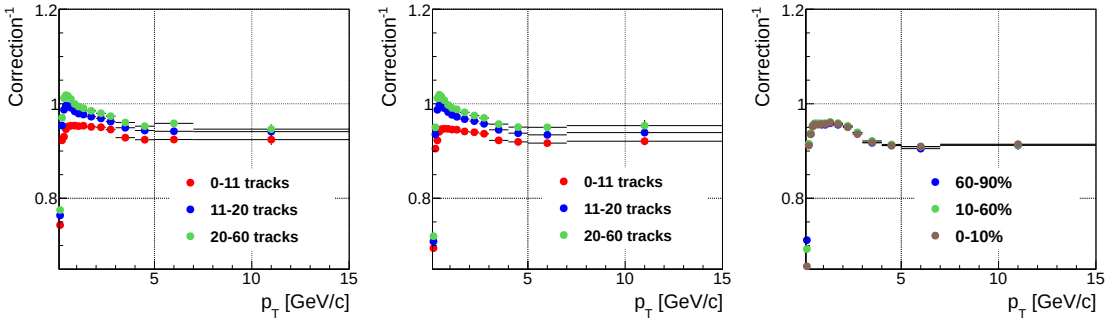

(a) (b) (c)

Figure 4.8: Single particle correction as a function of p_{T}. (a) $\sqrt{s} = 7$ TeV p–p, (b) $\sqrt{s} = 2.76$ TeV p–p, (c) $\sqrt{s_{\mathrm{NN}}} = 2.76$ TeV Pb–Pb.

Table 4.3: Histogram filling points for pair correction determination.

Stage	Track selection	Event selection	Detector effect
0	All triggered events	Primary MC	
1	Reconstructed vertex	Primary MC	Vertex reconstruction
2		Primary MC if reconstructed	Tracking efficiency
3		Primary MC if reconstructed + secondaries + fakes	Contamination
4		Reconstructed tracks	Tracking resolution

4.5.2 Pair corrections

As well as single particle corrections, a combined pair correction must be considered. An example of a pair effect is the possibility that two particles with $\Delta\phi \approx 0$ are incorrectly reconstructed as a single track. To demonstrate these corrections, separate $\Delta\phi$ distributions are filled at various stages of the analysis. Table 4.3 summarises these stages.

The ratio of the correlation plot at each stage to that of the previous stage was then taken; these ratios are shown in figure 4.9. It can be seen that the significant effects are those of tracking efficiency and contamination, and that the necessary corrections are, within statistical uncertainty, constant in $\Delta\phi$. While the statistical uncertainties for the two p–p collision energies in this study are relatively large due

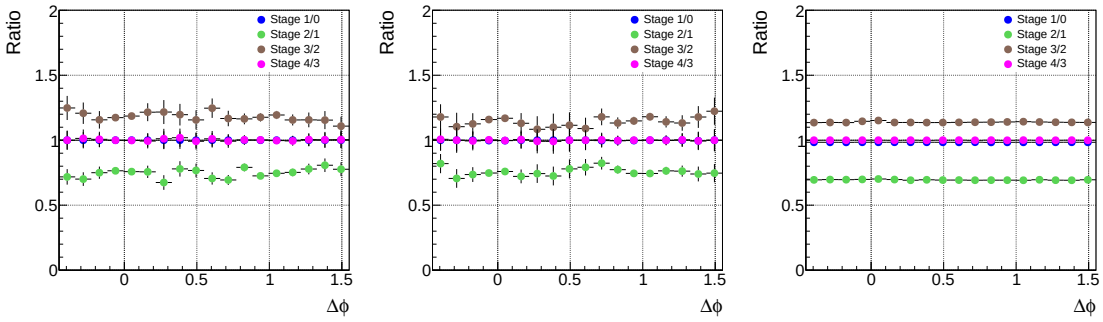

(a) (b) (c)

Figure 4.9: Pair correction as a function of $\Delta\phi$. Stages are defined in table 4.3. $\Delta\phi$ is shown in units of π. (a) $\sqrt{s} = 7$ TeV p–p, (b) $\sqrt{s} = 2.76$ TeV p–p, (c) $\sqrt{s_{\mathrm{NN}}} = 2.76$ TeV Pb–Pb.

to the low Monte-Carlo statistics available, the uncertainties for Pb–Pb collisions are small and the resulting ratios are very flat; generally pair effects are expected to be less significant in p–p collisions than in Pb–Pb. The plots in this figure are not binned in multiplicity or centrality as no significant distinction was observed between the bins.

4.5.3 Overall correction

As can be seen in sections 4.5.1 and 4.5.2, the single particle corrections are flat within statistical uncertainty for particles of p_{T} greater than 3 GeV, and the pair corrections are flat in $\Delta\phi$ within statistical uncertainty. As will be described in sections 4.6 and 4.7, the final values extracted from the correlation functions and compared between different systems are either the ratio of away to nearside yields, or are dependent on the widths of the near or awayside peaks. As such, the values are unchanged by a constant scaling of the correlation functions. This has the consequence that, provided all considered particles have $p_{\mathrm{T}} > 3$ GeV, the results are independent of both the single particle and pair corrections. Because of this, no correction was actually applied in the final analysis. Where absolute values of quantities were compared, for example between data and Monte-Carlo (MC), this

was done within the same system such that correction was not required.

4.6 Comparison of jet shapes

Dihadron correlations can be used to study the typical jet shape and momentum imbalance. As described in section 2.1, the relative p_{T} of a jet hadron with respect to the parent parton is defined as the jet fragmentation transverse momentum j_{T}. The typical jet width is thus characterised by the RMS of this, $\sqrt{\langle j_{\mathrm{T}}^2 \rangle}$.

In the same section, the net partonic transverse momentum k_{T} is also introduced. This quantifies the degree of p_{T} imbalance between the two jets. Both j_{T} and k_{T} can be extracted from $\Delta\phi$ correlation functions, as described in this section.

4.6.1 Extraction of j_{T}

The typical jet width is directly related to the width of the nearside peak of a dihadron correlation plot (it can be seen that $\sqrt{\langle j_{\mathrm{T}}^2 \rangle} = 0$ would cause the nearside peak to be a delta function), and can be extracted from a fit of this peak. The normalised correlation functions were fitted to the function

$$\frac{1}{N_{\mathrm{trigg}}} \frac{dN}{d\Delta\phi} = c_0 + g_{\mathrm{N1}}(\Delta\phi) + g_{\mathrm{N2}}(\Delta\phi) + g_{\mathrm{A}}(\Delta\phi) \tag{4.9}$$

where c_0 is a constant and $g_{\mathrm{N1,N2,A}}(\Delta\phi)$ are two Gaussians corresponding to the near-side peak and one to the awayside peak, with their means fixed at $\mu_{\mathrm{N1}} = \mu_{\mathrm{N2}} = 0$ and $\mu_{\mathrm{A}} = \pi$. Thus seven free parameters exist to be determined in the fit: the constant background factor c_0, the Gaussian widths σ_{N1}, σ_{N2} and σ_{A}, and the Gaussian areas c_1, c_2 and c_3. Only the peak widths $\sigma_{\mathrm{N,A}}$ were actually required for the analysis.

The nearside peak width was then taken to be

$$\sigma_{\mathrm{N}} = \sqrt{\frac{c_1}{c_1 + c_2}\sigma_{\mathrm{N1}}^2 + \frac{c_2}{c_1 + c_2}\sigma_{\mathrm{N2}}^2} \tag{4.10}$$

and the awayside peak width as the width of the awayside Gaussian.

For two particles from the same jet with $p_{\mathrm{T}} = p_{\mathrm{Tt}}, p_{\mathrm{Ta}}$, the nearside peak width can be related to j_{T} by

$$\sigma_{\mathrm{N}}^2 = \langle \Delta\phi_{\mathrm{N}}^2 \rangle = \left\langle \left(\frac{j_{\mathrm{Ty}}}{p_{\mathrm{Ta}}}\right)^2 + \left(\frac{j_{\mathrm{Ty}}}{p_{\mathrm{Tt}}}\right)^2 \right\rangle \tag{4.11}$$

assuming $\langle j_{\mathrm{Ty}}^2 \rangle \ll p_{\mathrm{Tt}}^2$ and p_{Ta}^2 [66] and thus

$$\sqrt{\langle j_{\mathrm{T}}^2 \rangle} = \sqrt{2\langle j_{\mathrm{Ty}}^2 \rangle} \simeq \sqrt{2} \left\langle \frac{p_{\mathrm{Tt}}^2 + p_{\mathrm{Ta}}^2}{p_{\mathrm{Tt}}^2 p_{\mathrm{Ta}}^2} \right\rangle^{-\frac{1}{2}} \cdot \sigma_{\mathrm{N}}. \tag{4.12}$$

4.6.2 Geometry of k_{T}

Diagrams illustrating a simplified version of the fragmentation of a parton pair in the plane perpendicular to the beam are presented in figure 4.10 with some relevant quantities labelled. Figure 4.10a shows two scattered partons with transverse momenta $\hat{p}_{\mathrm{T}}$ pointing in opposite directions in the parton–parton centre of mass frame.

The partons are shown in the lab frame in figure 4.10b with unequal p_{T} of $\hat{p}_{\mathrm{Tt}}$ and $\hat{p}_{\mathrm{Ta}}$. The imbalance of these momenta is quantified by $\hat{x}_{\mathrm{h}} \equiv \langle \hat{p}_{\mathrm{Ta}} \rangle / \langle \hat{p}_{\mathrm{Tt}} \rangle$. The net parton pair transverse momentum $\hat{p}_{\mathrm{T,pair}}$ corresponds to the vector sum of the k_{T} of each parton. The partons fragment, with jet fragments corresponding to each jet having transverse momenta of p_{Tt} and p_{Ta}. As j_{T} has been neglected, the jets have no width.

The component of k_{T} perpendicular to $\hat{p}_{\mathrm{Tt}}$, termed k_{Ty}, has been labelled. It is as-

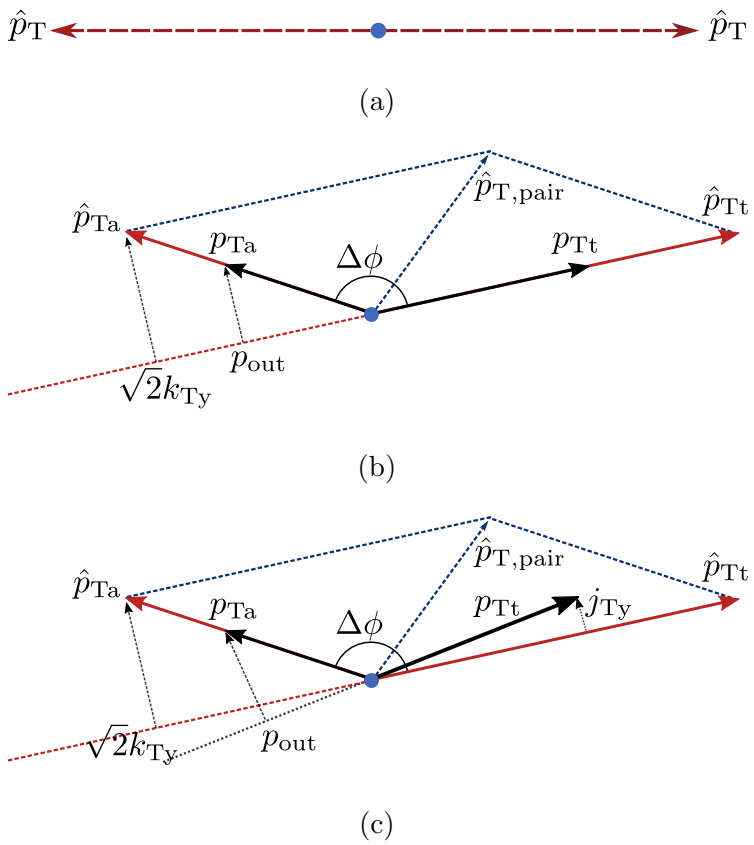

Figure 4.10: The geometry of fragmentation in the plane perpendicular to the beam. Some quantities relevant to this analysis are labelled.
(a) Back-to-back partons in the parton–parton centre of mass frame.
(b) The partons appear in the lab frame with unequal transverse momenta of $\hat{p}_{\mathrm{Tt}}$ and $\hat{p}_{\mathrm{Ta}}$, at an angle $\Delta\phi$. The partons fragment into hadrons of transverse momenta p_{Tt} and p_{Ta}, with j_{T} neglected here.
(c) As (b), with the addition of non-zero j_{T} for the trigger-side jet.

sumed that k_{Ty} and the component k_{Tx} parallel to $\hat{p}_{\mathrm{Tt}}$ follow equal Gaussian distributions. An important feature of k_{T} is that while $\langle k_{\mathrm{Tx}} \rangle = \langle k_{\mathrm{Ty}} \rangle = 0$, $\langle k_{\mathrm{T}} \rangle \neq 0$ as k_{T} is a radius vector, related to the components by the purely geometrical relationship $\sqrt{\langle k_{\mathrm{T}}^2 \rangle} = \sqrt{2\langle k_{\mathrm{Tx}}^2 \rangle} = \sqrt{2\langle k_{\mathrm{Ty}}^2 \rangle}$. These components lead to different experimental effects; specifically k_{Tx} causes the p_{T} imbalance of the outgoing parton pair (in other words causes $\hat{x}_{\mathrm{h}} \neq 1$) and k_{Ty} causes an acoplanarity (the p_{T} of one jet lies out of the plane defined by the p_{T} of the other jet and the beam axis [66]). The component of p_{Ta} perpendicular to p_{Tt}, a quantity somewhat analogous to k_{T} but defined in terms of final state hadrons rather than partons, is labelled p_{out}.

Actual jets have width, as described in section 2.1 and depicted in figure 2.3. Figure 4.10c displays exactly the same geometry as that in figure 4.10b but with the inclusion of non-zero j_{T} for the trigger ($\hat{p}_{\mathrm{Tt}}$ side) jet. This is essentially the combination of figures 4.10b and 2.3, and it can be seen that this confuses the geometry and makes it distinctly less trivial. In particular, p_{out} and k_{Ty} are no longer collinear and $\Delta\phi_{\mathrm{partons}} \neq \Delta\phi_{\mathrm{hadrons}}$.

4.6.3 Extraction of k_{T}

The determination of k_{T} required both the j_{T} results from section 4.6.1 and also the extraction of p_{out} from the data. While it would be possible to use the geometrical relationship $p_{\mathrm{out}} = p_{\mathrm{Ta}} \sin \Delta\phi$ on a pair-by-pair basis, this would not take into account the uncorrelated background. Instead, p_{out} was calculated [67] as

$$\sqrt{\langle p_{\mathrm{out}}^2 \rangle} \sim \langle p_{\mathrm{Ta}} \rangle \sin \sigma_{\mathrm{A}}. \tag{4.13}$$

The third quantity required from the data for the determination of k_{T} was the ratio

of p_{Ta} to p_{Tt}, termed x_{h} by analogy to the partonic $\hat{x}_{\mathrm{h}}$ introduced in section 4.6.2:

$$x_{\mathrm{h}} \equiv \frac{p_{\mathrm{Ta}}}{p_{\mathrm{Tt}}}. \tag{4.14}$$

These three quantities were then combined in the equation for k_{T} [66]

$$\frac{\langle z_{\mathrm{t}} \rangle \sqrt{\langle k_{\mathrm{T}}^2 \rangle}}{\langle \hat{x}_{\mathrm{h}} \rangle} = \frac{1}{\langle x_{\mathrm{h}} \rangle} \sqrt{\langle p_{\mathrm{out}}^2 \rangle - \langle j_{\mathrm{Tay}}^2 \rangle - \langle x_{\mathrm{h}}^2 \rangle \langle j_{\mathrm{Ty}}^2 \rangle}$$

where $\hat{x}_{\mathrm{h}} \equiv \hat{p}_{\mathrm{Ta}}/\hat{p}_{\mathrm{Tt}}$ and $z_{\mathrm{t}} \equiv p_{\mathrm{Tt}}/\hat{p}_{\mathrm{Tt}}$. Assuming no difference between j_{Tt} and j_{Ta}, this becomes

$$\frac{\langle z_{\mathrm{t}}(k_{\mathrm{T}}, x_{\mathrm{h}}) \rangle \sqrt{\langle k_{\mathrm{T}}^2 \rangle}}{\langle \hat{x}_{\mathrm{h}}(k_{\mathrm{T}}, x_{\mathrm{h}}) \rangle} = \frac{1}{\langle x_{\mathrm{h}} \rangle} \sqrt{\langle p_{\mathrm{out}}^2 \rangle - \langle j_{\mathrm{Ty}}^2 \rangle (1 + \langle x_{\mathrm{h}}^2 \rangle)} \tag{4.15}$$

where z_{t} and $\hat{x}_{\mathrm{h}}$ have been explicitly labelled as functions of k_{T} and x_{h}, and all quantities calculated from the data are collected on the right hand side. Solving for k_{T} is non-trivial, except in the limit that z_{t} and $\hat{x}_{\mathrm{h}}$ tend to 1, which corresponds to low $\sqrt{s}$; indeed at ISR energies $\langle z_{\mathrm{t}} \rangle \approx 0.85$ which enabled this approach to be taken [67].

At LHC energies values of the order of $z_{\mathrm{t}} \sim 0.35$ are expected and thus the aforementioned approximation is not valid; as such an iterative method utilising a Monte-Carlo model was used to solve for k_{T}. This model generates pairs of "partons" to which k_{T} values are applied, the values being drawn from a two-dimensional Gaussian distribution. An output $\sqrt{\langle k_{\mathrm{T}}^2 \rangle}$ value is then calculated according to equation 4.15, and the process repeated with this defining the width of the aforementioned Gaussian. This is then continued iteratively until the $\sqrt{\langle k_{\mathrm{T}}^2 \rangle}$ value converges. A more detailed description of the model is given in appendix B.

4.7 Calculation and comparison of yields

To calculate the yield of charged particles associated with a trigger particle from the correlation functions, it is necessary to subtract the uncorrelated background. This can either be extracted from a fit of the correlation function, or by using the so-called Zero Yield at Minimum (ZYAM) method, where it is assumed that between the jet peaks is a region of zero jet yield. This region is defined as the lowest-yield region of a given width in $\Delta\phi$, the width being selected to be small enough to ensure that the boundaries are sufficiently far from the peaks; the mean yield in this region is then taken as the background. For the yield calculation component of this analysis the ZYAM method was used; the fitting method was used in the determination of the systematic uncertainty. The process is illustrated in figure 4.11.

The integrals of the background-subtracted near and awayside peaks then correspond to the (uncorrected) near and awayside per-trigger yields, respectively. For the remainder of this document, "yield" will refer specifically to this per-trigger yield of charged particles associated with a trigger particle, unless otherwise specified.

An informative way of comparing yields across different systems is the taking of the ratio of awayside to nearside yield. This is sensitive to processes that modify the near and awayside yields differently; for example it would be expected that jet quenching would cause this ratio to fall in Pb–Pb collisions of increasing centrality, or possibly in p–p collisions of high multiplicity.

The process of taking ratios has the convenient side-effect, as mentioned in section 4.5.3, that the single particle and pair efficiencies cancel if they are constant in p_{T} and $\Delta\phi$, respectively. This method also allows the same quantity to be constructed for both Pb–Pb and p–p data.

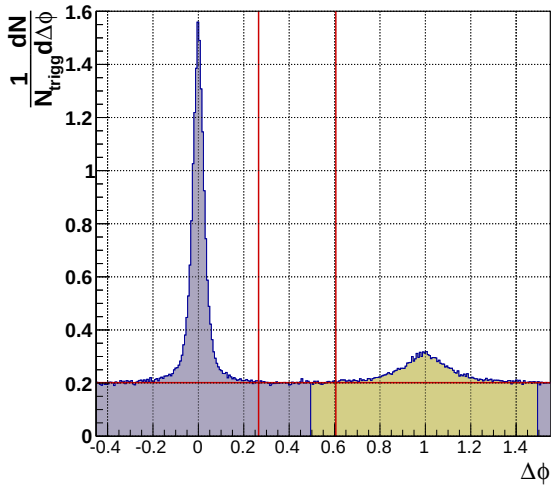

Figure 4.11: Normalised $\Delta\phi$ correlation plot illustrating the ZYAM process. The vertical red lines enclose the lowest-yield region of a given width in $\Delta\phi$, with the background taken to be the mean yield in this region and displayed as the horizontal red line. The near and awayside yields, prior to background subtraction, are shaded in blue and beige, respectively.

CHAPTER 5

MINIMUM BIAS PROTON STUDY RESULTS

This chapter presents the results of the study of jet shapes and transverse momentum imbalance, quantified by j_{T} and k_{T}, respectively, in minimum bias (MB) proton collisions. The study utilised data from $\sqrt{s} = 7$ TeV and $\sqrt{s} = 2.76$ TeV p–p collisions as described in section 4.1.

Results are presented for a range of trigger and associated p_{T} bins; the binning

Table 5.1: p_{T} binning for MB p–p study. All ranges are given in GeV. All combinations of $p_{\mathrm{Tt}}/p_{\mathrm{Ta}}$ bins were used, with the exception of those for which $p_{\mathrm{Ta}} > p_{\mathrm{Tt}}$.

	1	2	3	4	5	6
p_{Tt}	3–5	5–6	6–8	8–11	11–16	16–25
p_{Ta}	3–4	4–6	6–8			

scheme is outlined in table 5.1. All combinations of p_{Tt} and p_{Ta} bins were used, with the exception of those for which $p_{\mathrm{Ta}} > p_{\mathrm{Tt}}$. Combined statistical and systematic uncertainties are shown on the plots as brackets around the statistical error bars; the mechanism by which these were calculated is described in section 5.4.

5.1 Correlation function results

Correlation functions for each $p_{\mathrm{Tt,a}}$ bin were produced following the prescription in section 4.4, and fit to the function given in equation 4.9 of two nearside Gaussians, an awayside Gaussian and a constant for the uncorrelated background. These are shown for three $p_{\mathrm{Tt,a}}$ bins for each collision energy in figure 5.1. The separate contributions of the three Gaussians, along with the sum of these plus the constant background, are shown for one sample bin in figure 5.2.

The peak widths $\sigma_{\mathrm{N,A}}$ extracted from the fits are shown in figure 5.3, where σ_{N} is the combination of the two nearside Gaussian standard deviations as defined in equation 4.10. The widths are presented as functions of p_{Tt} within given p_{Ta} bins.

The nearside width is observed to decrease with increasing p_{Tt}, as expected due to the tendency of higher p_{T} triggers to carry a higher fraction of the momentum of the parent parton, and thus to lie closer to the jet axis. Likewise, a dependence is observed on p_{Ta}, for similar reasons. The combined effects of j_{T} and k_{T} complicate the interpretation of the awayside width, but a similar dependence on p_{Tt} and p_{Ta} is observed. These observations are qualitatively consistent with measurements at RHIC [66].

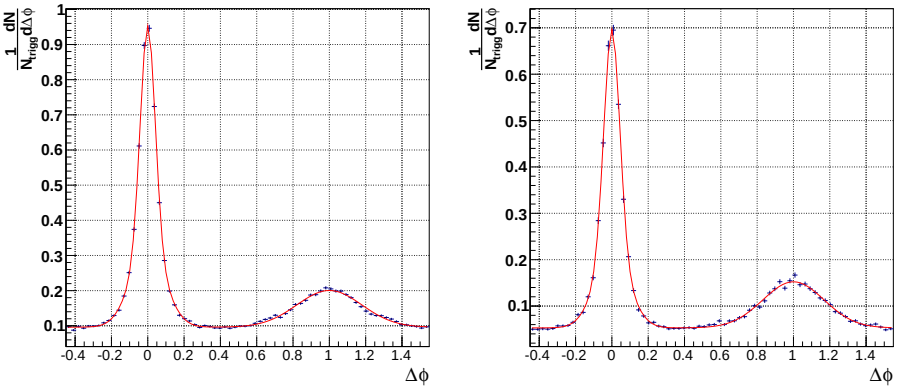

(a) $4 < p_{\mathrm{Tt}} < 5$ GeV, $3 < p_{\mathrm{Ta}} < 4$ GeV

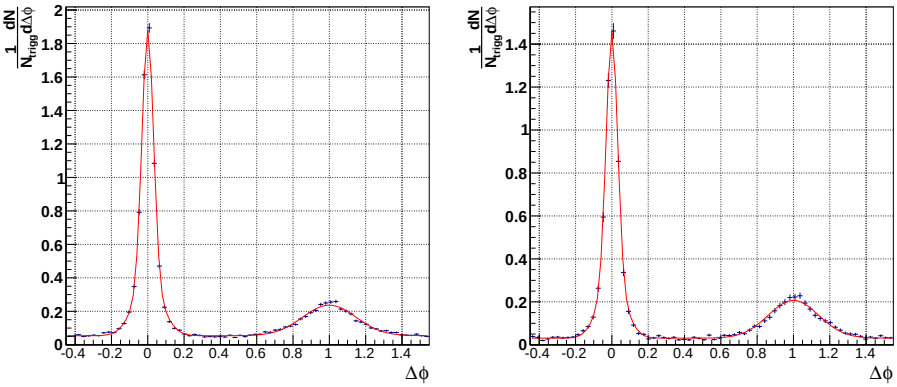

(b) $6 < p_{\mathrm{Tt}} < 8$ GeV, $4 < p_{\mathrm{Ta}} < 6$ GeV

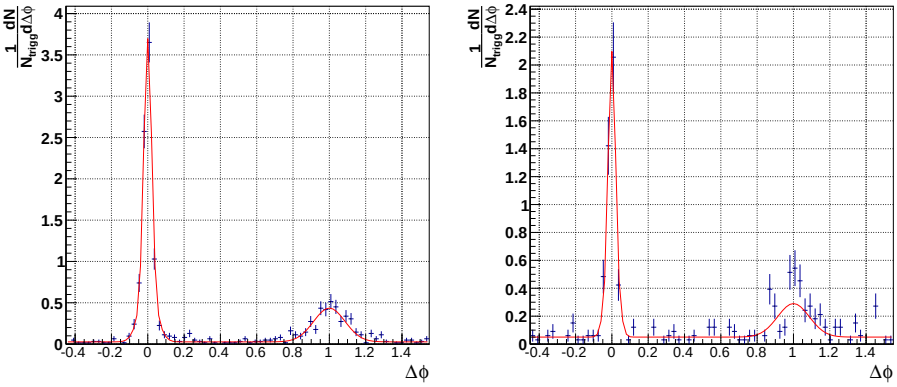

(c) $16 < p_{\mathrm{Tt}} < 25$ GeV, $6 < p_{\mathrm{Ta}} < 8$ GeV

Figure 5.1: Normalised correlation plots for minimum bias p–p data at $\sqrt{s} = 7$ TeV (left side) and $\sqrt{s} = 2.76$ TeV (right side), for three $p_{\mathrm{Tt,a}}$ bins, fit to two nearside Gaussians + awayside Gaussian + constant.

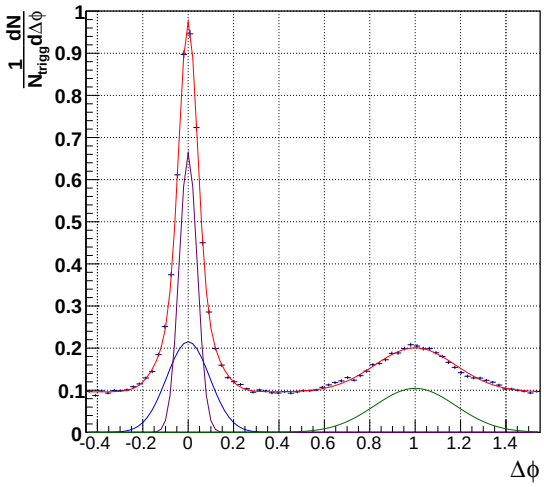

Figure 5.2: Normalised correlation plot from minimum bias p–p data at $\sqrt{s} = 7$ TeV, with $4 < p_{\mathrm{Tt}} < 5$ GeV and $3 < p_{\mathrm{Ta}} < 4$ GeV. The separate near and awayside Gaussians are shown, along with the combination of these plus the constant background.

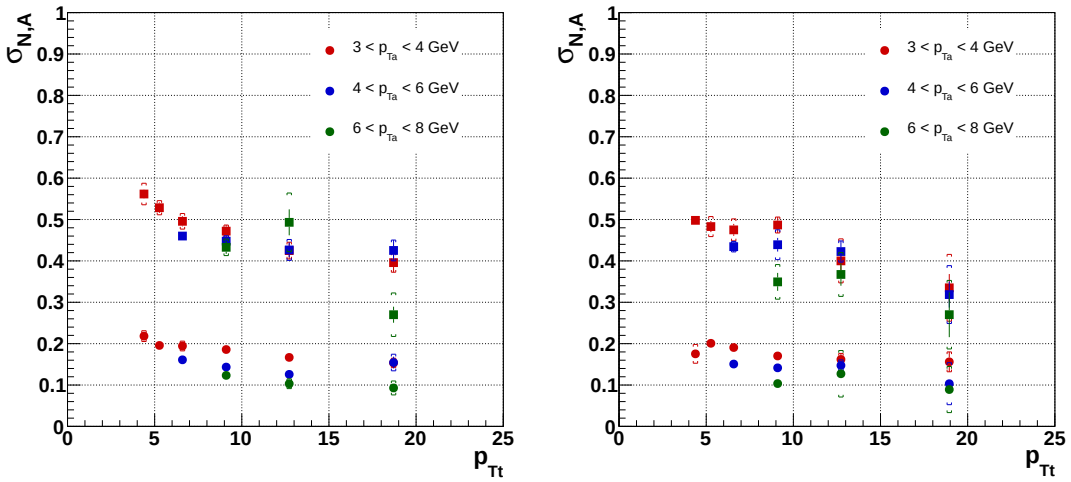

(a) (b)

Figure 5.3: Dependence of correlation function peak widths on p_{Tt} for various p_{Ta} windows. Circles denote nearside width σ_{N}, squares denote awayside σ_{A}. p_{Tt} values are given in GeV.
(a) $\sqrt{s} = 7$ TeV, (b) $\sqrt{s} = 2.76$ TeV.

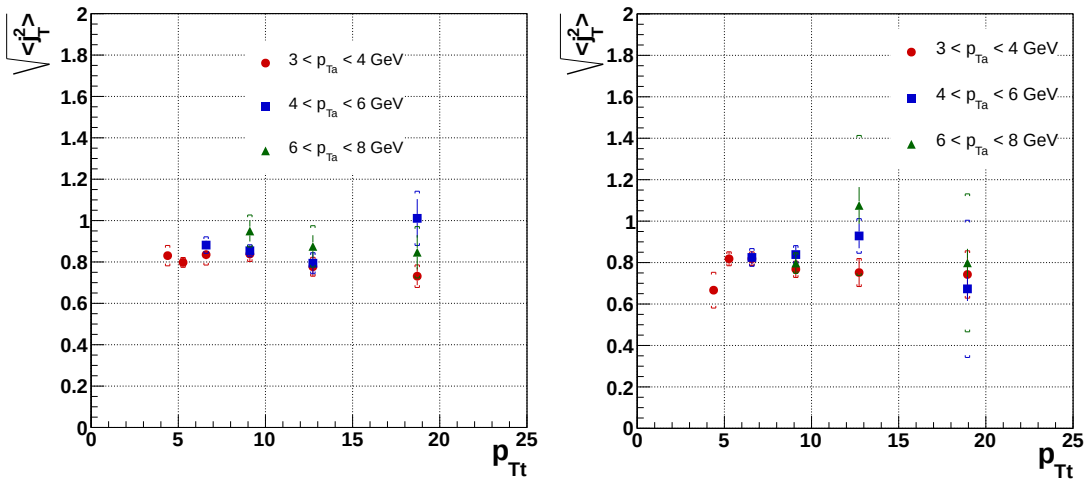

(a) (b)

Figure 5.4: $\sqrt{\langle j_{\mathrm{T}}^2 \rangle}$ values extracted from p–p data for various $p_{\mathrm{Tt,a}}$ bins. p_{Tt} values are given in GeV.
(a) $\sqrt{s} = 7$ TeV, (b) $\sqrt{s} = 2.76$ TeV.

5.2 Extracted j_{T} results

Values of $\sqrt{\langle j_{\mathrm{T}}^2 \rangle}$, determined following the method described in section 4.6.1, are presented in figure 5.4. It can be seen that the measured $\sqrt{\langle j_{\mathrm{T}}^2 \rangle}$ is independent of p_{Tt} and p_{Ta}, with a constant value of $\sqrt{\langle j_{\mathrm{T}}^2 \rangle} \approx 0.8$ GeV. This is higher than the values of around 0.6 GeV measured in $\sqrt{s} = 200$ GeV p–p collisions at RHIC [66], consistently with the expectation from QCD that $\sqrt{\langle j_{\mathrm{T}}^2 \rangle}$ should rise slowly with jet p_{T}, following $\sqrt{\langle j_{\mathrm{T}}^2 \rangle} \sim \sqrt{p_{\mathrm{Tjet}}}$ (and hence with collision energy) [98]. The expected difference in $\sqrt{\langle j_{\mathrm{T}}^2 \rangle}$ between the two collision energies studied in this analysis is too small to be identified in the results presented here.

5.3 Extracted k_{T} results

$\sqrt{\langle p_{\mathrm{out}}^2 \rangle}$ and $\langle x_{\mathrm{h}} \rangle$ were also calculated; the results are shown in figures 5.5 and 5.6, respectively. $\sqrt{\langle p_{\mathrm{out}}^2 \rangle}$ is observed to increase with increasing p_{Ta} and with decreasing

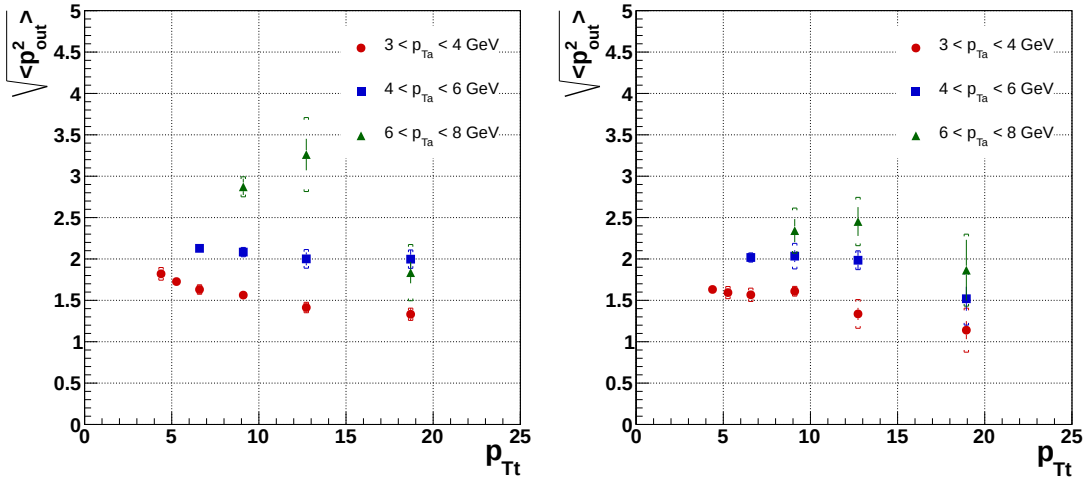

(a) (b)

Figure 5.5: $\sqrt{\langle p_{\mathrm{out}}^2 \rangle}$ values extracted from p–p data for various $p_{\mathrm{Tt,a}}$ bins. p_{Tt} values are given in GeV.
(a) $\sqrt{s} = 7$ TeV, (b) $\sqrt{s} = 2.76$ TeV.

p_{Tt}; this behaviour is expected from the equation for $\sqrt{\langle p_{\mathrm{out}}^2 \rangle} \approx \langle p_{\mathrm{Ta}} \rangle \sin \sigma_{\mathrm{A}}$ (equation 4.13), noting that σ_{A} decreases with increasing p_{Tt}. The dependence of $\langle x_{\mathrm{h}} \rangle$ on p_{Tt} and p_{Ta} arises trivially from the definition of x_{h}.

These results were then used, along with the $\sqrt{\langle j_{\mathrm{T}}^2 \rangle}$ results, to determine $\sqrt{\langle k_{\mathrm{T}}^2 \rangle}$ using the method described in section 4.6.3. The Monte-Carlo model described in appendix B was used to extract the values from the experimental measurements. These are shown in figure 5.7 as functions of p_{Tt} within given bins in p_{Ta}.

These results indicate that $\sqrt{\langle k_{\mathrm{T}}^2 \rangle}$ increases with $\sqrt{s}$ as expected from measurements at earlier experiments – values are measured of $\sqrt{\langle k_{\mathrm{T}}^2 \rangle} \approx 10$ GeV in $\sqrt{s} = 2.76$ TeV collisions and $\sqrt{\langle k_{\mathrm{T}}^2 \rangle} \approx 12$ GeV in $\sqrt{s} = 7$ TeV collisions, compared with the result of $\sqrt{\langle k_{\mathrm{T}}^2 \rangle} = 2.68$ GeV measured in $\sqrt{s} = 200$ GeV collisions at RHIC [66], and of 1.1 GeV measured in $\sqrt{s} = 62.4$ GeV collisions at the ISR [67]. However, some dependence on hadron p_{T} is also observed, contrary to previous measurements at lower beam energies: $\sqrt{\langle k_{\mathrm{T}}^2 \rangle}$ can be seen to increase with increasing p_{Tt} and p_{Ta}. This is suggested to be a consequence of the radiative origin of the measured acoplanarity.

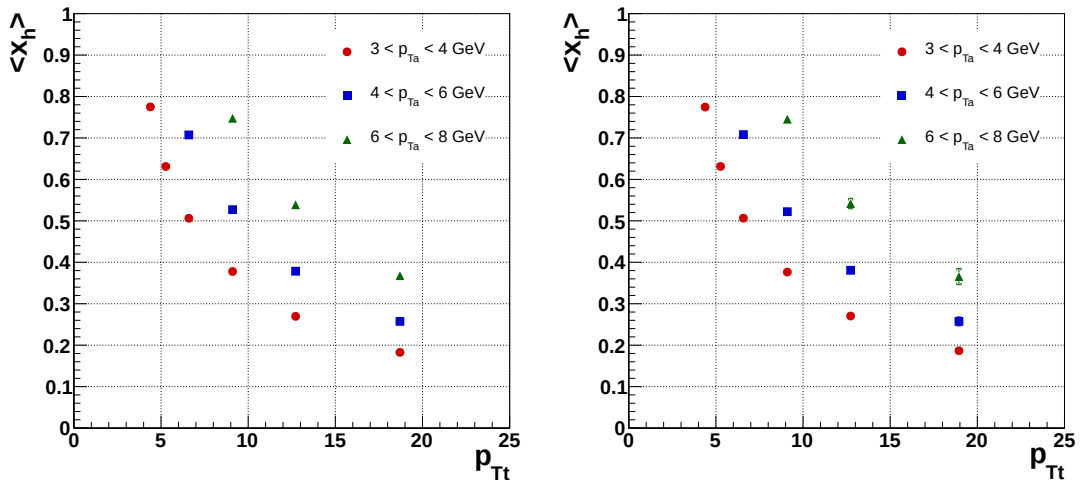

(a) (b)

Figure 5.6: $\langle x_{\mathrm{h}} \rangle$ values extracted from p–p data for various $p_{\mathrm{Tt,a}}$ bins. p_{Tt} values are given in GeV.
(a) $\sqrt{s} = 7$ TeV, (b) $\sqrt{s} = 2.76$ TeV.

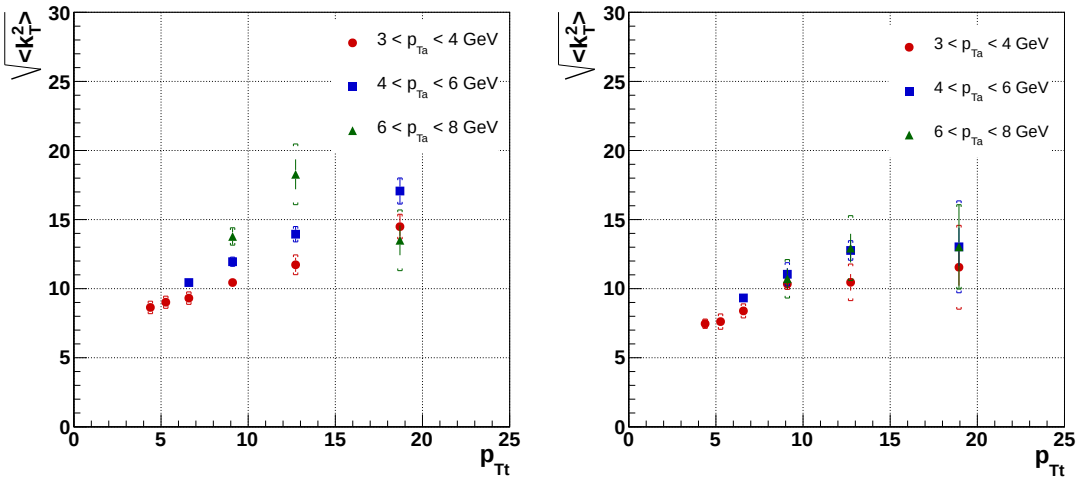

(a) (b)

Figure 5.7: $\sqrt{\langle k_{\mathrm{T}}^2 \rangle}$ values extracted from p–p data for various $p_{\mathrm{Tt,a}}$ bins. p_{Tt} values are given in GeV.
(a) $\sqrt{s} = 7$ TeV, (b) $\sqrt{s} = 2.76$ TeV.

5.4 Systematic uncertainties

The largest sources of systematic uncertainty in the minimum bias proton analysis were the choice of track cuts and the choice of the mechanism used to extract the peak widths. To determine the extent of the systematic effects, the track cuts and width extraction scheme were varied and the spread of the results calculated following the prescription in [99]. This prescription defines the systematic uncertainty on a data point as the standard deviation of the values of that data point according to the different methods, with the statistical uncertainty subtracted in quadrature. Thus, if the spread of the values from the different methods was consistent with statistical fluctuation, the calculated systematic uncertainty on that point would be zero.

The following sets of track cuts were used, listed here in order from least to most restrictive:

1. TPC tracks as defined in section 4.1.1.
2. Moderately tight cuts:
   (a) Combined ITS+TPC tracks.
   (b) At least 70 TPC clusters.
   (c) Same DCA requirements as (1).
3. Tight cuts:
   (a) Combined ITS+TPC tracks.
   (b) At least 70 TPC clusters.
   (c) Maximum DCA to vertex in beam direction $\mathrm{DCA}_z < 2$ cm.

The following schemes were used to determine the peak widths:

1. The distributions were fit to two nearside Gaussians, one awayside Gaussian plus a constant, as described in section 4.6.1.

2. The widths were taken as the background-subtracted RMSs of the distributions in the peak regions, with the background determined in the non-peak region under the assumption that between the peaks existed a region of zero jet yield.

3. As method 2, but with different widths for the defined "peak" and "background" regions.

By way of example, peak widths σ_{N} and σ_{A} extracted from $\sqrt{s} = 7$ TeV p–p data, with $4 < p_{\mathrm{Ta}} < 6$ GeV, are shown in figure 5.8. The same procedure was also used for the other p_{Ta} bins, for $\sqrt{s} = 2.76$ TeV data, and for the quantities calculated from the peak widths, but the plots are not shown here.

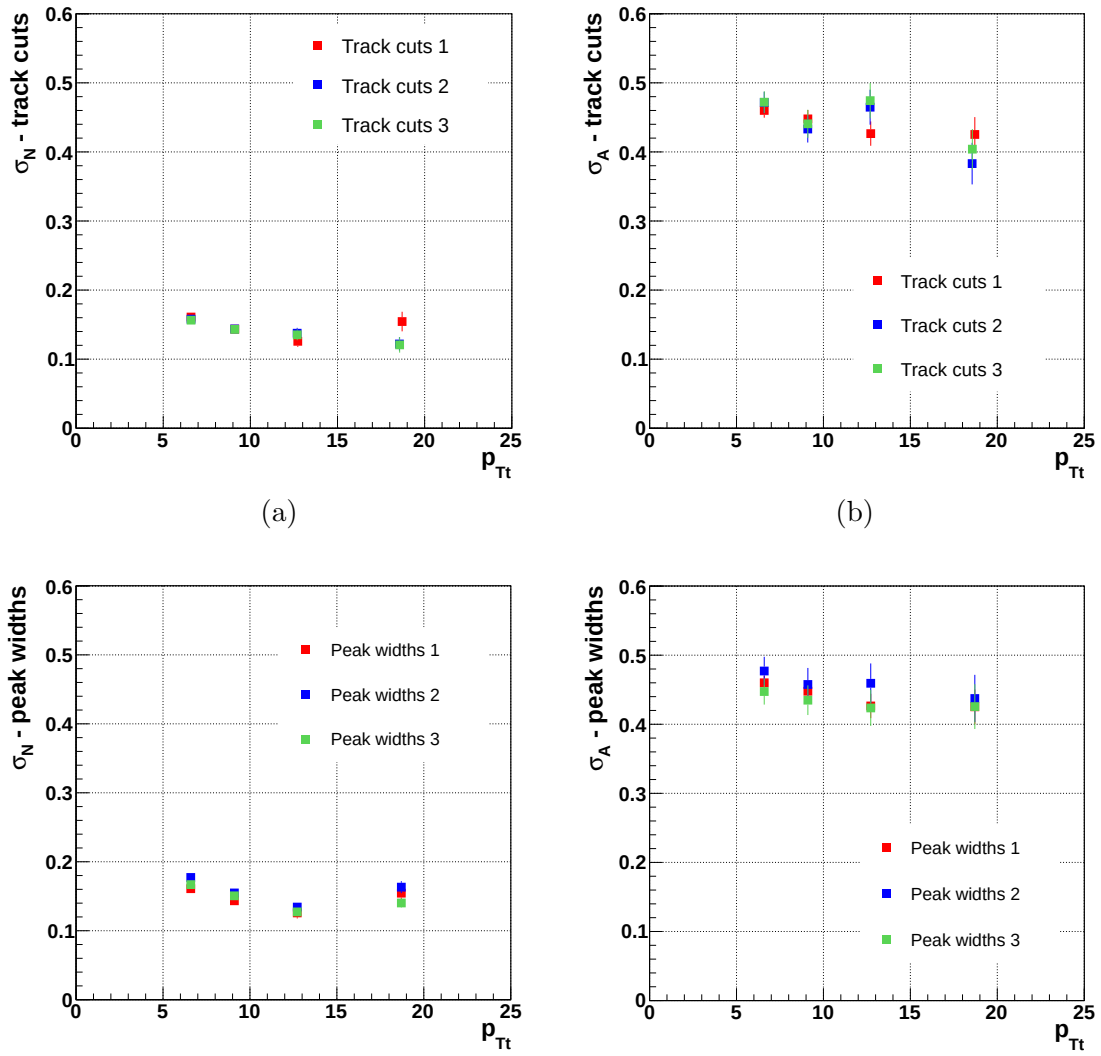

Figure 5.8: Near and awayside peak widths $\sigma_{\mathrm{N,A}}$ extracted from $\sqrt{s} = 7$ TeV p–p data using various methods, the spread of which was used to determine the systematic uncertainty. Only the $4 < p_{\mathrm{Ta}} < 6$ GeV bin is shown here. p_{Tt} values are given in GeV.
Top row shows the effects of using different track cuts on the (a) nearside width and (b) awayside width.
Bottom row shows the effects of using width determination schemes on the (c) nearside width and (d) awayside width.
The different methods are described in the text of section 5.4.

CHAPTER 6

JET YIELD DEPENDENCE ON MULTIPLICITY

This chapter presents the results of the yield study component of the analysis, as described in chapter 4. As detailed in section 4.1, the analysis used data from p–p collisions at $\sqrt{s} = 7$ TeV and $\sqrt{s} = 2.76$ TeV, and from Pb–Pb collisions at $\sqrt{s_{\mathrm{NN}}} = 2.76$ TeV. Background-subtracted correlation plots are shown for each system; the away/nearside yield ratios are then compared between the different systems. As explained in section 4.7 an increase in the degree of jet quenching, for example in Pb–Pb collisions of increasing centrality, would be expected to cause this ratio to fall below that expected in the absence of such effects.

The multiplicity and centrality binning used for each analysed system is shown in table 6.1. The centrality binning scheme for the peripheral Pb–Pb data was selected such that it corresponds to the same multiplicity binning that was used for

Table 6.1: Multiplicity/centrality binning for all analysed data. Binning for p–p data is defined in terms of multiplicity, and binning for Pb–Pb data is defined in terms of centrality.

Bin number	2.76 TeV p–p	7 TeV p–p	Pb–Pb	Pb–Pb (peripheral)
1	0–10	0–10	90%–60%	90%–88%
2	10–15	15–20	60%–50%	88%–85%
3	15–20	20–30	50%–40%	85%–81%
4	20–30	30–40	40%–30%	81%–77%
5	30–40	40–58	30%–20%	77%–73%
6	40–60	58–65	20%–10%	73%–70%
7	60–70	65–100	10%–5%	
8			5%–0%	

$\sqrt{s} = 2.76$ TeV data, with the most peripheral bin removed. For the $\sqrt{s} = 7$ TeV p–p data, the minimum bias trigger was used for bins 1–5, and the high multiplicity trigger for bins 6 and 7.

Unless otherwise stated, a p_{T} binning was used of $3 < p_{\mathrm{Ta}} < 8$ GeV and $8 < p_{\mathrm{Tt}} < 15$ GeV. In all plots of yields which follow, combined statistical and systematic uncertainties are shown as brackets around the statistical error bars; the scheme used to calculate these is described in section 6.3. Systematic uncertainties for the simulated Monte-Carlo data are not displayed.

6.1 Correlation function results

6.1.1 Results from 7 TeV proton data

Normalised, background-subtracted correlation plots were produced from $\sqrt{s} = 7$ TeV p–p data, following the binning outlined in table 6.1. The correlation plots for three bins are shown in figure 6.1. The near and awayside yields extracted from these are presented in figure 6.2, where they are compared with results from simulated Monte-Carlo data. The multiplicities are scaled by the mean multiplicity to

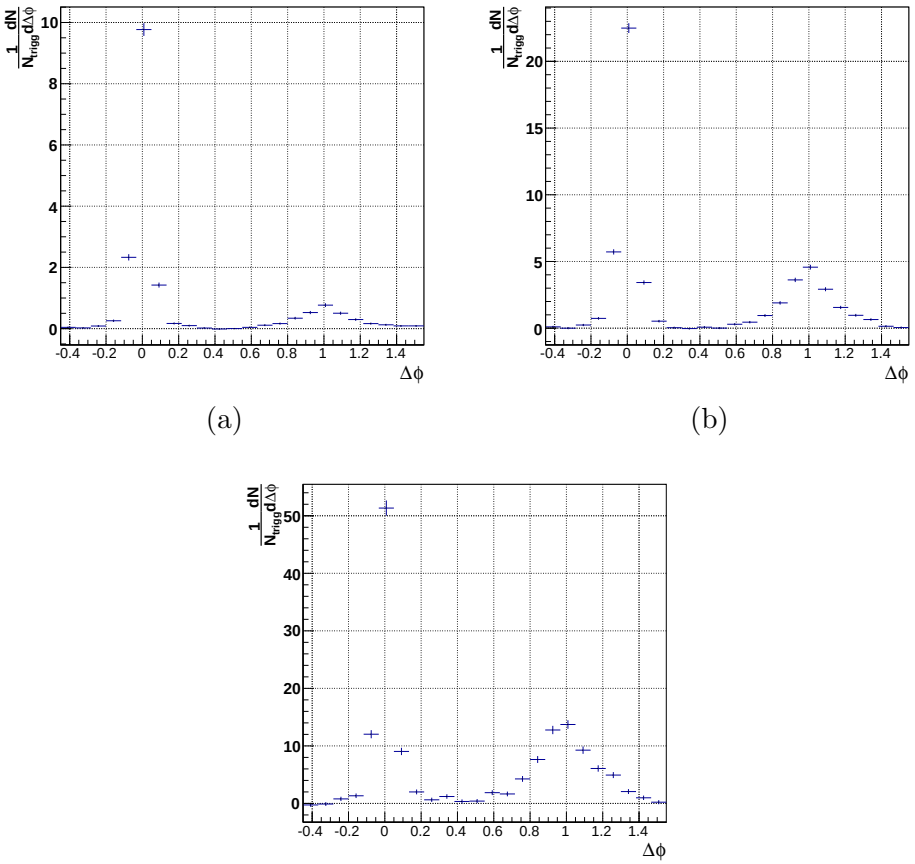

Figure 6.1: Normalised and background-subtracted correlation plots for $\sqrt{s} = 7$ TeV p–p data, for three multiplicity bins. (a) 0–10 tracks, (b) 30–40 tracks, (c) 65–100 tracks. (a) and (b) were produced from minimum bias triggered data, (c) was produced from high multiplicity triggered data.

account for the difference in slope between the multiplicity spectra in real and simulated data; with this correction applied the Monte-Carlo can be seen to describe the data well.

The yields are expected to rise with multiplicity, as observed, due to a bias towards harder collisions in higher multiplicity events. This effect is compounded on the awayside by acceptance effects, with higher multiplicity events being more likely to have both jets within the detector acceptance.

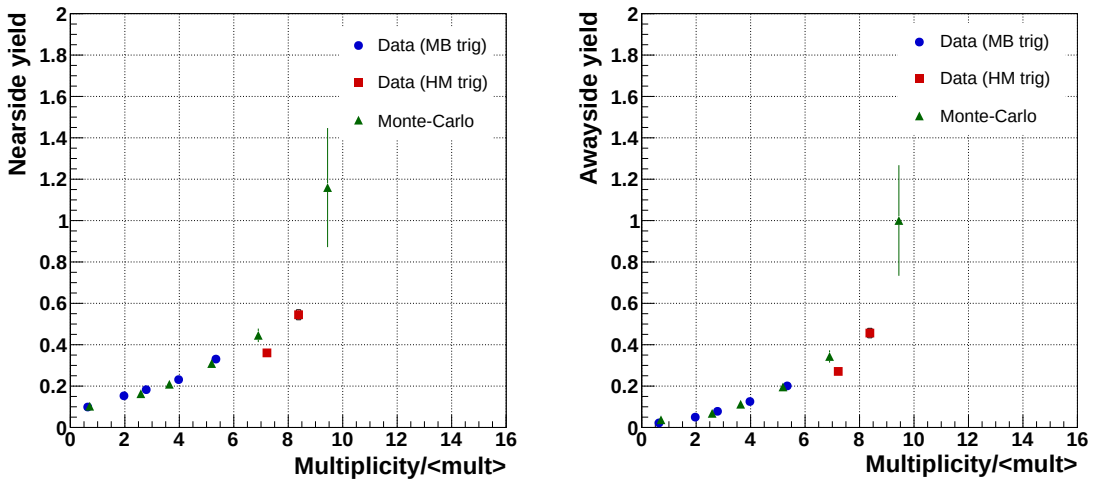

(a) (b)

Figure 6.2: Comparison of extracted $\sqrt{s} = 7$ TeV p–p yields from data with those from MC simulations. $3 < p_{\mathrm{Ta}} < 8$ GeV; $8 < p_{\mathrm{Tt}} < 15$ GeV. (a) Nearside yield, (b) awayside yield.

6.1.2 Results from 2.76 TeV proton data

Analogously to the previous section, normalised and background-subtracted correlation plots were produced from $\sqrt{s} = 2.76$ TeV data and three such plots are shown in figure 6.3. The near and awayside yields extracted from these are compared with those from simulated Monte-Carlo data in figure 6.4. It can be seen that, with the multiplicity scaled by the mean multiplicity, the Monte-Carlo data match the real data well.

6.1.3 Results from ion data

As shown in table 6.1, two centrality binning schemes were used for $\sqrt{s_{\mathrm{NN}}} = 2.76$ TeV Pb–Pb data, one spanning the full range of centrality from 90% to 0%, and one spanning a more limited range from 90% to 70%, corresponding to the multiplicity binning used for $\sqrt{s} = 2.76$ TeV p–p data, to allow direct comparison between the two systems. Three sample plots from those binned over the full

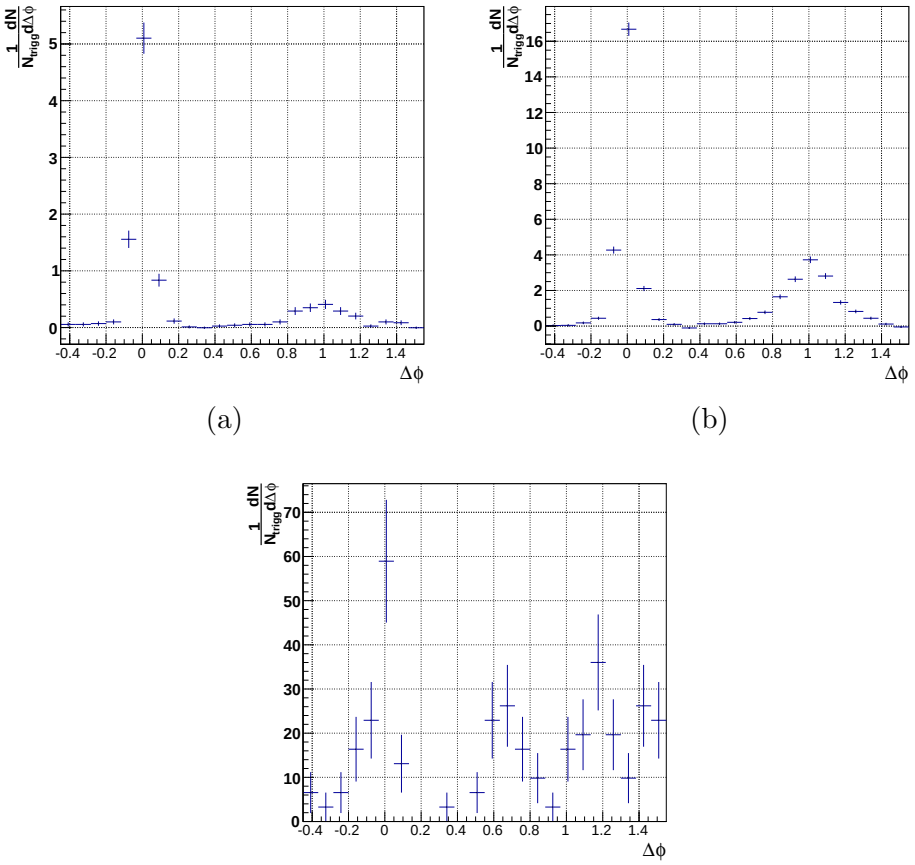

Figure 6.3: Normalised and background-subtracted correlation plots for three multiplicity bins in $\sqrt{s} = 2.76$ TeV p–p data. (a) 0–10 tracks, (b) 20–30 tracks, (c) 60–70 tracks.

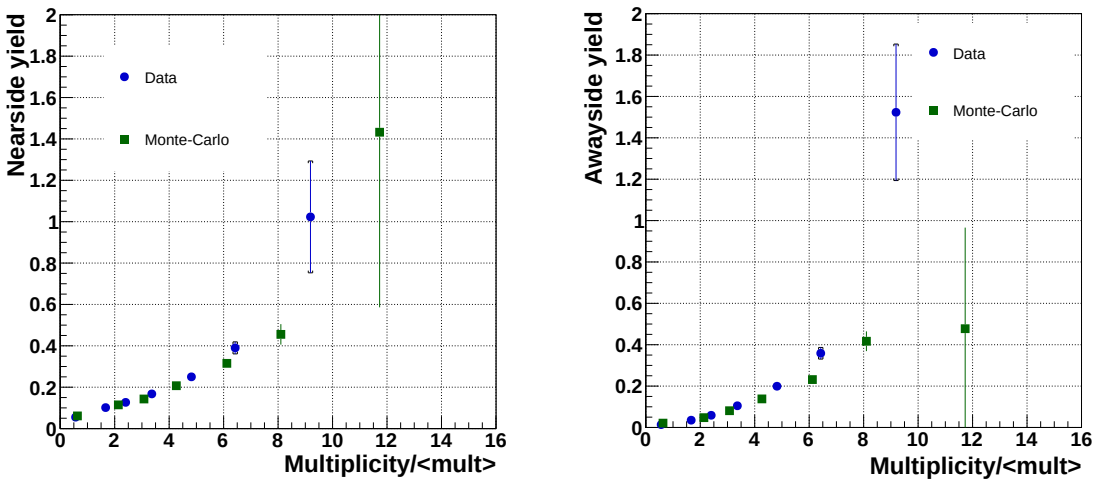

(a) (b)

Figure 6.4: Comparison of extracted $\sqrt{s} = 2.76$ TeV p–p yields from data with those from MC simulations. $3 < p_{\mathrm{Ta}} < 8$ GeV; $8 < p_{\mathrm{Tt}} < 15$ GeV. (a) Nearside yield, (b) awayside yield.

range of centrality are presented in figure 6.5, and three of those from the peripheral binning scheme are presented in figure 6.6.

Near and awayside yields extracted from the correlation plots over the full range of multiplicity are presented in figure 6.7. For consistency with the p–p data, centralities are expressed in terms of multiplicity rather than as a percentage. It can be seen that the awayside yield falls in increasingly central collisions, while the same is not the case for the nearside yield. This suppression of the awayside is interpreted as a consequence of jet quenching.

6.2 Yield comparisons between systems

As described in section 4.7, it would be expected that jet quenching would suppress the awayside yield relative to the nearside, causing the away/nearside yield ratio to fall in Pb–Pb collisions of increasing centrality. Figure 6.8 shows this ratio as a function of increasing centrality (expressed in terms of multiplicity as well as

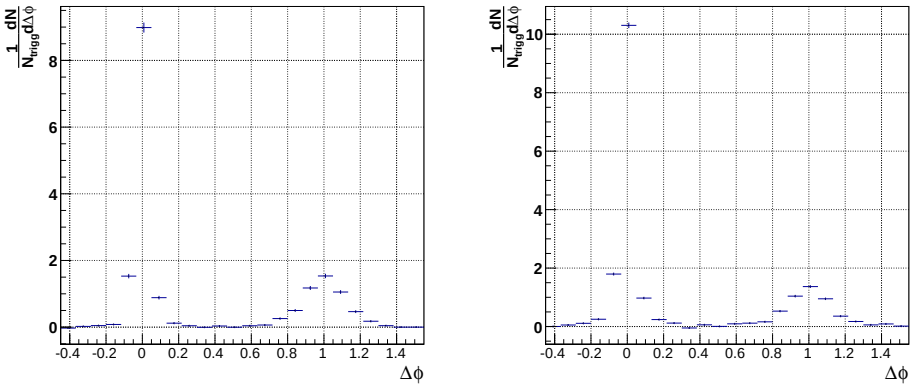

(a) (b)

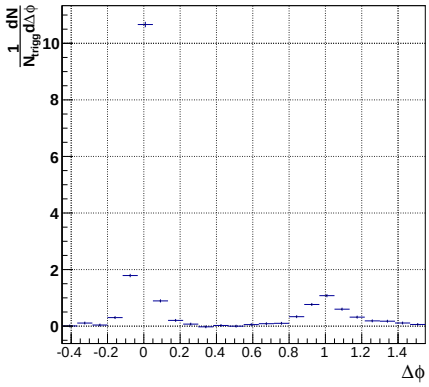

(c)

Figure 6.5: Normalised and background-subtracted correlation plots for $\sqrt{s_{\mathrm{NN}}} = 2.76$ TeV Pb–Pb data, for three centrality bins. (a) 60%–90%, (b) 30%–40%, (c) 0%–5%.

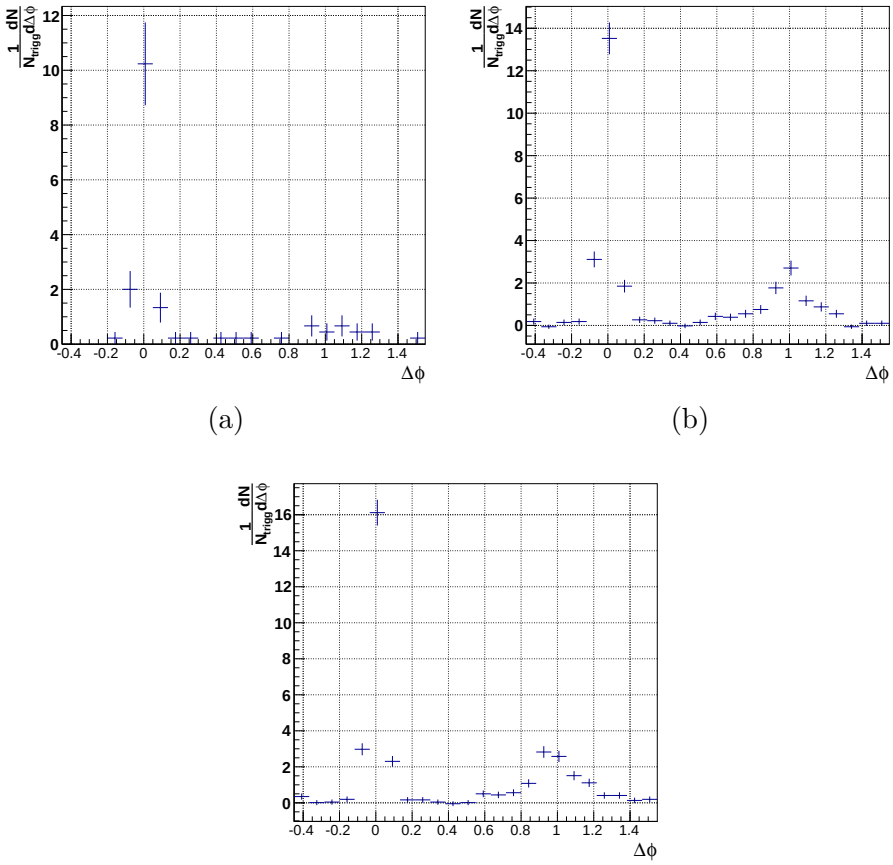

Figure 6.6: Normalised and background-subtracted correlation plots for peripheral $\sqrt{s_{\mathrm{NN}}} = 2.76$ TeV Pb–Pb data, for three centrality bins. (a) 88%–90%, (b) 77%–81%, (c) 70%–73%.

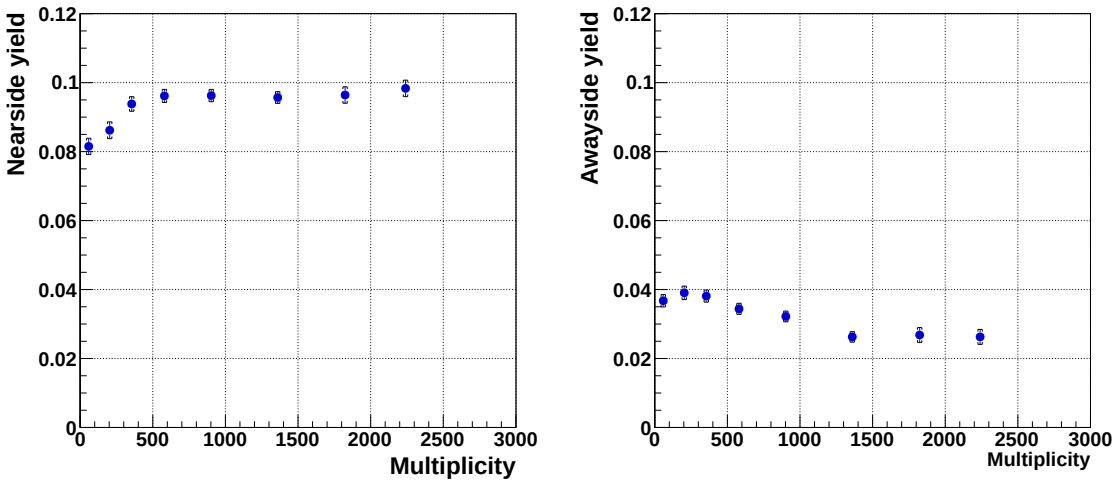

(a) (b)

Figure 6.7: Yields extracted from $\sqrt{s_{\mathrm{NN}}} = 2.76$ TeV Pb–Pb data. $3 < p_{\mathrm{Ta}} < 8$ GeV; $8 < p_{\mathrm{Tt}} < 15$ GeV. (a) Nearside yield, (b) awayside yield.

centrality percentile) from Pb–Pb data. It can be seen that the ratio does indeed fall for more central collisions.

Presented in figure 6.9 is the away/near yield ratio as a function of multiplicity (scaled by mean multiplicity [40]) for p–p collisions at $\sqrt{s} = 7$ TeV and $\sqrt{s} = 2.76$ TeV, compared with results from Pythia simulations of the same energies. The ratios are observed to rise with multiplicity, an effect which is expected as a consequence of a bias in higher multiplicity bins towards dijet events with both jets inside the detector acceptance. This behaviour was reproduced in a Monte-Carlo model, and was also observed in Pythia data as shown on the plot.

The ratio for $\sqrt{s} = 7$ TeV data, for which stronger QGP effects would be expected (if present at all), is consistently lower than that for $\sqrt{s} = 2.76$ TeV data. However, as the ratio was not observed to fall or to plateau at a value of less than 1 at higher multiplicities, and as this was broadly consistent with Pythia, this cannot be interpreted as evidence for QGP production. This is consistent with other results indicating that dijet production cross sections in p–p collisions are generally well-described by QCD predictions [100].

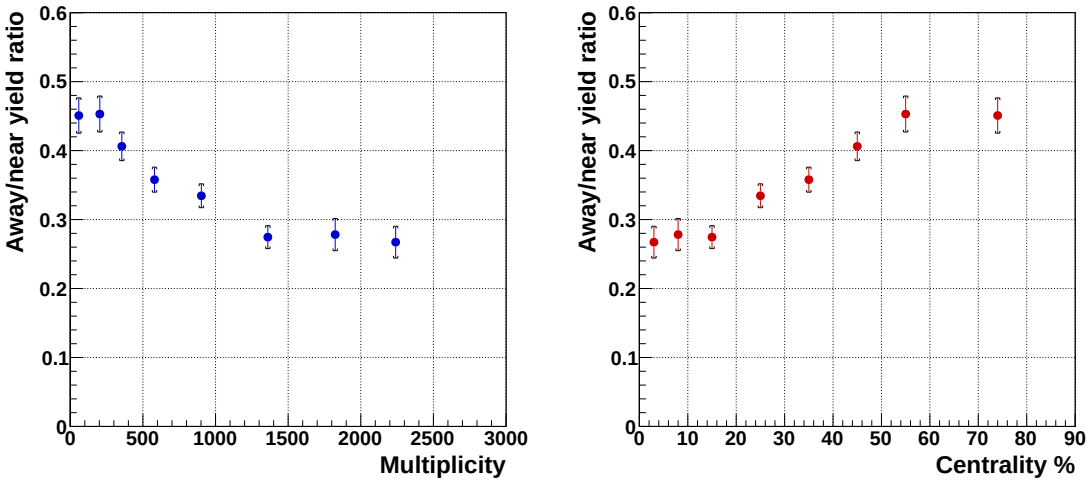

(a) (b)

Figure 6.8: Away/nearside yield ratios from Pb–Pb collisions with $3 < p_{\mathrm{Ta}} < 8$ GeV and $8 < p_{\mathrm{Tt}} < 15$ GeV, over the full centrality range. (a) shows the ratio in terms of multiplicity, and (b) in terms of centrality. Note that that increasing centrality percentile is equivalent to decreasing multiplicity.

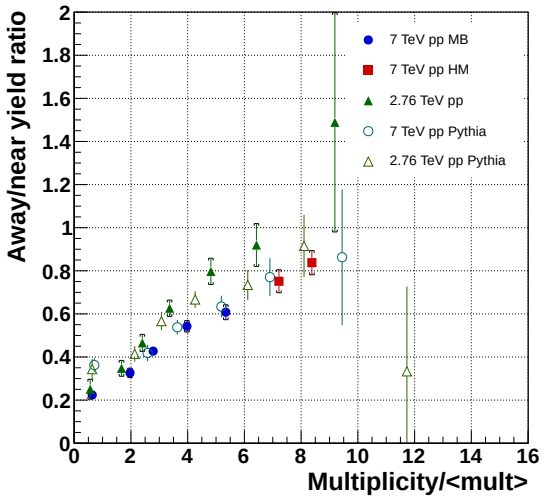

Figure 6.9: Comparison of away/nearside yield ratios from $\sqrt{s} = 2.76$ TeV and $\sqrt{s} = 7$ TeV p–p collisions, with multiplicities scaled by mean multiplicity. Results from simulated Pythia data are also shown. $3 < p_{\mathrm{Ta}} < 8$ GeV; $8 < p_{\mathrm{Tt}} < 15$ GeV

The yield ratios extracted from $\sqrt{s} = 2.76$ TeV p–p collisions were also compared to those from peripheral $\sqrt{s_{\mathrm{NN}}} = 2.76$ TeV Pb–Pb collisions. These results are presented in figure 6.10. It can be seen that while the yield ratios for the two systems match closely at low multiplicities, at higher multiplicities the yields diverge and the peripheral Pb–Pb data do not exhibit the rise with multiplicity observed in the p–p data.

The divergence between the two distributions is interpreted as being a consequence of the differing mechanisms by which a high multiplicity event can be produced – in proton collisions, high multiplicities are generally produced in events with two hard jets, both of which are produced within the detector acceptance. While this mechanism also occurs in Pb–Pb events it is possible, and indeed more likely, to produce high multiplicities from a superposition of many soft nucleon–nucleon collisions – results from the Monte-Carlo Glauber model described in appendix C indicate that a Pb–Pb event with 50 tracks typically has around 10 participants and 25 binary nucleon–nucleon collisions. As these events are generally more isotropic than a typical dijet event, the acceptance effects are not as pronounced and the rise of yield ratio with multiplicity is not observed.

The results presented in this chapter indicate that high multiplicity p–p collisions are dominantly jet-like and therefore non-thermal, and hence are not equivalent to peripheral Pb–Pb collisions of comparable multiplicity. Broadly speaking, this is because jet suppression is a soft QCD effect in an extended deconfined medium, but multiplicity in proton collisions is correlated not with the size of any produced medium but instead with the number of jets inside the detector acceptance.

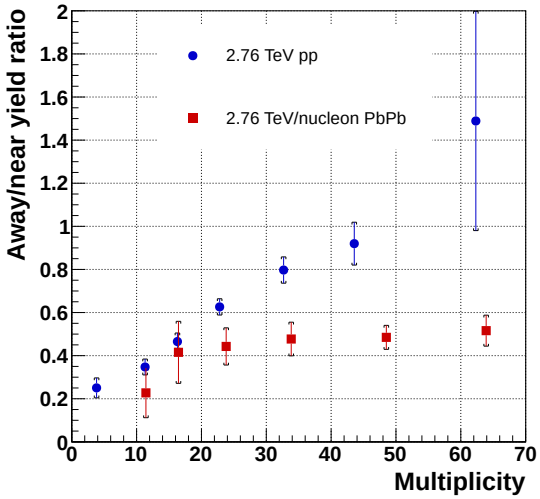

Figure 6.10: Away/nearside yield ratios from peripheral $\sqrt{s_{\mathrm{NN}}} = 2.76$ TeV Pb–Pb collisions, compared with $\sqrt{s} = 2.76$ TeV p–p collisions over the same multiplicity range. $3 < p_{\mathrm{Ta}} < 8$ GeV; $8 < p_{\mathrm{Tt}} < 15$ GeV.

6.3 Systematic uncertainties

The most significant sources of systematic uncertainty in the yield analysis arose from the subtraction of the uncorrelated pedestal background, and from the choice of track cuts. To quantify the extent of these effects, the pedestal subtraction scheme and track cuts were varied, and the spread of the results calculated according to [99].

The following pedestal subtraction schemes were used:

1. ZYAM method as described in section 4.7.
2. As method 1, but with a ZYAM background region twice as wide.
3. As method 1, but with the ZYAM background region fixed to the geometric midpoint between the two peaks.
4. Background extracted from a fit of the correlation plots to two peaks plus a constant.

The following sets of track cuts were used:

1. TPC tracks as defined in section 4.1.1.
2. Moderately tight cuts:
   (a) Combined ITS+TPC tracks.
   (b) At least 70 TPC clusters.
   (c) Same DCA requirements as (1).
3. Tight cuts:
   (a) Combined ITS+TPC tracks.
   (b) At least 70 TPC clusters.
   (c) Maximum DCA to vertex in beam direction $\mathrm{DCA}_z < 2$ cm.

The yields and ratios extracted from $\sqrt{s} = 2.76$ TeV p–p data using these various methods are presented in figure 6.11. The same method was used to calculate systematic uncertainties for the other analysed datasets, but the plots are not shown here.

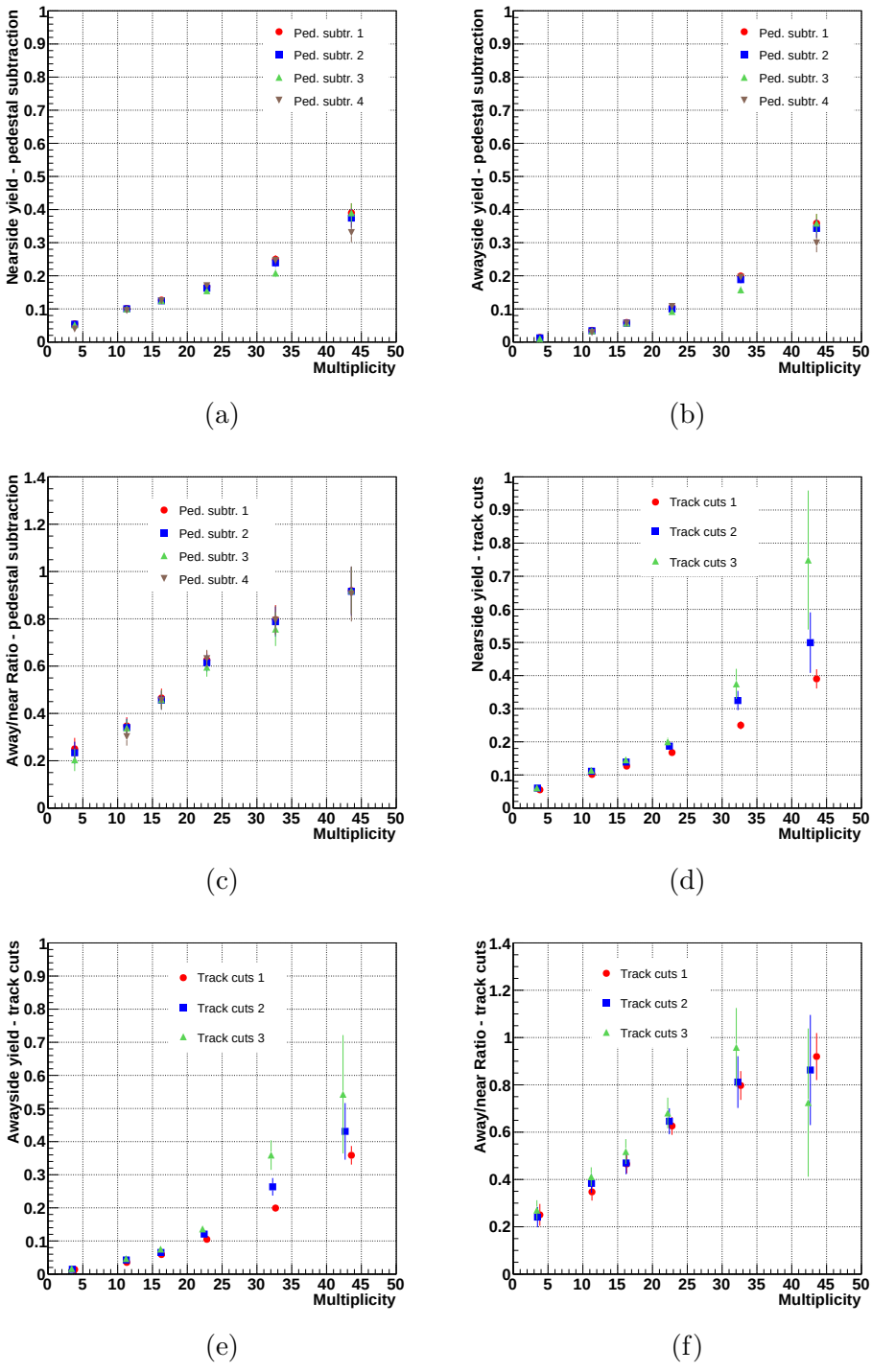

Figure 6.11: Near and awayside yields, and away/nearside yield ratios, extracted from $\sqrt{s} = 2.76$ TeV p–p data using varied methods, the spread of which is used to determine the systematic uncertainty.
Top row shows the effects of using different pedestal subtraction schemes on the (a) nearside yield, (b) awayside yield and (c) away/nearside yield ratio.
Bottom row shows the effects of using difference track cuts on the (d) nearside yield, (e) awayside yield and (f) away/nearside yield ratio.
The different methods used are described in the text of section 6.3.

CHAPTER 7

JET SHAPE DEPENDENCE ON MULTIPLICITY

This chapter presents the results of the analysis of jet shape dependence on event multiplicity. The analysis uses the same data as used in the yield analysis. As detailed in section 4.1, this comprised data from p–p collisions at $\sqrt{s} = 7$ TeV and $\sqrt{s} = 2.76$ TeV and Pb–Pb collisions as $\sqrt{s_{\mathrm{NN}}} = 2.76$ TeV.

The multiplicity and centrality binning was unchanged from that outlined in table 6.1, with the exception that the highest multiplicity bin was removed from the $\sqrt{s} = 2.76$ TeV p–p data and the most peripheral removed from the peripheral Pb–Pb data. This was necessitated by there being insufficient statistics in these bins for a reliable fit.

As with the yield analysis, trigger and associated p_{T} bins of $8 < p_{\mathrm{Tt}} < 15$ GeV and

$3 < p_{\mathrm{Ta}} < 8$ GeV were used. Combined statistical and systematic uncertainties are shown on the plots as brackets around the statistical error bars; the method used for calculating these is presented in section 7.4.

7.1 Correlation function results

As described in section 4.6.1, the normalised correlation plots shown in section 6.1 were fit to the function given in equation 4.9 of two nearside Gaussians, one awayside Gaussian and a constant background. The results of these fits are shown for some sample multiplicity bins for all collision systems and beam energies in figures 7.1–7.4.

7.2 Correlation peak widths

The peak widths $\sigma_{\mathrm{N,A}}$ extracted from the fits to p–p data are presented in figure 7.5, and those from Pb–Pb data are presented in figure 7.6. The nearside peak widths were taken as the combined widths of the two nearside Gaussians in the fit, as defined in equation 4.10.

Extraction of $\sqrt{\langle k_{\mathrm{T}}^2 \rangle}$ from these correlation functions was not possible using the method described in this document. Multiplicity in a jet event is a product of both Q^2 (with harder scattering causing higher jet multiplicity) and acceptance effects (with high multiplicity jet events being more likely to have both jets inside the detector acceptance), requiring a proper treatment of jet fragmentation in the model used for the extraction of k_{T}. This is beyond the scope of a model such as that used in this work.

However, given that in heavy ion collisions the majority of the observed multiplicity originates from soft processes, in the absence of medium effects the shape of the

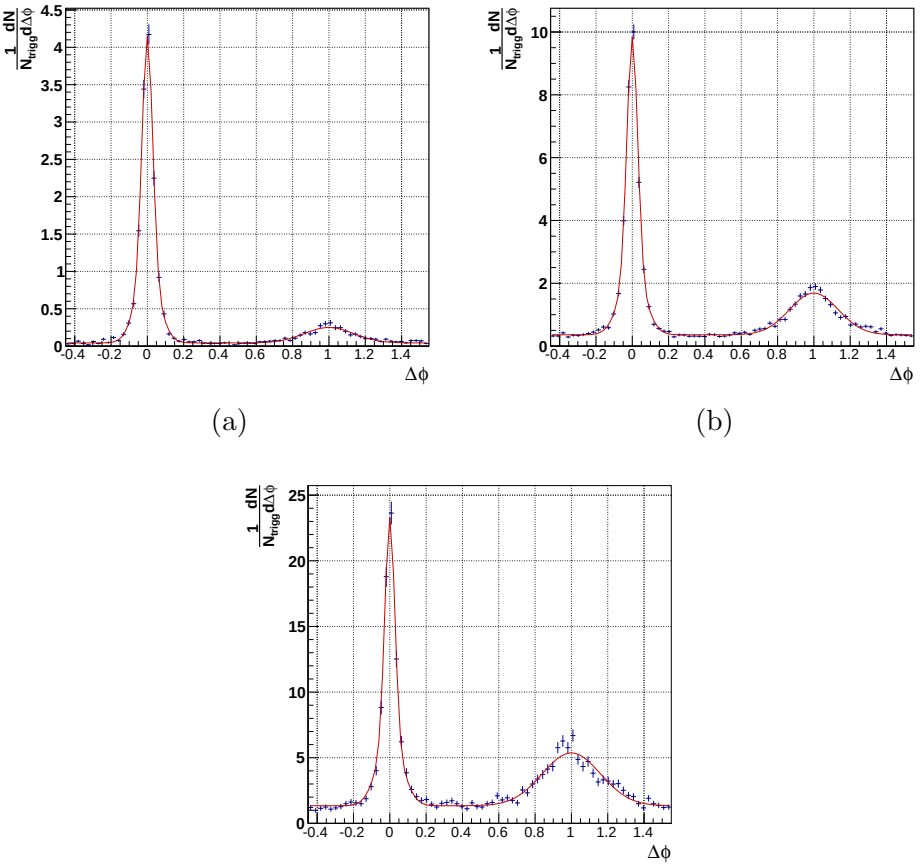

Figure 7.1: Normalised correlation plots for $\sqrt{s} = 7$ TeV p–p data, for three multiplicity bins, fit to two nearside Gaussians + awayside Gaussian + constant. (a) 0–10 tracks, (b) 30–40 tracks, (c) 65–100 tracks. (a) and (b) were produced from minimum bias triggered data, (c) was produced from high multiplicity triggered data.

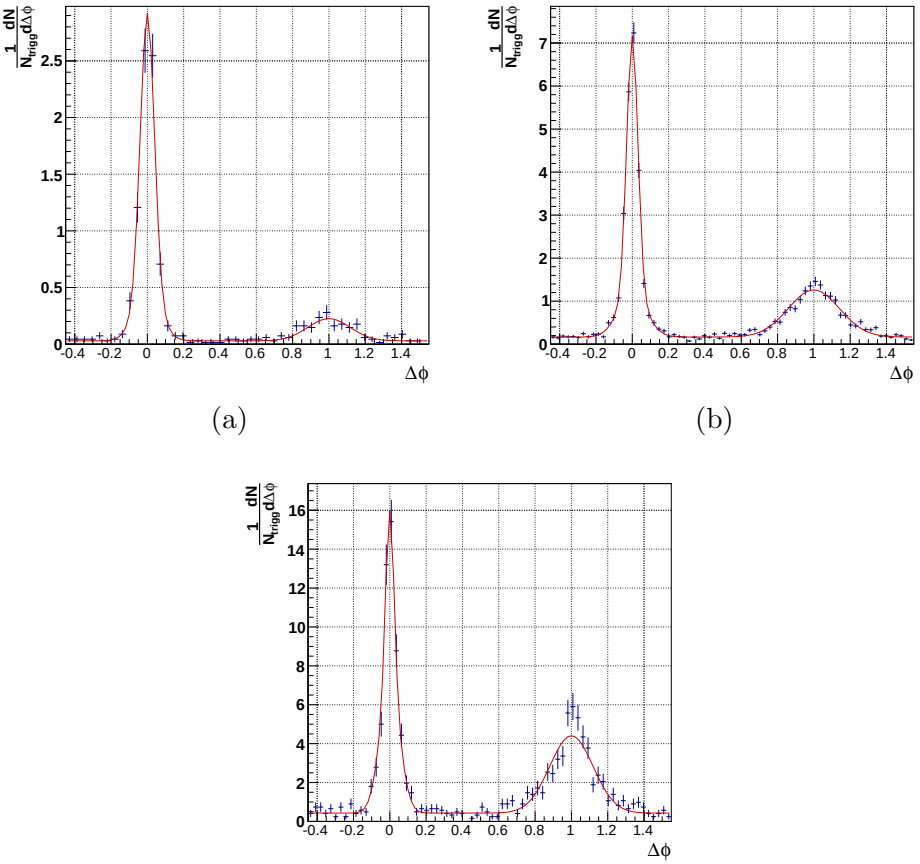

Figure 7.2: Normalised correlation plots for $\sqrt{s} = 2.76$ TeV p–p data, for three multiplicity bins, fit to two nearside Gaussians + awayside Gaussian + constant. (a) 0–10 tracks, (b) 20–30 tracks, (c) 40–60 tracks.

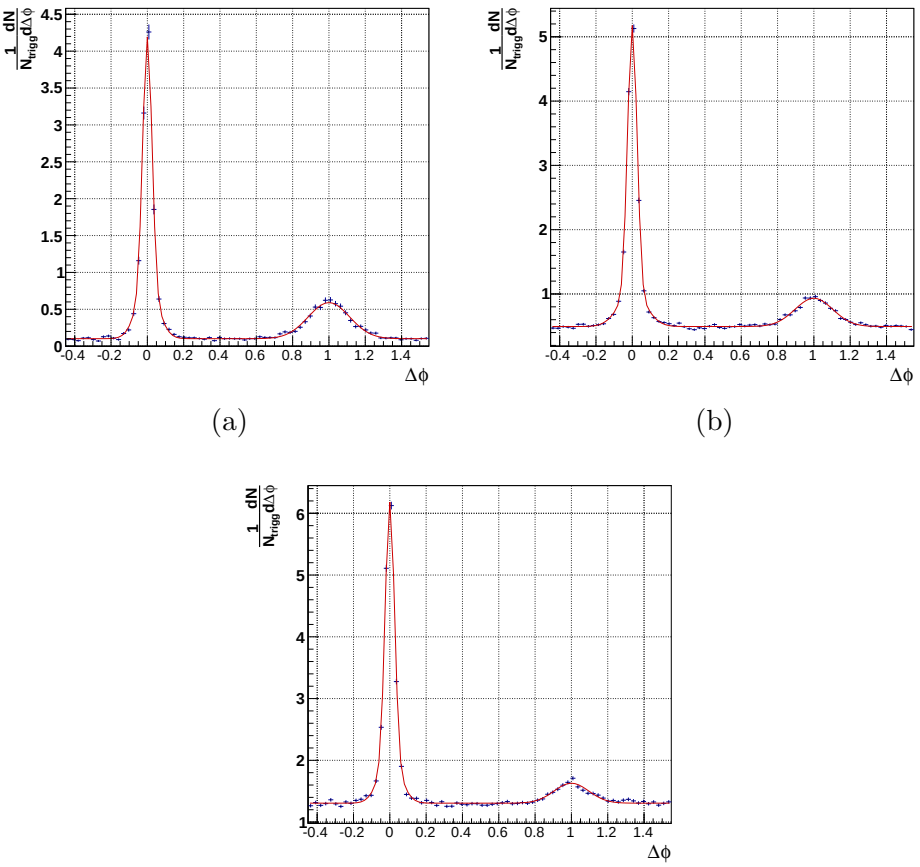

Figure 7.3: Normalised correlation plots for $\sqrt{s_{\mathrm{NN}}} = 2.76$ TeV Pb–Pb data, for three centrality bins, fit to two nearside Gaussians + awayside Gaussian + constant. (a) 60%–90%, (b) 30%–40%, (c) 0%–5%.

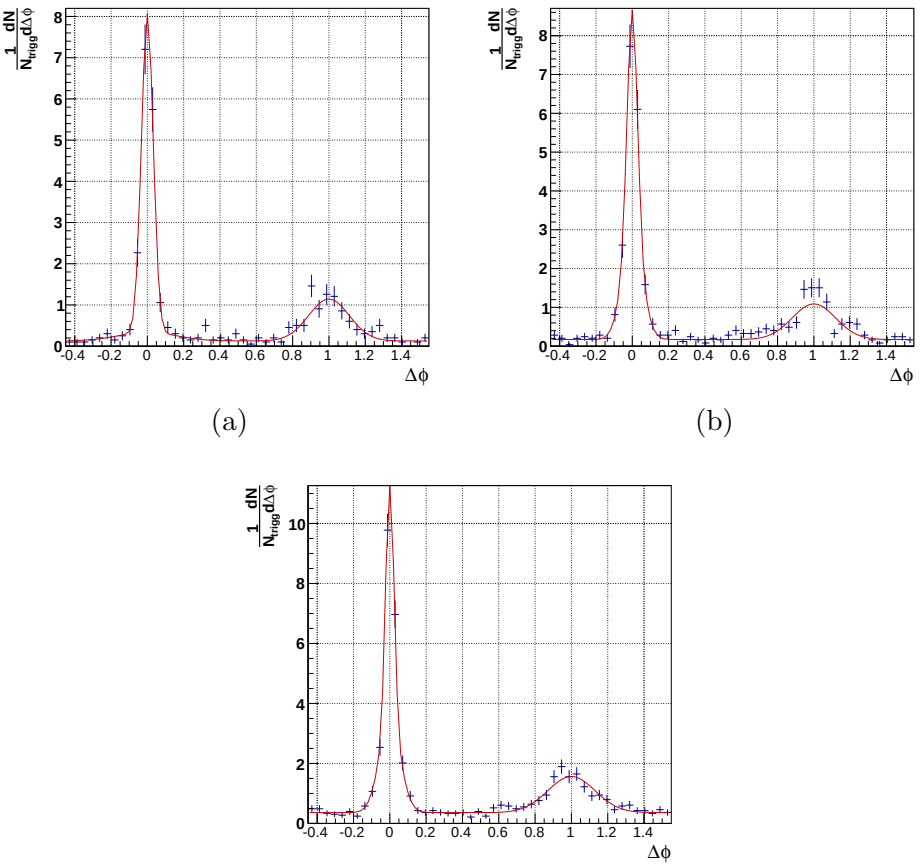

Figure 7.4: Normalised correlation plots for peripheral $\sqrt{s_{\mathrm{NN}}} = 2.76$ TeV Pb–Pb data, for three centrality bins, fit to two nearside Gaussians + awayside Gaussian + constant. (a) 81%–85%, (b) 77%–81%, (c) 70%–73%.

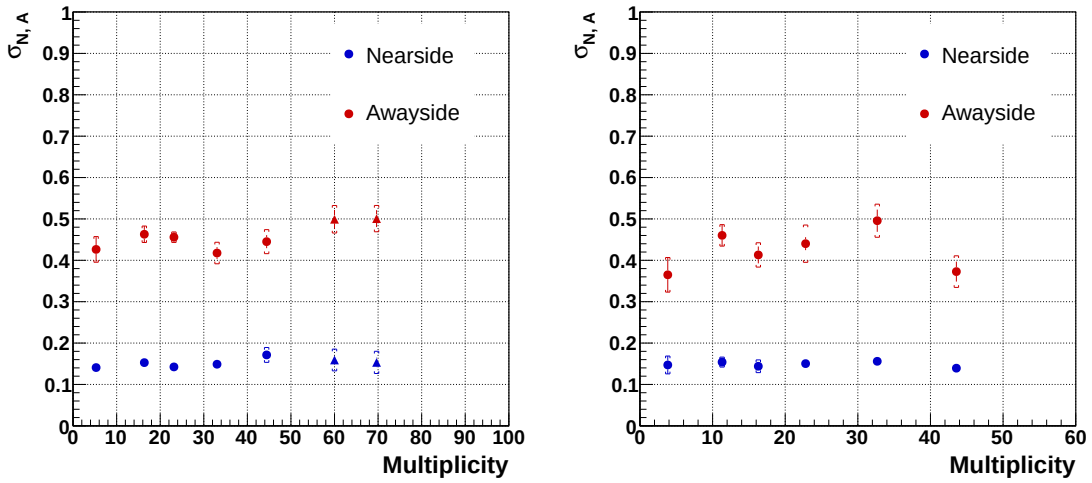

(a) (b)

Figure 7.5: Values of σ_{N} and σ_{A} extracted from correlation functions from p–p data with $8 < p_{\mathrm{Tt}} < 15$ GeV and $3 < p_{\mathrm{Ta}} < 8$ GeV. (a) $\sqrt{s} = 7$ TeV, with circles indicating minimum bias triggered data and triangles indicating high multiplicity triggered data. (b) $\sqrt{s} = 2.76$ TeV.

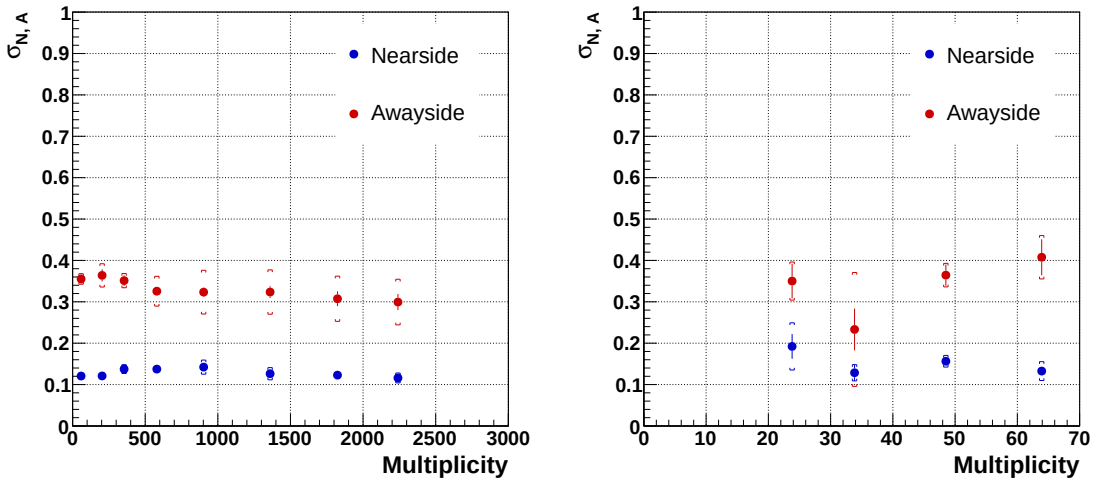

(a) (b)

Figure 7.6: Values of σ_{N} and σ_{A} extracted from correlation functions from $\sqrt{s_{\mathrm{NN}}} = 2.76$ TeV Pb–Pb data with $8 < p_{\mathrm{Tt}} < 15$ GeV and $3 < p_{\mathrm{Ta}} < 8$ GeV. (a) full multiplicity (centrality) range, (b) peripheral region.

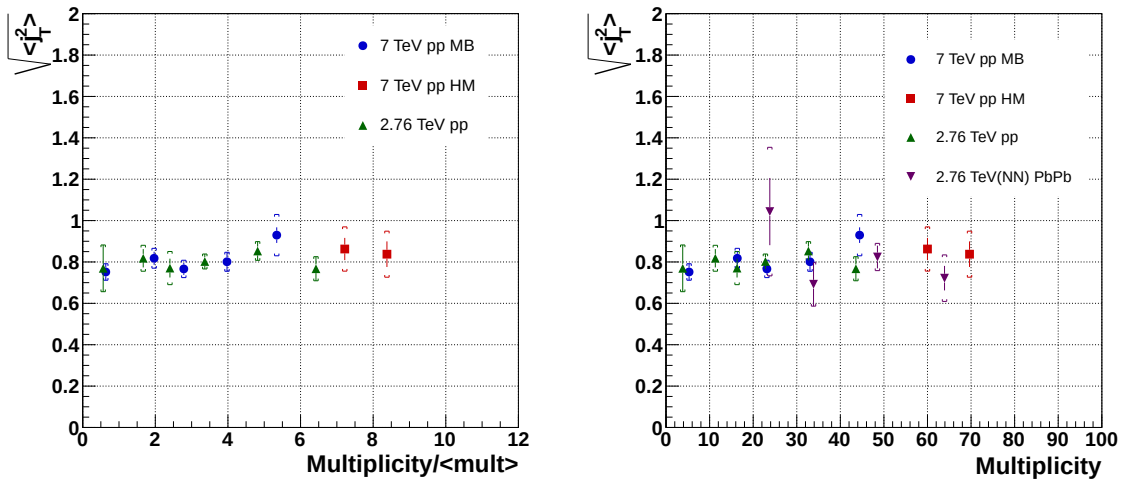

(a) (b)

Figure 7.7: Comparison of $\sqrt{\langle j_{\mathrm{T}}^2 \rangle}$ extracted from (a) p–p data at $\sqrt{s} = 7$ TeV and $\sqrt{s} = 2.76$ TeV, with multiplicity scaled by mean multiplicity, and (b) the same p–p data and also peripheral $\sqrt{s_{\mathrm{NN}}} = 2.76$ TeV Pb–Pb data. $8 < p_{\mathrm{Tt}} < 15$ GeV; $3 < p_{\mathrm{Ta}} < 8$ GeV.

correlation function (for sufficiently high p_{T} hadrons) is independent of centrality. Figure 7.6a shows a slight downward trend in σ_{A} with increasing centrality, but given the systematic uncertainties it is difficult to draw conclusions.

The near and awayside peak widths measured in p–p collisions are consistent with being independent of multiplicity, as are the nearside peak widths measured in Pb–Pb collisions.

7.3 Shape results

Figure 7.7 shows the values of the RMS jet fragmentation transverse momentum $\sqrt{\langle j_{\mathrm{T}}^2 \rangle}$, extracted from p–p and peripheral Pb–Pb data according to the method described in section 4.6.1. It can be seen that for all systems, $\sqrt{\langle j_{\mathrm{T}}^2 \rangle}$ is constant at around $\sqrt{\langle j_{\mathrm{T}}^2 \rangle} \approx 0.8$ GeV. This is consistent with the minimum bias proton results presented in section 5.2.

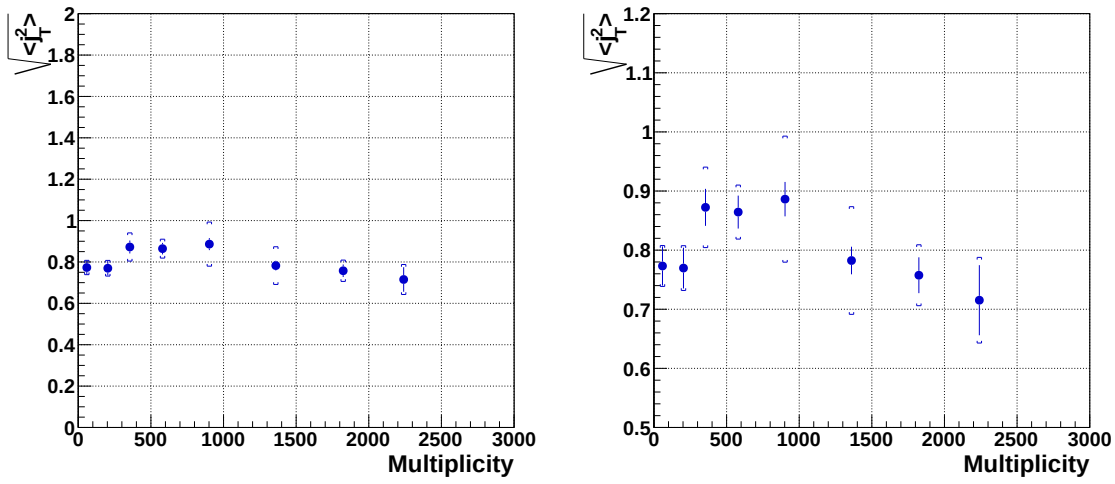

(a) (b)

Figure 7.8: $\sqrt{\langle j_{\mathrm{T}}^2 \rangle}$ values extracted from $\sqrt{s_{\mathrm{NN}}} = 2.76$ TeV Pb–Pb data with $8 < p_{\mathrm{Tt}} < 15$ GeV and $3 < p_{\mathrm{Ta}} < 8$ GeV, over the full multiplicity (centrality) range. (b) shows the same but with the y axis zoomed in.

The $\sqrt{\langle j_{\mathrm{T}}^2 \rangle}$ results for Pb–Pb data over the full range of centrality are shown in figure 7.8. A slight downward trend is visible, with $\sqrt{\langle j_{\mathrm{T}}^2 \rangle}$ decreasing slightly in increasingly central collisions. As mentioned above, in the absence of medium effects the hard processes are expected to be independent of centrality, and thus this may be interpreted as a consequence of interaction with the medium. With no observed σ_{N} narrowing, this effect can be caused by a suppression of the high p_{T} hadrons in the jet; this would be qualitatively consistent with measurements at other experiments [101].

7.4 Systematics

As with the analysis of j_{T} and k_{T} in minimum bias p–p data presented in chapter 5, the largest sources of systematic uncertainty in the study of jet shape and imbalance as a function of multiplicity were the choice of track cuts and the choice of scheme used to extract the peak widths. To determine the magnitude of these effects the

same procedure was used as that detailed in section 5.4: various track cuts and width determination schemes were used and the spread of the results calculated following [99].

The following sets of track cuts were used:

1. TPC tracks as defined in section 4.1.1.
2. Moderately tight cuts:
   (a) Combined ITS+TPC tracks.
   (b) At least 70 TPC clusters.
   (c) Same DCA requirements as (1).
3. Tight cuts:
   (a) Combined ITS+TPC tracks.
   (b) At least 70 TPC clusters.
   (c) Maximum DCA to vertex in beam direction $\mathrm{DCA}_z < 2$ cm.

The following mechanisms were used to extract the peak widths:

1. Two nearside Gaussians, one awayside Gaussian plus a constant, as described in section 4.6.1.
2. Widths taken as background-subtracted RMSs of the distributions in the peak regions, with the background determined in the non-peak region under the assumption that between the peaks existed a region of zero jet yield.
3. As method 2, but with different widths for the defined "peak" and "background" regions.

Peak widths $\sigma_{\mathrm{N,A}}$ extracted from minimum bias triggered $\sqrt{s} = 7$ TeV p–p data are shown in figure 7.9; the same procedure was also used for the other datasets and for the quantities calculated from the peak widths, but the plots are not shown here.

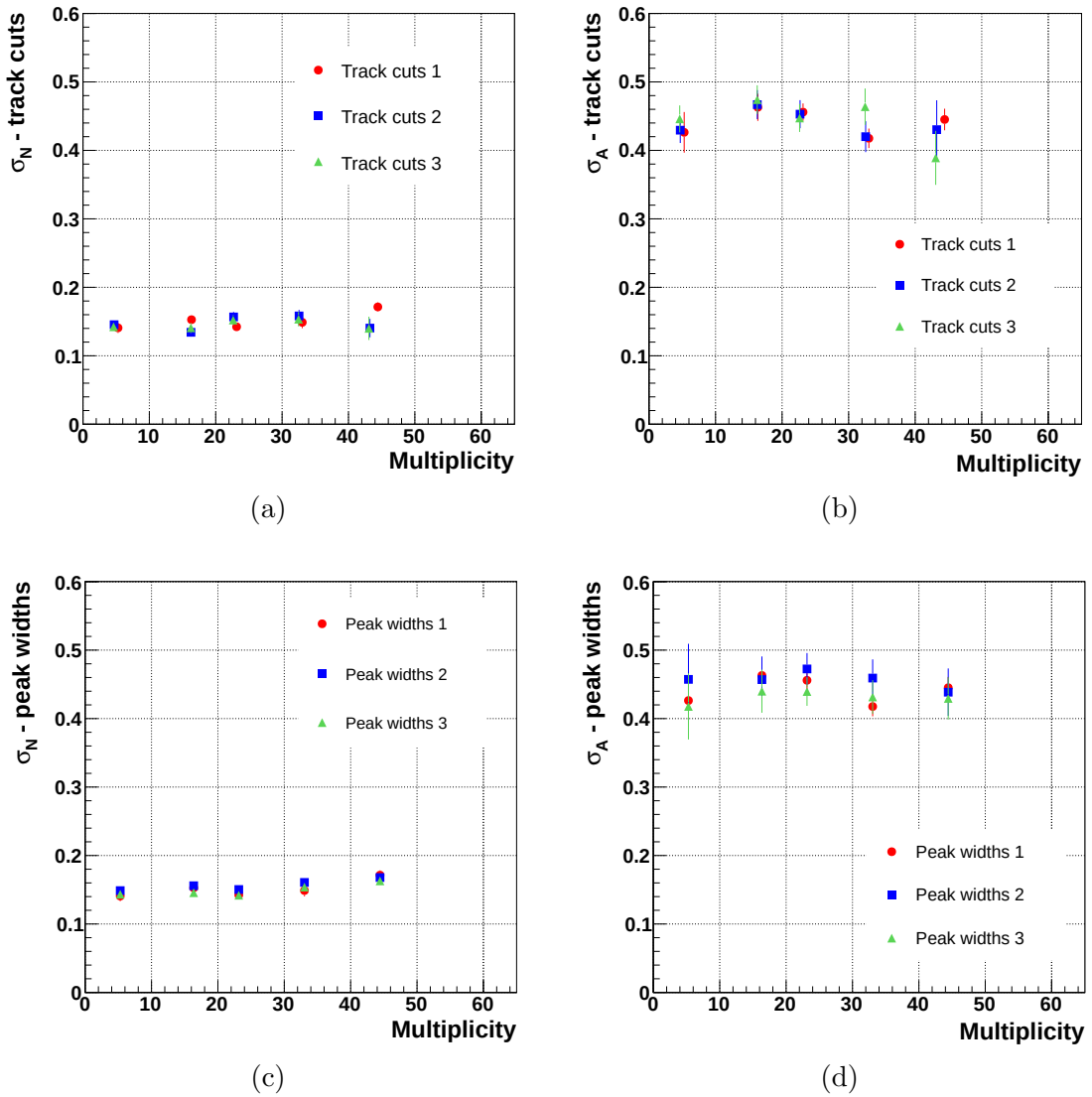

Figure 7.9: Near and awayside peak widths $\sigma_{\mathrm{N,A}}$ extracted from multiplicity-binned, minimum bias triggered $\sqrt{s} = 7$ TeV p–p data using various methods, the spread of which is used to determine the systematic uncertainty.
Top row shows the effects of using different track cuts on the (a) nearside width and (b) awayside width.
Bottom row shows the effects of using width determination schemes on the (c) nearside width and (d) awayside width.
The different methods are described in the text of section 7.4.

CHAPTER 8

CONCLUSIONS AND OUTLOOK

This thesis presents an analysis of the properties of jets in proton–proton and lead–lead collisions at the ALICE experiment at the CERN LHC, using the technique of two-particle azimuthal correlations.

The analysis studied a sample of 45M minimum bias triggered p–p events at $\sqrt{s} =$ 2.76 TeV, 52M minimum bias triggered p–p events at $\sqrt{s} = 7$ TeV and 18M minimum bias triggered Pb–Pb events at $\sqrt{s_{\mathrm{NN}}} = 2.76$ TeV, from data taking periods in 2010 and 2011. During the $\sqrt{s} = 7$ TeV p–p running period, a high multiplicity trigger was also in operation which was utilised to extend the multiplicity reach of the analysis.

Two-particle azimuthal correlations were used to analyse the dependence of jet shape and momentum imbalance on hadron p_{T} in minimum bias p–p collisions. The jet shape, quantified by the jet fragmentation transverse momentum j_{T}, was found to

be independent of hadron p_{T} and to have a value of $\sqrt{\langle j_{\mathrm{T}}^2 \rangle} \approx 0.8$ GeV. This is higher than values measured at other experiments with lower beam energies (for example the values of around 0.6 GeV measured in $\sqrt{s} = 200$ GeV proton collisions at RHIC); this is qualitatively consistent with QCD expectations. The expected difference in $\sqrt{\langle j_{\mathrm{T}}^2 \rangle}$ between the two beam energies studied here is too small to be identified in the measured results. Jet acoplanarity, quantified by the RMS net partonic transverse momentum $\sqrt{\langle k_{\mathrm{T}}^2 \rangle}$, was found to increase with collision energy and also with the transverse momentum of the particles in the jet.

Azimuthal correlations were also used to analyse the dependence of jet yield on multiplicity in p–p collisions and centrality in Pb–Pb collisions. The ratio of awayside to nearside yield was examined, a technique sensitive to jet suppression through interaction with a deconfined medium. In Pb–Pb collisions this suppression was observed as expected, but no suppression was observed in high multiplicity p–p collisions (which were well described by simulated Pythia data).

An analysis of the dependence of jet shape and transverse momentum imbalance on multiplicity/centrality was also performed, with the multiplicity dependence of the jet transverse momentum imbalance quantified with the width of the awayside peak. Although a slight downwards trend was identified in Pb–Pb collisions of increasing centrality, firm conclusions could not be drawn due to the systematic uncertainty.

The jet width was measured to have no dependence on multiplicity with a value of $\sqrt{\langle j_{\mathrm{T}}^2 \rangle} \approx 0.8$ GeV in p–p and peripheral Pb–Pb collisions, consistent with the measurement in minimum bias p–p data. Some indication was observed of a fall in central Pb–Pb collisions which, in the absence of a corresponding narrowing of the nearside peak width, was interpreted as a suppression of the high p_{T} hadrons in the jets.

The study of in-medium parton energy loss manifesting as measurable jet quenching is an area of active theoretical work, with various approaches used to describe the in-

teractions with the medium. Experimental study of different jet-related observables can be used to constrain and discriminate between these models. Two such observables, which are analysed in this thesis, are the jet yields and shapes; both of these are closely related to quantities which can be extracted from models [102, 103, 104].

As an improvement of this analysis for the future, the Monte-Carlo method for extracting $\sqrt{\langle k_{\mathrm{T}}^2 \rangle}$ could be developed further by introducing a jet p_{T} dependent fragmentation function. It would also be informative to analyse jet width and acoplanarity through full event-by-event jet reconstruction.

APPENDIX A

KINEMATICS OF PARTICLE COLLISIONS

Throughout this document, standard high energy physics notation is used. Some commonly used kinematic quantities are defined here.

When describing particle interactions, the Lorentz invariant Mandelstam variable s is defined in terms of a two-particle scattering process $1 + 2 \to 3 + 4$ as

$$s = (p_1 + p_2)^2 = (p_3 + p_4)^2 \tag{A-1}$$

where $p_{1,2,3,4}$ are the four-momenta of the incoming and outgoing particles. While high energy proton collisions are not simple two-particle processes such as this, s is generalised to refer to the momenta of the incoming protons. Thus, $\sqrt{s}$ is equal to the collision energy in the proton–proton centre of mass frame, equivalent to the

laboratory frame in a colliding beam experiment with equal beam energies. When describing heavy ion collisions, the energy is typically quantified by the nucleon–nucleon centre of mass collision energy $\sqrt{s_{\mathrm{NN}}}$.

While the proton–proton centre of mass frame is equivalent to the laboratory frame, the colliding partons can have any fraction x of the total momentum of their parent proton (described by the Parton Distribution Functions (PDFs) as outlined in section 2.1), and so the centre of mass frame of a parton–parton scattering is generally boosted longitudinally to an unknown degree with respect to the laboratory frame. As such, the component of momentum transverse to the beam direction p_{T}, which is invariant under this boost, is often used instead of the overall momentum when describing the particles produced in a collision. In general, a subscript "T" typically refers to the transverse component of a kinematic quantity such as this.

Another widely used kinematic variable is rapidity, defined as

$$y = \frac{1}{2} \ln \frac{E + p_z}{E - p_z} \tag{A-2}$$

where E and p_z are a produced particle's energy and longitudinal momentum respectively. The difference in rapidity between two particles Δy is invariant under a Lorentz boost in the longitudinal direction. As the mass and thus energy of a particle is often not known, this is commonly approximated by the pseudorapidity

$$\eta = -\ln(\tan \frac{\theta}{2}) \tag{A-3}$$

where θ is the polar angle of a particle with respect to the beam direction. Pseudorapidity is equal to rapidity in the limit that particle mass $m \to 0$.

APPENDIX B

MONTE-CARLO SOLVING FOR k_{t}

As explained in section 4.6.3, a Monte-Carlo model was used to extract the final values for net partonic transverse momentum k_{T}, by solving

$$\frac{\langle z_{\mathrm{t}}(k_{\mathrm{T}}, x_{\mathrm{h}})\rangle \sqrt{\langle k_{\mathrm{T}}^2\rangle}}{\langle \hat{x}_{\mathrm{h}}(k_{\mathrm{T}}, x_{\mathrm{h}})\rangle} = \frac{1}{\langle x_{\mathrm{h}}\rangle}\sqrt{\langle p_{\mathrm{out}}^2\rangle - \left\langle j_{\mathrm{Ty}}^2\right\rangle (1 + \langle x_{\mathrm{h}}^2\rangle)} \tag{A-1}$$

(equation 4.15 in the main text). This section describes that model.

The model works by generating a large number of pairs of back-to-back partons, according to a p_{T} spectrum Σ defined as

$$\Sigma = \frac{dN}{d\hat{p}_{\mathrm{T}}} = \frac{1}{\xi + \hat{p}_{\mathrm{T}}^{n-1}} \tag{A-2}$$

where $\xi = 1$ GeV (an unphysical momentum cutoff, required to prevent divergences at low p_{T}, on which the final result does not depend) and n is set such that the

measured hadron p_{T} spectrum is reproduced within the p_{T} range covered by the analysis (assuming here that $\sqrt{\langle k_{\mathrm{T}}^2 \rangle} = \sqrt{\hat{p}_{\mathrm{T}} Q_0}$ where $Q_0 \sim 1$ GeV [98]). This leads to values of $n = 5.0$ for $\sqrt{s} = 2.76$ TeV p–p data, and $n = 4.7$ for $\sqrt{s} = 7$ TeV p–p data.

The partons are then Lorentz boosted in such a manner as to preserve the invariant mass of the pair, resulting in the imbalance quantified by k_{T}. This k_{T} is drawn from a two-dimensional Gaussian with $\sigma = k_{\mathrm{Tinput}}$, such that azimuthal angle is uniformly distributed between 0 and 2π. k_{Tinput} is set to a suitable input value, initially equal to the right-hand-side of equation A-1. A limitation of the model is that it assumes k_{T} to be independent of parton p_{T}, which is believed to not be the case at LHC energies [56].

The partons are then fragmented into a pair of hadrons, according to a fragmentation function $D(z)$ parameterised as

$$D(z) = (1 - z)^{0.88}(1 + z)^{-13.29} z^{-0.16}. \tag{A-3}$$

This parameterisation is obtained from e^+e^- collision data [66, 105]. The fragmentation process also adds a relatively small j_{T} component to the hadrons following the measured value of $\sqrt{\langle j_{\mathrm{T}}^2 \rangle} \sim 0.6$ GeV, as presented in section 5.2.

A large number of hadron pair "dijets" are generated in this manner and the mean z_{t} and $\hat{x}_{\mathrm{h}}$, within p_{Tt} and p_{Ta} bins according the analysis, are output. From these, $\sqrt{\langle k_{\mathrm{T}}^2 \rangle}$ is calculated according to

$$\sqrt{\langle k_{\mathrm{T}}^2 \rangle} = \mathrm{RHS} \cdot \frac{\langle \hat{x}_{\mathrm{h}} \rangle}{\langle z_{\mathrm{t}} \rangle} \tag{A-4}$$

where RHS refers to the right-hand-side of equation A-1. The generation process is then repeated with the calculated k_{T} as the new k_{Tinput}. This iterative process is then repeated until the k_{T} values converge, at which point a consistent value of k_{T}

is deemed to have been calculated.

APPENDIX C

MONTE-CARLO GLAUBER MODEL

As described in section 4.3.2, to determine the centrality percentiles used in the analysis of heavy ion data, the multiplicity spectrum of that data was fit to a Glauber model to describe the collision geometry, with a negative binomial distribution to describe the particle production. This section describes said model, the basic construction of which is well-established in heavy ion physics [82].

In the model, a large number of Pb–Pb collisions are generated, with a multiplicity calculated for each one. The first step is the determination of the position of the nucleons (in spherical polar co-ordinates (r, ϕ, θ)) within each colliding nucleus. The angles ϕ and θ are drawn randomly from flat distributions, and the radius r from a Woods-Saxon distribution.

An impact parameter b is then generated randomly from the distribution $dN/db = b$ (up to a cutoff $b_{\mathrm{max}} \gg R_{\mathrm{Pb}}$, where R_{Pb} is the nucleus radius), and the nuclei

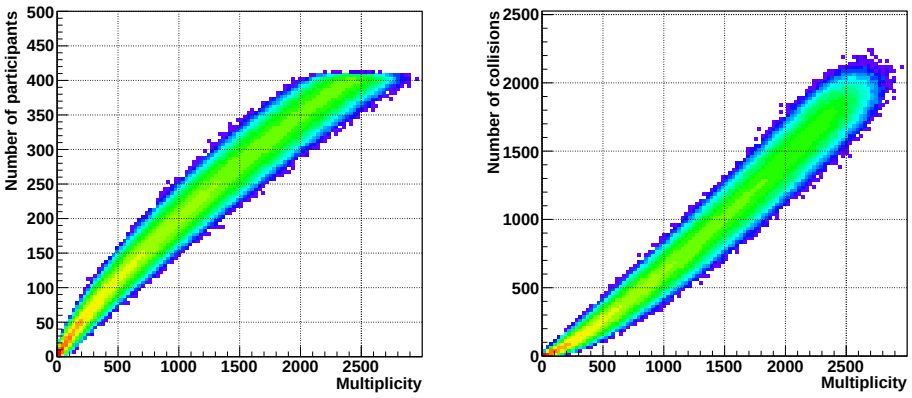

(a) (b)

Figure A-1: Distributions of N_{part} and N_{coll} as functions of observed multiplicity N_{tracks}.

are positioned accordingly. It is assumed that the nucleons have no transverse component of momentum, and that no interactions occur between nucleons of the same nucleus. A collision between two nucleons is deemed to occur when their relative transverse separation $b_{\mathrm{NN}} < \sqrt{\sigma_{\mathrm{NN}}/\pi}$, where σ_{NN} is the inelastic nucleon–nucleon cross section.

For each nucleus–nucleus collison, the number of participants N_{part} and the number of collisions N_{coll} can then be counted. N_{part} is defined as the number of nucleons which undergo at least one collision, and N_{coll} as the total number of binary nucleon–nucleon collisions. The remaining nucleons, which do not collide, are termed spectator nucleons.

The particle production is then assumed to follow a negative binomial distribution, which has been seen to describe the data well at many experiments [106]. N'_{part} is then defined as

$$N'_{\mathrm{part}} = \sum_{1}^{N_{\mathrm{part}}} \mathrm{NB}(\mu, \kappa) \tag{A-1}$$

with N'_{coll} defined similarly, where $\mathrm{NB}(\mu, \kappa)$ are randomly generated numbers sampled from a negative binomial distribution with parameters μ and κ, defined as

$$P^{\mathrm{NB}}_{\mu,\kappa}(n) = \frac{\Gamma(n+\kappa)}{\Gamma(n+1)\Gamma(\kappa)} \cdot \frac{(\mu/\kappa)^n}{(\mu/\kappa+1)^{n+\kappa}}. \tag{A-2}$$

The observed particle multiplicity N_{tracks} is then calculated as

$$N_{\mathrm{tracks}} = pN'_{\mathrm{part}} + (1-p)N'_{\mathrm{coll}} \tag{A-3}$$

where $p \in [0,1]$ defines the relative contribution of N_{part} and N_{coll}. In this manner, the N_{tracks} distribution for a large number of events can be calculated; the dependence of N_{tracks} on N_{part} and N_{coll} is shown in figure A-1. This is then repeated for many p, μ and κ, in order to best fit the resultant distribution to the observed multiplicity distribution. As explained in section 4.3.2, this χ^2 minimisation was performed in the region above 25 tracks, to minimise the contamination from electromagnetic interactions.

REFERENCES

[1] R. Feynman, *QED: The Strange Theory of Light and Matter* (Princeton University Press, 1985).

[2] D. Perkins, *Introduction to High-Energy Physics 3rd Ed.* (Addison-Wesley, London, 1987).

[3] E. D. Bloom *et al.*, Phys.Rev.Lett. **23**, 930 (1969).

[4] J. Bjorken and E. A. Paschos, Phys.Rev. **185**, 1975 (1969).

[5] M. Gell-Mann, Phys.Lett. **8**, 214 (1964).

[6] G. Zweig, (1964), PRINT-64-170.

[7] V. Barnes *et al.*, Phys.Rev.Lett. **12**, 204 (1964).

[8] Particle Data Group, K. Nakamura, J. Phys. **G37**, 075021 (2010).

[9] R. K. Ellis, W. J. Stirling, and B. Webber, Camb. Monogr. Part. Phys. Nucl. Phys. Cosmol. **8**, 1 (1996).

[10] K. Yagi, T. Hatsuda, and Y. Miake, Camb. Monogr. Part. Phys. Nucl. Phys. Cosmol. **23**, 1 (2005).

[11] D. Gross and F. Wilczek, Phys.Rev.Lett. **30**, 1343 (1973).

[12] H. D. Politzer, Phys.Rev.Lett. **30**, 1346 (1973).

[13] N. Cabibbo and G. Parisi, Phys.Lett. **B59**, 67 (1975).

[14] E. Witten, Phys. Rev. **D30**, 272 (1984).

[15] R. Vogt, *Ultrarelativistic heavy-ion collisions* (Elsevier, 2007).

[16] F. Karsch, Lect.Notes Phys. **583**, 209 (2002), hep-lat/0106019.

[17] J. D. Bjorken, Phys. Rev. D **27**, 140 (1983).

[18] STAR Collaboration, B. Abelev *et al.*, Phys.Rev. **C79**, 034909 (2009), 0808.2041.

[19] ALICE Collaboration, P. Petrov, Acta Phys.Polon.Supp. **5**, 263 (2012).

[20] S. Hands, Contemp. Phys. **42**, 209 (2001), physics/0105022.

[21] Simulation of heavy ion collision, Retrieved from internet January 2013 `http://ipap.yonsei.ac.kr/~npl/intro0.html`.

[22] H. Caines, J.Phys. **G31**, S101 (2005), nucl-ex/0412016.

[23] ALICE Collaboration, K. Aamodt *et al.*, Phys.Lett. **B696**, 328 (2011), 1012.4035.

[24] F.-M. Liu and K. Werner, J.Phys. **G38**, 124183 (2011), 1106.5909.

[25] V. Topor Pop, M. Gyulassy, J. Barrette, C. Gale, and A. Warburton, Phys.Rev. **C86**, 044902 (2012), 1203.6679.

[26] C. Lindsey *et al.*, Nucl.Phys. **A498**, 181C (1989).

[27] ALICE Collaboration, K. Aamodt *et al.*, Eur.Phys.J. **C68**, 345 (2010), 1004.3514.

[28] PHOBOS Collaboration, B. Alver *et al.*, Phys.Rev. **C83**, 024913 (2011), 1011.1940.

[29] CMS Collaboration, D. Velicanu, J.Phys. **G38**, 124051 (2011), 1107.2196.

[30] STAR Collaboration, J. Adams *et al.*, Phys.Rev.Lett. **95**, 152301 (2005), nucl-ex/0501016.

[31] K. Werner, I. Karpenko, and T. Pierog, Phys.Rev.Lett. **106**, 122004 (2011), 1011.0375.

[32] R. C. Hwa and C. Yang, Phys.Rev. **C83**, 024911 (2011), 1011.0965.

[33] WA97 Collaboration, E. Andersen *et al.*, J.Phys. **G25**, 181 (1999).

[34] STAR, J. Adams *et al.*, Nucl. Phys. **A757**, 102 (2005), nucl-ex/0501009.

[35] J. Rafelski and B. Muller, Phys. Rev. Lett. **48**, 1066 (1982).

[36] T. Matsui and H. Satz, Phys.Lett. **B178**, 416 (1986).

[37] NA50 Collaboration, B. Alessandro *et al.*, Eur.Phys.J. **C39**, 335 (2005), hep-ex/0412036.

[38] PHENIX Collaboration, A. Adare *et al.*, Phys.Rev.Lett. **98**, 232301 (2007), nucl-ex/0611020.

[39] PHENIX Collaboration, S. S. Adler *et al.*, Phys.Rev.Lett. **96**, 012304 (2006), nucl-ex/0507032.

[40] ALICE Collaboration, B. Abelev *et al.*, Phys.Rev.Lett. **109**, 072301 (2012), 1202.1383.

[41] R. L. Thews, M. Schroedter, and J. Rafelski, Phys.Rev. **C63**, 054905 (2001), hep-ph/0007323.

[42] A. Andronic, P. Braun-Munzinger, K. Redlich, and J. Stachel, Phys.Lett. **B652**, 259 (2007), nucl-th/0701079.

[43] R. Snellings, New J.Phys. **13**, 055008 (2011), 1102.3010.

[44] A. Perry, schematic image of two colliding ions, private communication.

[45] ALICE Collaboration, M. Krzewicki, J.Phys. **G38**, 124047 (2011), 1107.0080.

[46] STAR, J. Adams *et al.*, Phys. Rev. **C72**, 014904 (2005), nucl-ex/0409033.

[47] ALICE Collaboration, K. Aamodt *et al.*, Phys.Rev.Lett. **105**, 252302 (2010), 1011.3914.

[48] CMS Collaboration, S. Chatrchyan *et al.*, Phys.Rev. **C87**, 014902 (2013), 1204.1409.

[49] ALICE Collaboration, K. Aamodt *et al.*, Phys.Lett. **B696**, 30 (2011), 1012.1004.

[50] STAR Collaboration, J. Adams *et al.*, Phys.Rev.Lett. **91**, 172302 (2003), nucl-ex/0305015.

[51] PHENIX Collaboration, S. Adler *et al.*, Phys.Rev. **C69**, 034910 (2004), nucl-ex/0308006.

[52] STAR, J. Adams *et al.*, Phys. Rev. Lett. **91**, 072304 (2003), nucl-ex/0306024.

[53] H. Zhang, J. Owens, E. Wang, and X.-N. Wang, Phys.Rev.Lett. **98**, 212301 (2007), nucl-th/0701045.

[54] PHENIX Collaboration, J. Jia, Nucl.Phys. **A855**, 92 (2011), 1012.0858.

[55] ALICE Collaboration, K. Aamodt *et al.*, Phys.Rev.Lett. **108**, 092301 (2012), 1110.0121.

[56] D. A. Appel, Phys.Rev. **D33**, 717 (1986).

[57] J. Blaizot and L. D. McLerran, Phys.Rev. **D34**, 2739 (1986).

[58] M. Rammerstorfer and U. W. Heinz, Phys.Rev. **D41**, 306 (1990).

[59] N. Armesto *et al.*, Phys.Rev. **C86**, 064904 (2012), 1106.1106.

[60] V. A. Khoze and W. Ochs, Int.J.Mod.Phys. **A12**, 2949 (1997), hep-ph/9701421.

[61] V. A. Khoze, W. Ochs, and J. Wosiek, (2000), hep-ph/0009298.

[62] H1 and ZEUS, F. D. Aaron *et al.*, JHEP **01**, 109 (2010), 0911.0884.

[63] B. A. Kniehl, G. Kramer, and B. Potter, Nucl.Phys. **B597**, 337 (2001), hep-ph/0011155.

[64] R. P. Feynman, R. D. Field, and G. C. Fox, Nucl. Phys. **B128**, 1 (1977).

[65] CERN-College de France-Heidelberg-Karlsruhe, M. Della Negra *et al.*, Nucl. Phys. **B127**, 1 (1977).

[66] PHENIX, S. S. Adler *et al.*, Phys. Rev. **D74**, 072002 (2006), hep-ex/0605039.

[67] CERN-Columbia-Oxford-Rockefeller, A. L. S. Angelis *et al.*, Phys. Lett. **B97**, 163 (1980).

[68] A. Kulesza, G. Sterman, and W. Vogelsang, Nucl. Phys. **A721**, 591 (2003), hep-ph/0302121.

[69] L. Apanasevich *et al.*, Phys. Rev. **D59**, 074007 (1999), hep-ph/9808467.

[70] J. D. Bjorken, FERMILAB-PUB-82-059-THY.

[71] M. Gyulassy, I. Vitev, X.-N. Wang, and B.-W. Zhang, (2003), nucl-th/0302077.

[72] R. Baier, Y. L. Dokshitzer, A. H. Mueller, S. Peigne, and D. Schiff, Nucl.Phys. **B483**, 291 (1997), hep-ph/9607355.

[73] M. Gyulassy, P. Levai, and I. Vitev, Nucl.Phys. **A661**, 637 (1999), hep-ph/9907343.

[74] X.-N. Wang and X.-f. Guo, Nucl.Phys. **A696**, 788 (2001), hep-ph/0102230.

[75] P. B. Arnold, G. D. Moore, and L. G. Yaffe, JHEP **0112**, 009 (2001), hep-ph/0111107.

[76] ALICE Collaboration, R. Lietava, J.Phys.Conf.Ser. **381**, 012040 (2012).

[77] T. Renk, H. Holopainen, R. Paatelainen, and K. J. Eskola, Phys.Rev. **C84**, 014906 (2011), 1103.5308.

[78] L. Evans and P. Bryant, JINST **3**, S08001 (2008).

[79] C. Salgado *et al.*, J.Phys. **G39**, 015010 (2012), 1105.3919.

[80] M. Benedikt *et al.*, (2000), CERN-2000-003.

[81] ATLAS Collaboration, G. Aad *et al.*, Nature Commun. **2**, 463 (2011), 1104.0326.

[82] ALICE Collaboration, B. Abelev *et al.*, Phys.Rev.Lett. **105**, 252301 (2010), 1011.3916.

[83] ALICE, K. Aamodt *et al.*, JINST **0803**, S08002 (2008).

[84] ALICE Collaboration, K. Aamodt *et al.*, Phys.Rev.Lett. **106**, 032301 (2011), 1012.1657.

[85] ALICE, G. Dellacasa *et al.*, CERN-LHCC-99-12.

[86] A. Morsch and B. Pastircak, Radiation in ALICE detectors and electronics racks, ALICE Internal Note ALICE-INT-2002-028.

[87] ALICE TPC Layout, ALICE TPC page, retrieved March 2009 `http://aliceinfo.cern.ch/TPC/`.

[88] ALICE, G. Dellacasa *et al.*, CERN-LHCC-2000-001.

[89] P. Newman, Tracking detectors II, Lecture delivered Birmingham 2008, `http://epweb2.ph.bham.ac.uk/user/newman/appt08/lecture8.pdf`.

[90] M. Krivda *et al.*, JINST **7**, C01057 (2012).

[91] A. Jusko, M. Krivda, and R. Lietava, CTP training, Course delivered CERN 2012, `http://juskoa.web.cern.ch/juskoa/train_last/ctptrain.pdf`.

[92] D. Elia, G. Aglieri Rinella, A. Kluge, M. Krivda, and M. Nicassio, Int. J. Mod. Phys. **E16**, 2503 (2007), nucl-ex/0703019.

[93] ALICE, e. . Alessandro, B. *et al.*, J. Phys. **G32**, 1295 (2006).

[94] M. J. Tannenbaum, PoS **CFRNC2006**, 001 (2006), nucl-ex/0611008.

[95] T. Sjostrand, S. Mrenna, and P. Z. Skands, JHEP **0605**, 026 (2006), hep-ph/0603175.

[96] P. Z. Skands, Phys.Rev. **D82**, 074018 (2010), 1005.3457.

[97] X.-N. Wang and M. Gyulassy, Phys.Rev. **D44**, 3501 (1991).

[98] V. A. Khoze and M. Ryskin, private communication.

[99] L. Lyons, J. Phys. A: Math. Gen. **25**, 1967 (1992).

[100] ATLAS, G. Aad *et al.*, Eur.Phys.J. **C73**, 2509 (2013), 1304.4739.

[101] CMS Collaboration, S. Chatrchyan *et al.*, Phys.Rev. **C84**, 024906 (2011), 1102.1957.

[102] T. Renk and K. J. Eskola, Phys.Rev. **C84**, 054913 (2011), 1106.1740.

[103] N. Armesto, C. A. Salgado, and U. A. Wiedemann, Phys.Rev.Lett. **93**, 242301 (2004), hep-ph/0405301.

[104] M. Y. Kopysov and Y. E. Pokrovsky, Phys.Lett.B (1997), hep-ph/9705326.

[105] DELPHI Collaboration, P. Abreu *et al.*, Eur.Phys.J. **C13**, 573 (2000).

[106] M. L. Miller, K. Reygers, S. J. Sanders, and P. Steinberg, Ann. Rev. Nucl. Part. Sci. **57**, 205 (2007), nucl-ex/0701025.